UNIVERSITY OF FORT HARE

Faculty of Science & Agriculture

Chemistry Department

Preparation of photocatalytic TiO_2 nanoparticles immobilized on carbon nanofibres for water purification

Pardon Nyamukamba
(Student Number: 200805439)

Dr L.Tichagwa (Supervisor)

Dr C. Greyling (Co-Supervisor)

A DISSERTATION SUBMITTED TO THE UNIVERSITY OF FORT HARE IN FULFILLMENT OF THE REQUIREMENT FOR THE DEGREE OF MASTER OF SCIENCE IN CHEMISTRY

MARCH 2011

Declaration

I, Pardon Nyamukamba, declare that this work was done in the Department of Chemistry, University of Fort Hare, Private Bag X1314, Alice, 5700 from February 2009 to November 2010 and has not been submitted in part or in whole to any other university.

Dedications

This work is dedicated to my wife Nyarai Meg, my daughter Natalie Anopaishe, my mother Beatrice and my father Liverty in appreciation of their inspiration, unconditional love and acceptance.

Acknowledgements

God the Almighty made everything possible and I am so thankful.

I would like to express my sincere gratitude to my supervisors Dr Lilian Tichagwa and Dr Corinne Greyling for their guidance and fruitful conversations. My achievements during my MSc research would not have been possible without their excellent guidance and support. I also thank my fellow Chemistry postgraduate students for their support. I could have not done it without them.

To my uncles Gonyeti and Joel, my brothers, sisters and all my relatives and friends who were always there for me, I say thank you so much for the support and bringing the best out of me and may God richly bless you.

Additionally I would like to acknowledge and thank the following people for their assistance in various ways Mr H. Mungondori, Mr N.C. Manene, Mr T. Bunhu, Mr E. Rudolph, Mr R. Taziwa, Nikita, S. Musyoka, Dr R. Butcher, Mr B. Ulrich, Mr M. Nwamadi, Mr Thandisile and all departmental staff who were genuinely interested in my work and extremely supportive. It is with a deep sense of gratitude that I thank the National Research Foundation and the Department of Science and Technology of South Africa for their generous financial support as part of the Nanotechnology for Water Treatment Flagship with Professor Sanderson as the grant holder as well as the Govan Mbeki Research and Development Centre at the University of Fort Hare.

Abstract

Titanium dioxide nanoparticles were prepared using the sol-gel process. The effect of temperature and precursor concentration on particle size was investigated. The optimum conditions were then used to prepare carbon and nitrogen doped titanium dioxide (TiO_2) nanoparticles. Doping was done to reduce band gap of the nanoparticles in order to utilize visible light in the photocatalytic degradation of organic compounds. A significant shift of the absorption edge to a longer wavelength (lower energy) from 420 nm to 456 nm and 420 nm to 428 nm was observed for the carbon doped and nitrogen doped TiO_2 respectively. In this study, the prepared TiO_2 photocatalyst was immobilized on carbon nanofibres to allow isolation and reuse of catalyst. The photocatalytic activity of the catalyst was tested using methyl orange as a model pollutant and was based on the decolourization of the dye as it was degraded. The doped TiO_2 exhibited higher photocatalytic activity than the undoped TiO_2. The materials prepared were characterized by XRD, TEM, SEM, FT-IR, DSC and TGA while the doped TiO_2 was characterized by XPS, ESR and Raman Spectroscopy.

LIST OF FIGURES

LIST OF TABLES

List of Abbreviations

PAN: Polyacrylonitrile

DMF: Dimethyl formamide

DSC: Differential scanning calorimetry

FTIR: Fourier-transform infrared spectroscopy

TGA: Thermogravimetric analysis

XRD: X-ray diffraction

TEM: Transmission electron microscopy

SEM: Scanning electron microscopy

UV-Vis: Ultraviolet visible spectroscopy

XPS: X-ray photoelectron spectroscopy

GC: Gas chromatography

DRS: Diffuse reflectance spectroscopy

EDX: Energy dispersive X-ray spectroscopy

ESR: Electron-spin resonance spectroscopy

TABLE OF CONTENTS

CHAPTER 1

1. General introduction

1.1 Study introduction and motivation

Water treatment and provision of safe potable water are tasks that most developing countries struggle to undertake. Millions of people worldwide especially in such countries have no access to safe drinking water. The world is having a challenge of meeting ever increasing demands for safe drinking water as the available supplies of fresh water are decreasing due to natural disasters such as droughts, health-based requirements and rapid growth of world population (Savage & Diallo, 2005). A lot of people are dying due to water related diseases and this means that safe drinking water is of great importance in both developed and developing countries thus showing a clear need for the improvement and development of new techniques for water treatment.

People are concerned about the contaminants in their water supply that may affect health or make water produce a foul taste. The available water in lakes, dams, rivers and underground water is not safe for drinking because it contains more than seven hundred soluble organic compounds, pathogens (Gupta & Ali, 2006), fine colloidal materials and toxic heavy metals derived from municipal, leaking underground storage tanks, industrial and agricultural activities as well as from the natural decomposition of animal and vegetable matter.

Organic compounds such as phenols cause unpleasant taste and odour in drinking water and can exert negative effects on normal biological processes (Dabrowski et al, 2005). Contaminants such as benzene, chlorobenzene, trichloroethylene, carbon tetrachloride, methylene chloride and vinyl chloride may pose health risks if they are present in large quantities. These organic contaminants need to be removed from water if the water is to be used in homes for human consumption. Several methods are available for treating water and these include chlorination, adsorption, flocculation and coagulation, ultra-filtration and reverse osmosis among others.

Some of the methods for water treatment have some significant disadvantages. For instance, when water is treated with chlorine or chloroamines, the chlorine may react with organic matter and produce compounds such as trihalomethanes (THM) as by-products which increase the risk of certain cancers (Dvorak & Skipton, 2008). Also, when adsorption is used to remove organic and inorganic micro-pollutants from water, it involves the accumulation of substance on the surface or interface which is basically a phase transfer of pollutants without degradation. The main drawback of this method is the production of secondary pollutants (sludge) that need disposal. This can be an expensive process in cases where activated carbon is used for adsorption and is to be regenerated. Such disadvantages of these commonly used methods have prompted research interest into the production of low-cost alternatives to adsorbents such as activated carbon and development of new water treatment methods such as photocatalysis.

Nanotechnology has been found to play an important role in solving many of the problems that are encountered in water purification (Savage & Diallo, 2005). The recent

development of nanotechnology has proved that nanomaterials such as nano-sized metal oxide catalysts can have high activity in the photo-degradation of a wide range of organic and inorganic contaminants in water (Theron et al, 2008). It is believed that photocatalysis will soon be recognized as one of the most effective means of dealing with various kinds of wastewater since organic pollutants can be completely degraded to harmless matter under normal conditions of temperature and pressure (Shifu & Gengyu, 2005). Unfortunately, the use of nanometric photocatalysts has also presented problems such as separation of catalyst particles from suspension after photocatalysis and the possibility of aggregation of the suspended particles. This problem is overcome by immobilizing the photocatalyst on supports such as polymer nanofibres using methods such as electrospinning. The use of carbon nanofibres as TiO_2 support means that the contaminants are first adsorbed and brought in the vicinity of the photocatalyst where they are degraded. This makes the immobilization method very effective in the degradation of contaminants that do not easily adsorb on the photocatalyst (Torimoto et al, 1996).

Although it has been shown that titanium dioxide nanoparticles perform under direct sunlight, only 5 % of the total natural light has enough energy to cause effective photosensitization (Wilke & Breuer, 1999). The abundance of the visible light (55% compared to 5% for UV) motivated a great deal of research to enhance the effectiveness of TiO_2 and to increase the spectral response in the visible region. This is achieved by modification of the TiO_2 photocatalyst through doping.

No single method manages to remove all contaminants and often a combination of treatment processes is required to effectively treat the water. Photocatalysis presents itself as a promising technique. Regardless of which method of treatment is considered, the water should be tested first to determine what substances are present. It is important to know what contaminants are present and their quantities prior to selecting the method of treatment as this helps to choose the best and effective method.

1.2 Problem statement

The photocatalytic activity of titanium dioxide (TiO_2) for the photomineralisation of organic compounds was found to be higher when the particle size of the catalyst was in the nano-range (Anpo et al, 1987: Maira et al, 2000). Most precursors to the titanium dioxide are very reactive and it is very difficult to control the hydrolysis rate and subsequently the particle size. The particle size of TiO_2 photocatalyst can be reduced by controlling the hydrolysis rate and by using the appropriate values of parameters such as precursor concentration and reaction temperature. Thus it is necessary to come up with the best synthesis conditions if the smallest possible nanoparticles are to be produced. TiO_2 has a wide band gap and reducing the particle size increases the band gap hence it can only absorb ultraviolet light which is only 5 % of the solar radiation reaching the earth's surface. This means that more energy is needed to supply light of appropriate wavelength and this makes the use of TiO_2 expensive. Hence there is need to modify the band gap of TiO_2. This can be done by incorporation of non metals so that it uses light in the visible region which accounts for 55 % light. Once TiO_2 is prepared, its use in the form of powder in water treatment has a big disadvantage since there is need for separation of the catalyst from the treated water after the photodegradation process. There

is therefore a clear need to immobilize the catalyst on solid nano-supports which would be relatively simpler to remove from water.

1.3 Aims and objectives

The main objective of this study is to prepare TiO_2 nanoparticles using the sol-gel process and immobilize them on carbon nanofibres for the removal of organic contaminants in water.

1.3.1 Specific objectives

1. To prepare TiO_2 nanoparticles and study the effect of the sol-gel temperature and precursor concentration on the particle size of the nanoparticles produced.
2. To deduce the optimum conditions of temperature and precursor concentration in the preparation of TiO_2 nanoparticles.
3. To increase the spectral response of TiO_2 nanoparticles prepared using the optimum conditions through doping with carbon and nitrogen.
4. To immobilize TiO_2 nanoparticles on carbon nanofibers via electrospinning and carbonization.
5. Evaluate the photocatalytic activity of the prepared TiO_2/PAN composite nanofibres.

1.4 Delineation and delimitations of the study

The average particle size of the TiO_2 nanoparticles increases when the calcination temperature is very high resulting in reduction of surface area (Youping et al, 2007: Miki et al, 2009). Also conversion of anatase phase (more photo-catalytically active) to rutile

was found to occur at temperatures above 600 °C (Sotter et al, 2005 : Miki et al, 2009) so to ensure that part of the TiO_2 is in anatase phase a maximum annealing temperature of 600 °C is used.

1.5 Dissertation outline

The dissertation consists of seven (7) chapters and is organized such that each chapter has its own introduction and list of references. The study is first introduced in Chapter 1 and the problem statement, aims and objectives are stated in this chapter. Chapter 2 is the literature review that gives an overview of TiO_2 photocatalysts, their properties, basic principles of photocatalysis, ways modifying the nanomaterials, applications, preparation methods and process parameters affecting their properties in synthesis. This chapter also explains processes involved in preparation of carbon nanofibres, immobilization of the TiO_2 nanoparticles on the carbon nanofibres and the characterization techniques.

Chapter 3 gives the preliminary studies of the study where the purity and authenticity of the PAN powder are determined. Also the suitable stabilization and carbonization conditions for the electrospun nanofibres using the available equipment are established. Chapter 4 describes the methods used for the synthesis of TiO_2 nanoparticles and their immobilization on electrospun nanofibres while Chapter 5 gives the characterization of the photocatalyst/carbon composite nanofibres.

Chapter 6 describes the method used for carbon and nitrogen doping, characterization of the doped TiO_2 and evaluation of photocatalyst activity and finally Chapter 7 gives a summary of concluding remarks along with recommendations for future work.

References

Anpo, M., Shima, T.; Kodama, S.; Kubokawa, Y. *Journal of Physical Chemistry* ***1987***, *91*, 4305-4310.

Dabrowski, A.; Podkoscielny, P.; Hubicki, Z.; Barczak, M. *Chemosphere* **2004**, *58*, 1049-1070.

Dvorak, B. I & Skipton, S. O. *Drinking Water Treatment: Activated Carbon Filtration G1489* **2008**.

Gupta, V. K & Ali, I. *Encyclopedia of Surface and Colloid Science: Second Edition **2006***.

Maira, A. J.; Yeung, K. L.; Lee, C. Y.; Yeu, P. L.; Chan, C. K. L. *Journal of Catalysis* **2000**, *192*, 185-196.

Miki, T.; Nishizawa, K.; Watanabe, E.; Taoda, H. *Research on Chemical Intermediates* **2009**, *35* : 257-262.

Savage, N, & Diallo, M. S. *Journal of Nanoparticle Research* **2005**, *7*, 331–342.

Shifu, C & Gengyu, C. *Chemosphere* **2005**, *60*, 1308-1315

Sotter, E.; Vilanova, X.; Llobet, E.; Stankova, M.; Correig, X. *Journal of Optoelectronics and Advanced Materials* **2005**, *7*, 1395-1398.

Theron, J.; Walker, J. A.; Cloete, T. E. *Critical Reviews in Microbiology* **2008**, *34*:43–69.

Torimoto, T.; Ito, S.; Kuwabata, S.; Yoneyama, H. *Enviromental Science Technology* **1996**, *30*, 1275-1281.

Youping, C.; Hongaqi, S.; Wanqin, J.; Nanping, X, (2007). *Chinese Journal of Chemistry* **2007**, *15*, 178-183.

CHAPTER 2

2. Literature review

2.1 Introduction

Since 1972 when Fujishima and Honda discovered the photocatalytic splitting of water using titanium electrodes, interest in using TiO_2 as a homogenous catalyst for waste water and ground water remediation has increased tremendously (Kositzi et al. 2004; Prieto et al. 2005). This is because the catalyst is capable of degrading several organic and inorganic pollutants (Kabra et al, 2004). Titanium dioxide can adopt seven structures namely columbite, bronze, anatase, rutile, brookite, ramsdellite and hollandite (Rocquefelte et al, 2004) but exists as three allotropic forms (anatase, brookite and rutile) in nature. Among these the most common is rutile. The crystal systems of rutile and anatase are tetragonal while brookite is orthorhombic. Some illustrations of the crystal structure of TiO_2 are given in Figure 2.1. In anatase the octahedrals are connected by their vertices while in rutile they are connected by their edges. The crystal structure of TiO_2 largely depends on the preparation method.

Upon heating, both anatase and brookite convert to rutile which is more stable at all temperatures and pressures below 60 kbar according to thermodynamic calculations (Banfield, 2001). Reverse phase stability is described by particle size experiments due to size effect on surface energy. When the TiO_2 particles are less than 50 nm, anatase is more stable and can only transform to rutile at temperatures above 700 °C (Xiaobo, 2009). Zhang reported that anatase is the most stable at sizes less than 11 nm, brookite at sizes between 11-35 nm and rutile at sizes greater than 35 nm (Zhang, 2000).

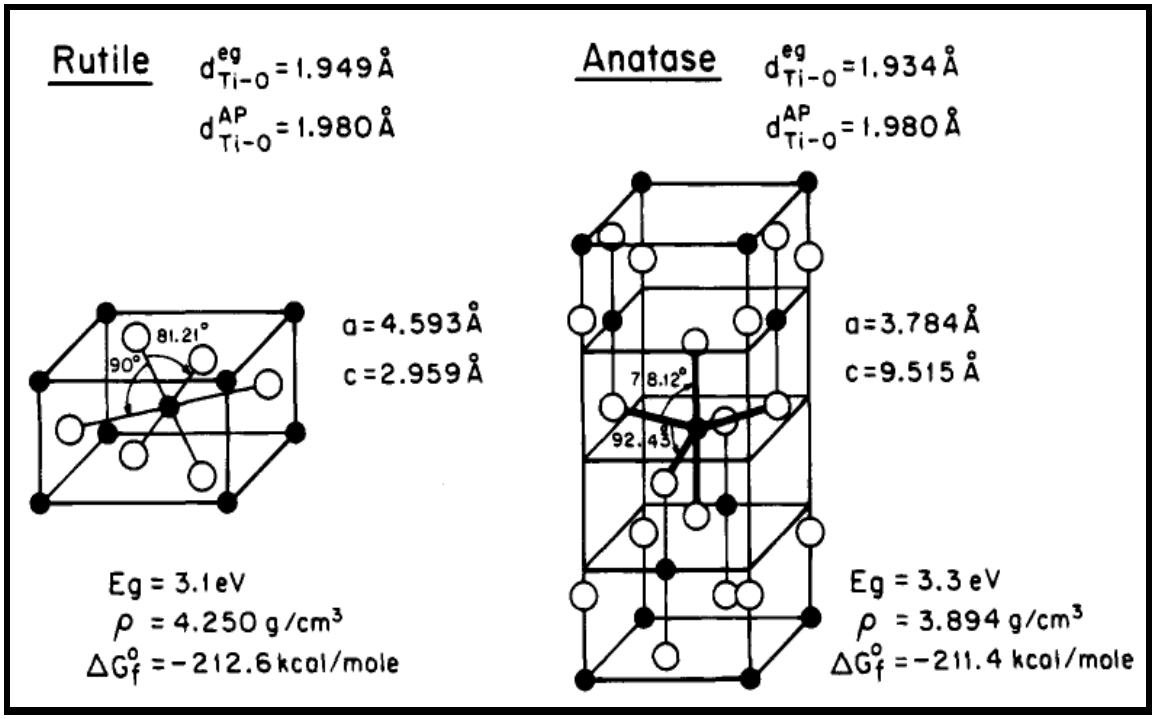

Figure 2.1: Structure of rutile and anatase (Linsebigler et al, 1995).

Although anatase is thermodynamically less stable than rutile, its formation is kinetically favoured at relatively lower temperatures ($<600^{0}$C). The lower temperature could explain the higher surface area and higher surface density of active sites for adsorption and for catalysis since higher temperatures increase particle size (Hermann, 1999: Chen et al, 2003). It has been reported that photocatalytic activity is high when it is in the anatase form even though the sample morphology is an important property in determining photocatalytic activity (Falcomer et al, 2006). A lot of studies reported that the photocatalytic activity of nano-sized TiO_2 is affected by particle size, specific area, crystalline phase and surface properties (e.g. surface OH and oxygen vacancy) (Linsebigler et al, 1995). It is known that surface defects play an important role in the photocatalytic activity, since defects act as active sites for the adsorption and dissociation

of molecules on the surface (Sakai et al, 2001). The photocatalytic activity of TiO_2 can also be enhanced by incorporation of impurities in the lattice structure.

2.2 Nanopowder properties

Nanopowders are three dimensional uni-axial nanosized objects at a level intermediate between atom/molecule and bulk. Semiconductor photocatalysts studied have been either metal oxides such as (ZnO, WO_3, CeO_2, ZrO_2, Nb_2O_3, Fe_2O_3, SnO_2,) or chalcogenides such as (CdS, ZnS, CdTe, ZnSe, CdSe) (Peral et al, 1997). These nanopowders have a tendency to grow into micro-powders or macroscopic materials instantaneously and then lose their specific features. Therefore, the production of a nanopowder with controlled particle size and degree of aggregation is the main attraction for the many research efforts. Recently, significant progress in the diversity of preparative methods has been made. Powder size is the primary driver for the growing synthetic interest as it affects photocatalyst properties. For instance, the optical absorption spectrum of gold changes as the gold particle size changes. In general, nanoparticles have different classical properties from the bulk material.

2.2.1 High surface-to-volume (S/V) ratio

The size and surface characteristics of nanoparticles are related. For a spherical particle, the surface to volume ratio is inversely proportional to its radius. As the size of the nanoparticle decreases to the nanometer range, its surface area will increase significantly and a large fraction of these atoms will be exposed on the surface. In addition, they become more active since the surface atoms which are more chemically active than the bulk atoms have fewer adjacent coordinate atoms. As a result, surface characteristics play

an important role in the properties of nanoparticles from phase transformation to reactivity.

2.2.2 Discrete electronic structure

The energy levels of nanoparticles are not continuous as in bulk materials; instead they are discrete due to the confinement of the electron wave function. This results in the electronic, optical and magnetic properties being size dependent. Rademann reported that mercury behaves as either a metal or nonmetal depending on its particle size (Rademann et al, 1992). Optical absorption spectroscopy is used to investigate the size dependent properties as the position and shape of the absorption peaks depend strongly on particle size. Figure 2.2 shows the absorption spectra of CdSe nanoparticles of different sizes

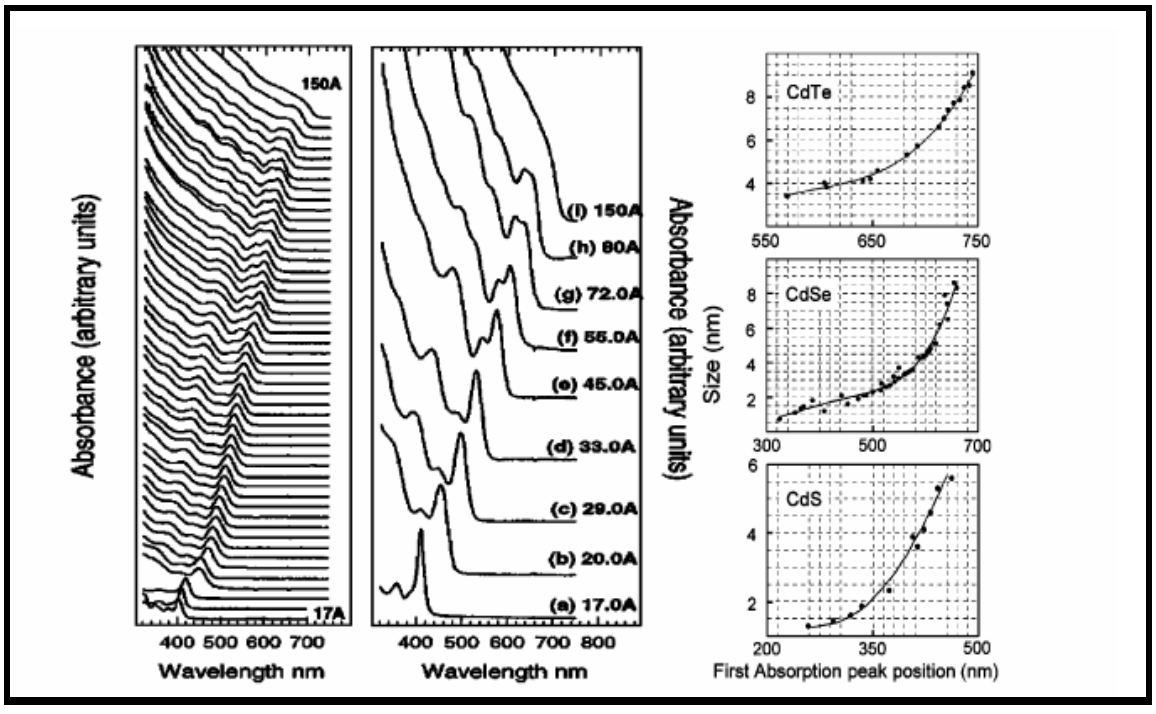

Figure 2.2: Discrete electronic transitions in optical absorption for different sizes of CdSe nanoparticles (left, middle) and the first absorption peak change versus nanoparticle size (right) (Yu, 2003).

As the size of the nanoparticles increases, the λ_{max} shifts to higher wavelengths (left and middle diagrams). The far right diagram shows how the first absorption peak changes as the nanoparticle size changes for CdSe, CdS, CdTe (Qu, 2001; Yu, 2003).

2.2.3 High reactivity

Nanoparticles are expected to be more reactive because of high surface area and a large fraction of surface atoms. The ability of nanoparticles of some elements to act as catalysts has been investigated. It has been found that the reaction of elemental oxygen with silver depends on particle size (Rao et al, 2004). The smaller silver nanoparticles are capable of dissociating oxygen molecules to atomic oxygen. Such an observation was also found to be similar to the chemisorption study of chlorine on copper (Baetzold, 1981) and carbon monoxide on palladium (Grunze, 1978). Although gold is very stable and inert, when its nanoparticles were supported on a TiO_2 surface they had a marked size effect on their catalytic activity in the oxidation of carbon monoxide, showing maximum chemical activity when the nanoparticles were 3.5nm and below (Valden et al, 1998).

2.3 Selection of a suitable semi-conductor for photocatalysis

There are several semiconductors that may be used for photocatalysis, such as TiO_2, ZnO, MgO, WO_3, Fe_2O_3, CdS. An ideal photocatalyst for photocatalytic oxidation should have the following properties:

(i) Photo-stability

(ii) Availability

(iii) Low cost

(iv) Chemically and biologically inert

(v) Ability to adsorb reactants

Of all the available semi-conductors which can be used as photocatalysts, TiO_2 is generally considered to be the best semiconductor photocatalyst available at present (Mills et al, 2002). It is particularly attractive for the degradation of organic pollutants due to its ability to use solar radiation as a source of light and to operate without pH adjustments unlike the photo-Fenton process which requires a specific pH range (Perez-Estrada et al, 2005). The other advantages of using titanium dioxide include:

i. its ability to mineralize pollutants such as herbicides, carboxylic acids, and alcohols completely to carbon dioxide, water and simple minerals (Calza et al, 2006).
ii. non-toxicity
iii. photochemical stability
iv. strong oxidizing power at ambient temperature and pressure
v. photo-generated electrons are reducing enough to produce superoxide from oxygen
vi. Anti-bacterial
vii. Self-cleaning
viii. Chemical inertness
ix. Physical stability
x. Superhydrophilic
xi. Stable in the presence of aqueous electrolyte solutions
xii. Relatively inexpensive and readily available

Zinc oxide has the same band gap as TiO_2 and it seems to be a suitable alternative but it degrades during repeated photocatalytic cycles and cannot be used for technical

applications. Cadmium sulphide has a lower band gap of 2.42 eV compared to TiO_2, but it suffers from photo-corrosion induced by self oxidation leading to depressed photoactivity and the release of Cd^{2+} which are dangerous pollutants (Domenech & Prieto, 1986).

2.4 Synthetic methods for TiO_2 particles

There are various techniques for preparing TiO_2 nanoparticles and these include reverse micelles, the sol-gel process, the metal organic chemical vapor deposition (MOCVD) (Wu & Yu, 2004), gas phase (aerosol) synthesis (Pratsinis,1998), wet chemical synthesis by precipitation of hydroxides from salts, microemulsion-mediated methods (Kumar et al, 1993) and electrochemical synthesis. These methods can be divided into five general groups namely sol-gel, deposition methods, sonochemical and microwave assisted methods, hydro/solvo-thermal methods and oxidation methods.

2.4.1 Oxidation methods

These methods involve the oxidation of titanium metal using oxidants or anodization. Anodization of titanium sheet under a voltage between 10 and 20 V in 0.5 % hydrogen fluoride leads to the formation of aligned TiO_2 nanotubes whose diameter is controlled by varying the applied voltage (Xiaobo, 2009). In another study, crystallized TiO_2 nanotubes were obtained when anodized titanium plate was heat treated at 500 °C for six hours in an oxygen environment (Varghese et al, 2003). Direct oxidation of the titanium metal with hydrogen peroxide has also been found to lead to the formation of TiO_2 nanorods (Wu et al, 2005).

2.4.2 Sonochemical and microwave assisted methods

The sonochemical method has been applied to produce highly photoactive TiO_2 nanoparticles by the hydrolysis of titanium tetraisopropoxide (TTIP) in pure water or in an ethanol/water mixture under ultrasonic radiation (Yu et al, 2001). Sonochemistry arises from *acoustic cavitation* which is the formation, growth and collapse of bubbles within a liquid medium. Heat (~5 000 K) and high pressures (~1000 atm) are produced by cavitational collapse (Xiaobo, 2009).

Microwave radiations can also be applied to produce various TiO_2 nanomaterials (Gressel et al, 2005). In industrial processing this method has an advantage of rapid heat transfer and selective heating. The colloidal TiO_2 nanoparticles can be prepared in a short period of time (within 5 to 60 minutes) compared to several hours needed for the conventional methods of forced hydrolysis at high temperatures (~ 195 °C) (Corradi et al, 2005). TiO_2 nanotubes which are open-ended and multi-walled with diameters of 8–12 nm and lengths between 200–1000 nm were also prepared using this method (Wu et al, 2005).

2.4.3 Deposition methods

In these methods, materials in the vapor state are condensed to form a solid phase material. The process is normally carried out in a vacuum chamber and if a chemical reaction takes place it is called chemical vapour deposition (CVD) and physical vapour deposition (PVD) if no reaction occurs. Examples of CVD include electrostatic spray hydrolysis, diffusion flame pyrolysis, thermal plasma pyrolysis, ultrasonic spray pyrolysis, laser-induced pyrolysis, and ultrasonic-assisted hydrolysis. TiO_2 films with grain size less than 30 nm and TiO_2 nanoparticles with sizes less than 10 nm were

synthesized by pyrolysis of TTIP in a helium/oxygen atmosphere (Seifried et al, 2000). Thermal plasma synthesis (Ishigaki et al, 2004) and spray pyrolysis (Gablenz et al, 1998) have been used in some studies but they are complex, capital and energy-intensive and the properties of the powder are not easy to control.

2.4.4 Hydro/solvo-thermal methods

These are two processes, solvothermal and hydrothermal which are almost similar. The process is carried out in autoclaves under controlled temperature and pressure. It allows the use of temperatures above the boiling point of water/organic solution. Compared to hydrothermal method, the solvothermal method uses a non-aqueous solvent, has better control of the properties of TiO_2 and the temperature can be increased much higher meaning high boiling point solvents can be used. Treatment of titanium tetrachloride solution saturated with sodium chloride at 160 °C for 2 hours produced TiO_2 nanorods (Feng et al, 2005). The solvothermal method was used to prepare TiO_2 of good quality without the use of surfactants (Kim et al, 2003).

2.4.5 Sol-gel methods

A sol-gel process can be defined as the conversion of a precursor solution to an inorganic solid through polymerization reactions induced by water. Hydrolysis forms a sol which is basically a dispersion of colloidal particles in a liquid, and condensation leads in the formation of a gel. Compared to the methods discussed above, the sol-gel process is very promising for synthesis and preparation of inorganic and organic-inorganic hybrid nanomaterials because it allows the use of low processing temperatures (<100 °C) and molecular level composition homogeneity (Attar et al, 2008). Particle size, shape and

distribution are easy to control using the sol-gel method. Figure 2.3 shows the various steps to control the final morphology of the product using the sol-gel process.

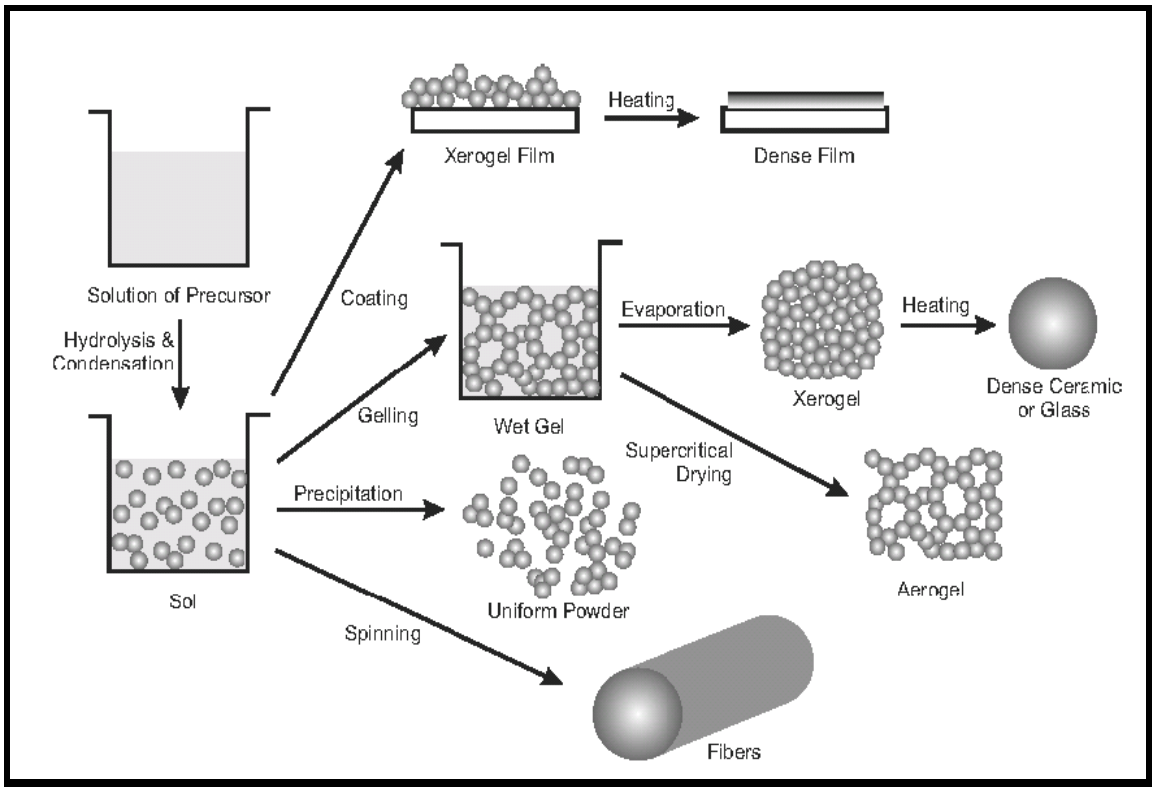

Figure 2.3: Different sol-gel steps to control the final morphology of the product (Livage et al, 1998).

The sol-gel process produces fine, spherical powders of uniform size and has been widely used to synthesize TiO_2 materials and normally proceeds via an acid-catalyzed step of titanium (IV) alkoxides (Oskam et al, 2003). One of the most attractive features of the sol-gel process is the possibility to shape the resulting material into desired forms such as fiber, film and monodispersed powder.

Typical precursors are metal oxides and metal chlorides. A metal alkoxide consists of an M-O-R linkage where M is the metal, O is oxygen and R is an alkyl group. The

polarization that takes place in the M-O bond makes it susceptible to nucleophilic attack. In the presence of water, the alkoxide undergoes a nucleophilic substitution reaction in which the alkoxy groups (OR) are replaced by the hydroxyl groups from water and this process is called hydrolysis. The metal hydroxide groups will link and generate a hydrated metal-oxide network which eventually forms small nuclei and this process is called condensation. The general sol-gel process is described in Figure 2.4.

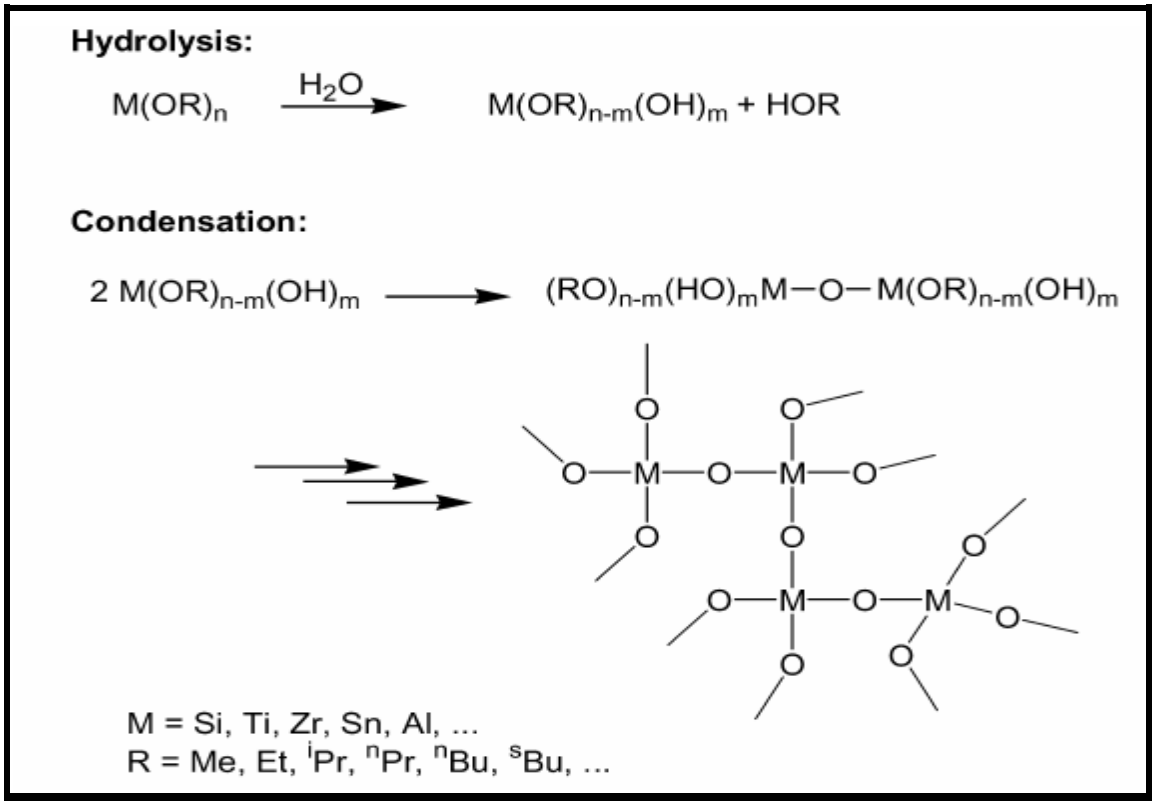

Figure 2.4: Sol-gel process (Brinker, 1990).

Metal alkoxides used for the sol-gel process are generally very reactive and thus there is need for controlling the reactivity in order to obtain sols and gels with desirable properties by using modifiers or addition of chelating ligands such as *β*-diketones, carboxylic acids or other complex ligands (Attar et al, 2008). These modifiers react with

alkoxides giving rise to new molecular precursors that can be used in sol-gel processing to provide better control of the hydrolysis-condensation process. These new precursors reduce reactivity and functionality, prevent condensation and lead to formation of species that are smaller. Livage *et al*, 1998 investigated the use of acetylacetone to improve the sol–gel processing of metal alkoxides.

Modification by modifiers reduces the number of M-OR bonds available for hydrolysis and thus hydrolytic susceptibility. If β-diketones are used they decrease the nuclearity resulting in small particles since these ligands are surface capping reagents and polymerization lockers. Carboxylate ligands such as acetic acid mostly act as bridging chelating ligands.

2.5 Process parameters affecting properties of TiO_2

There are various parameters that influence the size and properties of the TiO_2 particles produced via the sol-gel process. To get TiO_2 particles with desirable properties, the parameters that influence hydrolysis and condensation reactions of the sol-gel process should be controlled. It has been established that some parameters are more important than others. The parameters include pH, nature and concentration of the catalyst, water/precursor molar ratio, reaction temperature, precursor concentration, type of solvent and type of precursor (Ding et al, 1995: Arroyo et al, 1993).

2.5.1 Influence of precursor concentration

Particle size increase with increasing precursor concentration due to enhanced coagulation and sintering resulting from the large concentration of TiO_2 nuclei generated at high TTIP precursor concentrations (Jang et al, 1995). Increase in precursor

concentration increases the crystallinity of the anatase, and enhances transformation from anatase to rutile. (Kim et al, 2005).

2.5.2 Influence of water content

The amount of water is a crucial parameter in controlling the hydrolysis reaction. Xiaobo (2009) reported that the development of Ti-O-Ti chains through alcoxolation is favoured when the content of water is low, with low hydrolysis rates and excess titanium alkoxide in the reaction mixture. Figure 2.5a shows the products of partial and complete hydrolysis to form monomers.

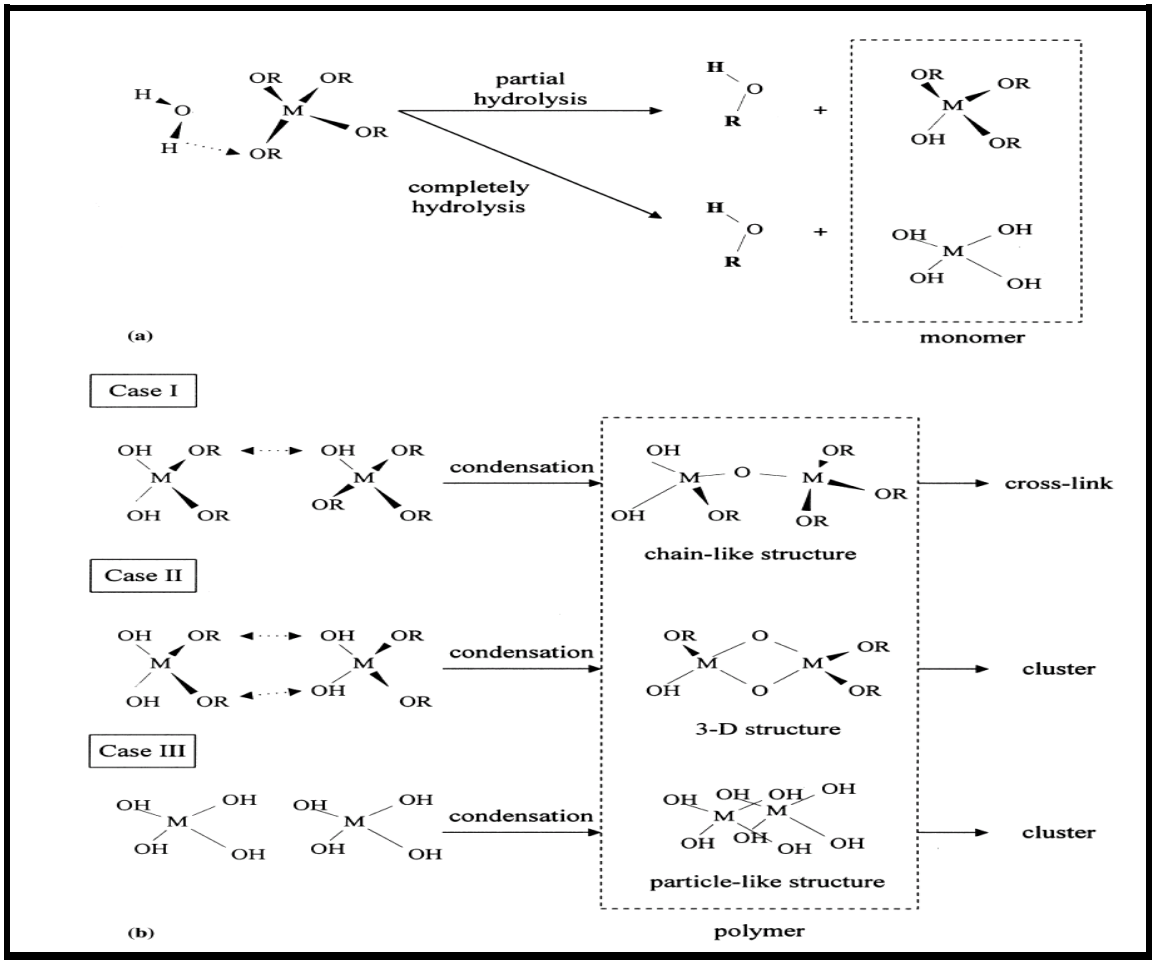

Figure 2.5: Schematic diagram showing sol-gel reactions (Yu et al, 2000).

The amount of water should not be too low otherwise the hydrolysis of the alkoxides with water will be incomplete and condensation occurs between the monomers of $(OH)_xTi(OR)_{4-x}$ (Fu et al, 2000) as illustrated in Case I in Figure 2.3b. Other researchers reported that the ratio of water to the alkoxide required for particle formation should be greater than 2.5 as deduced from the equation R= $[H_2O]/[TEOT]$ >2.5 (Barringer & Bowen, 1982). The largest R value reported was 7 which gave particles with average size of 300 nm. If the amount of water is increased, a stronger nucleophilic reaction between water and alkoxide molecules occurs resulting in more alkoxyl groups being substituted by OH groups of water. The monomers obtained then interact with each other to form a three dimensional network structure as shown in Figure 2.3b Case II. When R is over a critical value, the hydrolysis is more complete and more alkoxides convert to the corresponding metal hydrates, $M(OH)_z$ which then react with each other to form particle-like polymers as shown in Figure 2.5, Case III (Fu et al, 2000). The formation of $Ti(OH)_4$ is favoured by high hydrolysis rates caused by large amounts of water.

2.5.3 Influence of pH

The pH of the sol-gel system for the preparation of uniform nanoparticles of anatase titania from condensed TiO_2 gel is a key factor for controlling the final particle size and shape of the product (Sugimoto et al, 1997). The grain size of the TiO_2 particles generally increases with increase in pH of the sol (Johromi et al, 2009). When the hydrogen ion concentration is high the particles grow rapidly to form large grains because the hydrogen ions interfere in the reaction and decrease the nucleation rate. The new nucleus has enough time to grow and aggregate into large TiO_2 particles (Chai et al, 2007). Matijevic *et al,* 1997) reported the synthesis of TiO_2 spherical particles of a narrow size by aging a highly acidic solution of titanium tetrachloride at elevated temperatures for 6 to 47 hours.

The amount of acid (pH) determines not only the size of the nanoparticles but also the stability of the sol (Vorkapic & Matsoukas, 1998).

2.5.4 Influence of temperature

The sol-gel temperature is a critical parameter in controlling the properties of the resulting TiO_2 nanoparticles. Vorkapic & Matsoukas, 1998 studied the effect of the hydrolysis temperature on particle size where they varied the temperature between 0 and 50 °C and they found out that low hydrolysis temperatures favored formation of larger particles. When the temperature was increased, the size decreased and reached a minimum in the range 25 - 50 °C. High temperatures increase the thermal energy of the colloid, decreases viscosity and the dielectric constant of the solvent, thus lowering the electrostatic barrier against aggregation resulting in larger particles (Moon et al, 1995).

2.5.5 Influence of precursor type

Vorkapic & Matsoukas investigated the effect of different alkoxides on the size of the TiO_2 nanoparticles and they found out that at 25 °C the final size decreases with increase in the length of the alkoxy group. Their results showed that particle size decreased in the order ethoxide > propoxide ≥isopropoxide > butoxide, corresponding to the order of decreasing reactivity of the alkoxide hence the lower hydrolysis rate.

2.5.6 Influence of type of solvent and concentration

In general, after nucleation the particles grow by molecular addition or aggregation and this particle growth is affected by the kinds of solvents used because particle interaction potential is different in each solvent. The increase in the amount and molecular weight of the alcohol was found to increase the size of the particles and the smallest size was

obtained when no alcohol was used (Vorkapic & Matsoukas, 1998). This is due to the fact that an increase in both concentration and molecular weight leads to a decrease in the dielectric constant of the solvent resulting in decreased stability and enhanced rate of re-aggregation and larger particle size. The formation of TiO_2 from thermal hydrolysis of titanium tetrachloride in water/n-propanol mixtures was investigated by Park et al (2006). The study showed that when powders were redispersed in various solvents the degree of aggregation increased in the order: methanol>ethanol>propanol suggesting that colloidal destabilization was the primary mechanism by which these alcohols influenced particle size.

In another study by Xu et al, 1999, the photocatalytic activity of unsupported TiO_2 gradually increased with increase in the chain of the solvent used in preparation due to the increase in the content of anatase and a decrease in particle size. They found out that when the solvent was changed from methanol to 2-pentanol, the content of anatase increased from 68 % to 91 % with a decrease in particle size from 11.6 nm to 10.5 nm. The increase in alcohol concentration in the sol-gel reaction mixture can slow down the hydrolysis rate and the resulting sol would possess a high content of amorphous TiO_2 (Xu et al, 1998).

2.6 Applications of TiO_2

In the chemical industry, TiO_2 was introduced in the 1900's to replace toxic lead oxides as a white pigment (Feng et al, 2006). It is used as a pigment in paints, paper, plastics and cosmetic products. The use of TiO_2 increased in the last few years as a photocatalyst, gas

sensor, catalyst support or promoter and so on. In this study it is going to be used as a photocatalyst in water treatment.

2.6.1 Application in solar water splitting

A lot of research has been done to study the properties and applications of TiO_2 with UV irradiation since the discovery of the photocatalytic splitting of water on a TiO_2 electrode (Tryk et al, 2000). The photocatalytic splitting of water into hydrogen and oxygen using TiO_2 materials is ideal for clean and sustainable energy sources. Under UV illumination, the photogenerated electrons and holes cause redox reactions. The water molecules are oxidized by the holes to form oxygen and reduced by electrons forming hydrogen and this leads to the overall splitting of water. For the effective water splitting of water, the bottom level of the conduction band should be more negative than the reduction potential of H^+/H_2 (0 Vs normal hydrogen electrode) and the top level of the valence band should be more positive than the oxidation potential of O_2/H_2O (1.23 V).

2.6.2 Application in photovoltaics

TiO_2 nanocrystalline electrodes have been used in dye-sensitized solar cell (DSSC) (Gratzel, 2000 & 2001) where they are placed in contact with a redox electrolyte. The performance of the DSSC depends on the structure and properties of TiO_2 electrodes such as mesoporosity and crystallinity which enhance adsorption of the dye (Xiaobo et al, 2009). The solar cells were reported to show high efficiencies when TiO_2 nanotubes were used as electrodes due to an increase in electron density (Ohsaki et al, 2005). The doped TiO_2 especially N-TiO_2 electrodes were found to be more efficient than pure TiO_2 due to the increase in the photo-induced current using visible light (Lindgren et al, 2003).

2.6.3 Application as a catalyst support or promoter

The role of TiO_2 in catalytic activity is to increase catalyst surface area. Interactions between catalyst and TiO_2 may occur leading to changes in reactivity and selectivity (Martin et al, 1991). Satterfield reported that V_2O_5 supported on TiO_2 was a superior catalyst compared to unsupported V_2O_5 when used for partial oxidation reaction of many hydrocarbons or selective catalytic reduction of nitric oxides (Satterfield, 1991).

Although TiO_2 is not good when used as a structural support material for metals compared to other semiconductors such as Al_2O_2 and SiO_2, its addition in small quantities can modify metal-based catalysts significantly. For example Au/TiO_2 has been used for carbon monoxide oxidation at low temperature (Boccuzzi, 1996).

2.6.4 Application in photocatalysis

TiO_2 has been used for photo-assisted degradation of organic compounds, pollutant air cleaning (Mills & Hunte, 1997: Peral, 1992), reduction of inorganic compounds and indoor odour removal (Kim, 2002). Some other uses include, self-cleaning (Blossey, 2003), antifogging film on vehicle windscreens (Paz, 1995) and photo-killing of pathogenic organisms for example in hospitals (Maness, 1999).

2.6.5 Application as a white pigment

Titanium dioxide is an intense white pigment because of its high refractive index that is chemically inert, resists fading in sunlight and is very opaque. It is used in paints for buildings, wood or furniture, industrial coatings and automobile finishes. It is corrosion protective, absorbs UV and protects paint from direct photochemical degradation of

organic binder making it very useful for the paint industry (Preuss, 1974). It is also used in thin film optical devices as a pigment including in anti-reflective coatings and dielectric mirrors for lasers due to its excellent optical transmittance.

In the paper industry, TiO_2 is used with clay, $CaCO_3$, and other pigments to give brightness and the loading differs depending on the quality of the paper pulp to meet specific performance and cost goals (Braun et al, 1992). In addition, pure TiO_2 is an effective sun screener so it is applied to cosmetic products (Hewitt, 1999).

2.7 Photocatalysis

Heterogeneous photocatalysis includes a variety of reactions such as organic synthesis, water splitting, hydrogen transfer, metal deposition, photo-reduction, water detoxification, gaseous pollutant removal and anti-cancer therapy. It is a rapidly expanding technology for water and air treatment. Generally, it can be defined as the acceleration of a photoreaction in the presence of a catalyst. It started in 1972 when Fujishima and Honda discovered the photochemical splitting of water into hydrogen and oxygen with titanium dioxide (Fujishima & Honda, 1972). Some years after the discovery of the photo-electrolysis of water on TiO_2, Bard and Frank (1977) discovered that cyanide in water can be decomposed by TiO_2 under ultraviolet light irradiation. Their results were very useful because they showed that there is a potential application of photocatalysis in the field of environmental purification.

Recently, interest has been focused on advanced oxidation processes especially the use of semiconducting metal oxides to remove organic and inorganic contaminants.

Heterogeneous photo-catalytic oxidation using TiO_2 received more attention as an alternative method for both air and water streams (Gaya & Abdullah, 2008). The main advantage of photocatalysis in water treatment is that there is no residue of the original material that remains and thus no sludge requiring disposal is produced because the process breaks down the contaminants into harmless inorganic products (CO_2, H_2O etc). Some other advantages include:

i. The process can be powered by natural sunlight which is free thus reducing significantly the electrical power requirements and operating costs.
ii. No consumable chemicals are required
iii. Operation of equipment involved is simple
iv. It is environmentally friendly

The initial process in photocatalysis is the generation of electron-hole pairs. When a semiconductor is irradiated with a photon of energy (*hv)* that exceeds its band gap energy (Eg) there is an excitation of an electron from the valence band (VB) to the conduction band (CB), leaving a positive hole behind. The excited-state conduction band electrons and valence-band holes can do the following:

i. It can recombine and dissipate the energy as heat if there is no suitable electron and hole scavengers.
ii. It can get trapped in the metastable surface states
iii. It can react with electron acceptors and electron donors adsorbed on the surface of the semiconductor.

2.7.1 Mechanism of TiO_2-assisted photocatalytic degradation

Photocatalysis over titanium dioxide is initiated by the absorption of a photon with energy equal to or greater than the semiconductor band gap (3.2 eV). This energy is used to promote an electron from the valence band (VB) to the conduction band (CB) producing electron-hole pairs (*e-/h*$^+$).

$$TiO_2 \xrightarrow{h\nu} e_{cb}^-(TiO_2) + h_{vb}^+(TiO_2) \qquad (2.1)$$

A simplified mechanism for the photo-activation of titanium dioxide catalyst is shown in Figure 2.6.

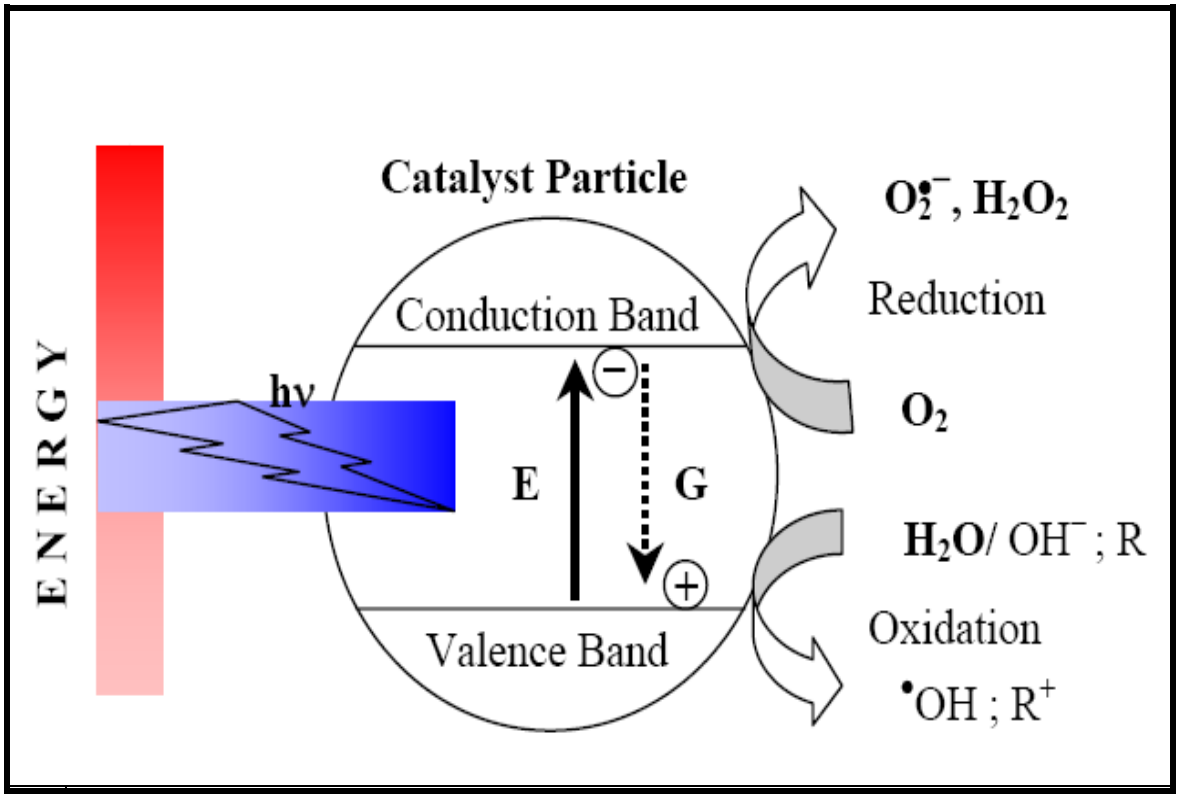

Figure 2.6: Mechanism for activation of TiO_2 (Rasheed, 2005)

The conduction band electron is strongly reducing and the valence band hole is strongly oxidizing so these will reduce and oxidize the adsorbed species on the semiconductor

respectively. The reduction of adsorbed oxygen (O_2) to oxygen radical ($O_2^{\cdot -}$) is normally the most important reaction of the conduction band electron. Oxidation of water or hydroxyl group (OH^-) by the hole produces the hydroxyl radical ($^{\cdot}OH$) which has a high oxidation potential (2.8V) and is indiscriminant in its reactions. The surface bound OH radicals rapidly attack pollutants at the surface.

2.7.2 Mechanism of generation of oxidation species

The oxidation pathway follows five steps and these are:

i. the diffusion of reactants to the photocatalyst surface

ii. adsorption of reactants onto the photocatalyst surface

iii. reaction on the surface

iv. desorption of products from the surface

v. diffusion of products from the surface

Only the molecules that are in direct contact with the catalyst surface undergo photocatalytic degradation. The oxidation of water and hydroxyl group by the valence band "hole" (h_{vb}^+) on the TiO_2 surface is shown in Equation 2.2 and 2.3.

$$TiO_2\ (h_{vb}^+) + H_2O_{ads} \longrightarrow TiO_2 + HO^{\bullet}_{ads} + H^+ \qquad (2.2)$$

$$TiO_2\ (h_{vb}^+) + HO^-_{ads} \longrightarrow TiO_2 + HO^{\bullet}_{ads} \qquad (2.3)$$

The electron in the conduction band will react with an adsorbed electron acceptor such as oxygen to form a superoxide ion ($O_2^{\cdot -}$) according to Equation 2.4.

$$TiO_2\,(e_{cb}^-) + O_{2\,ads} + H^+ \longrightarrow TiO_2 + HO_2^{\cdot} \longrightarrow O_2^{\cdot -} + H^+ \quad (2.4)$$

Hydrogen peroxide could also be formed via Equation 2.5.

$$TiO_2\,(e_{cb}^-) + HO_2^{\cdot} + H^+ \longrightarrow H_2O_2 \quad (2.5)$$

The UV light can also act on the produced hydrogen peroxide generating more hydroxyl radical according to Equation 2.6-2.8.

$$H_2O_2 \xrightarrow{h\nu} 2HO^{\cdot} \quad (2.6)$$

$$H_2O_2 + O_2^{\cdot -} \longrightarrow HO^{\cdot} + O_2 + HO^- \quad (2.7)$$

$$H_2O_2 + TiO_2\,(e_{cb}^-) \longrightarrow HO^{\cdot} + HO^- + TiO_2 \quad (2.8)$$

2.7.3 Pollutants that can be removed from water by TiO_2

2.7.3.1 Inorganic anions

Toxic anions can be oxidized to harmless or less toxic compounds by TiO_2 photocatalyst, for example nitrite is oxidized to nitrate; sulphide, sulphite and thiosulphate are converted to sulphates and the cyanide is converted to nitrogen or nitrate (Pollema et al, 1992).

2.7.3.2 Noble metals

Heavy metals which are toxic can be removed from waste water (Chen & Ray, 2001). They are reduced to zero oxidation states and are recovered as small crystallites deposited on the photocatalyst surface provided that the redox potential of the metal is more positive than that of the semiconductor. For example if mercury (II) is present it will be

reduced to mercury (0). This ability to reduce metal cations makes TiO_2 applicable in the recovery of silver from photographic baths. The silver forms small crystallites and as the photo-deposition increases, the metal particles form agglomerates that are bigger than the TiO_2 particles (Hermann et al, 1988). Other metals that can be removed from water by TiO_2 photocatalyst include gold, platinum, palladium and copper.

2.7.3.3 Organic compounds

TiO_2 photocatalysts have been used to oxidize a significant number of organic compounds such as phenols, chlorophenols, halocarbons, surfactants, pesticides and textile dyes. In most cases, the organic compounds were completely mineralized into harmless compounds such as CO_2 and H_2O. Liu et al, 2008 reported that TiO_2 is effective in the removal of humic acid which causes undesirable taste and colour in drinking water. Rhodamine B, a widely used colorant in textiles and foodstuffs which can cause irritation to human skin, eyes and respiratory tract has also been successfully removed from water by TiO_2 photo-catalyst (Luo et al, 2009).

2.7.3.4 Micro-organisms

Recently, photocatalysis on TiO_2 was reportedly used for the destruction of microorganisms such as bacteria and viruses and for the inactivation of cancer cells (Sakai et al, 1995; Kikuchi et al, 1997). Maness et al, 1999 reported that reactive oxidation species such as superoxide anions and hydroxyl radicals promoted oxidation of unsaturated phospholipids in microorganisms. Kuhn et al, 2003 suggested that the destruction of microbes took place through direct damage to cell walls caused by hydroxyl radicals and they also documented the use of TiO_2 disinfection on *E. coli*,

Pseudomonas aeruginosa, Staphylococcus aureus and Enterococcus faecium. The formation of hydroxyl radicals on the surface of the photo-catalyst is believed to account for the surface sterilizing property of TiO_2 (Fujishima et al, 1999). A TiO_2 photo-catalyst was also found to be effective for the removal of Pseudomonas aeruginosa, a microorganism that has the highest pathogenic effect in human and is resistant to chlorine and other oxidizing agents (Daneshvar et al, 2007).

2.8 Influence of operational parameters

2.8.1 Effect of mass/concentration of a photocatalyst

The rate of the reaction was found to be directly proportional to the mass of a catalyst, but above a certain value of mass, the reaction rate was found to level off and become independent of mass (Hermann, 1999). In general the optimum catalyst concentration must be determined to avoid excess catalyst and ensure good adsorption of efficient photons (Saquib & Muneer, 2003). If catalyst loading is too much, there could be unfavourable light scattering and reduction of light penetration into the solution (Chun et al, 2000). The limit depends on the working conditions of the photo-reactor. It was found that 1.3 mg TiO_2/cm^2 was the limit for a fixed bed, 2.5 mg TiO_2/cm^3 for suspension and 2.5 g/L using a batch photoreactor (Hermann, 1999). These limits correspond to the maximum amount of TiO_2 when the whole surface is exposed and fully illuminated.

2.8.2 Effect of light intensity

Increase in light intensity increases the photo-catalytic reaction although the nature or form of light has no affect on the pathway of the reaction (Stylidi et al, 2004). Of the total natural light, only 5 % has enough energy to cause effective photosensitization (Wilke &

Breuer, 1999). The overall quanta of light absorbed by a photocatalyst is given by the following equation (Kim et al, 2003).

$$\Phi\text{overall} = \frac{rate\ of\ reaction}{rate\ of\ absorption\ of\ light} \qquad (2.9)$$

Metal oxides such as TiO_2 in a heterogeneous system cannot absorb all incident light due to refraction and this makes it quite difficult to determine the quantum yield experimentally.

2.8.3 Effect of wavelength

The rate of reaction varies with the wavelength and it follows the absorption spectrum of the photocatalyst and generally decreases with an increase in wavelength (Herrmann, 1999). The threshold should correspond to the band gap, for instance TiO_2 which has a band gap of 3.02 eV requires light of $\lambda \leq 400$ nm.

2.8.4 Effect of pH

The pH of the solution is a very important parameter because it dictates the surface charge properties of the photocatalyst and size of aggregates it forms (Haque & Muneer, 2007). It has been reported that titanium dioxide is strongly oxidizing at low pH but at very low pH there is excess H^+ which retards the rate of reaction (Sun et al, 2006).

2.8.5 Reaction temperature

Photocatalytic systems do not require heating, they operate at room temperature. In general high temperatures favour recombination of charge carriers and desorption of

adsorbed reactant species, resulting in a decrease in photocatalytic activity. In the temperature range 20 $^{\circ}$C – 80 $^{\circ}$C, the true activation energy (E_t) is zero while the apparent activation energy (E_a) is usually very small. At temperatures below 0 $^{\circ}$C, E_a increases and desorption of the final product becomes the rate limiting step. At temperatures above 80 $^{\circ}$C, E_a becomes negative and the exothermic adsorption of a reactant will not be favoured and tends to be the rate limiting step (Hermann, 1999).

2.8.6 Influence of the nature of a photocatalyst

Surface morphology particularly particle size and agglomerate size greatly influence the performance of the photocatalyst (Dinga et al, 2005). The photomineralisation of organic compounds over TiO_2 was found to be higher when particle size of the catalyst was in the nano-range (Maira et al, 2001). Since the reaction takes place in the adsorbed phase, the smaller the particle the higher the surface area for adsorption hence the higher the degree of degradation.

2.8.7 Influence of the adsorption nature and concentration of the substrate

Since reaction takes place only in the adsorbed phase of the semiconductor particle, it means that those substances that can adhere effectively to the surface of the photocatalyst are more susceptible to direct oxidation. The degradation of aromatic compounds depends on the substituent group, for instance nitrophenol degrades faster than phenol because it is a stronger adsorbate than phenol (Bhatkhande et al, 2004). Generally compounds with electronegative atoms such as nitrobenzene and benzoic acid are good adsorbates in the dark compared to those with electron donating groups (Palmisano et al, 2007).

The concentration of the substrate on the photocatalyst depends on the rate of its degradation. If the rate of degradation is lower than the rate of accumulation of the substrate, it results in the saturation of the surface of the photocatalyst that diminishes photonic efficiency thus leading to catalyst deactivation (Arana et al, 2004).

2.9 Ways of improving photocatalytic efficiency

The photocatalytic activity of titanium dioxide depends on several parameters such as the method of preparation, particle size, reactive surface area and anatase to rutile ratio (Hoffmann et al, 1995; Brus, 1986). There are several ways to improve the photocatalytic activity of titanium dioxide and these include increasing its specific surface area and decreasing the size of the particles (Addamo et al, 2005). The development of a practical photocatalytic system on an industrial scale focuses on the cost effectiveness of the process. The use of expensive solar concentrators and artificial ultraviolet (UV) irradiation for photocatalytic reactions has a negative impact on the cost effectiveness of the system.

Although it has been shown that titanium dioxide surfaces perform under direct sunlight, it is only a small percentage of light (5 % UV) that can activate the surface. The abundance of the visible light (55 % compared to 5 % of UV) motivates a great deal of research to enhance the effectiveness of TiO_2 and to increase the spectral response in the visible region. The band gap of bulk TiO_2 is 3.0 eV for rutile and 3.2 eV for anatase phase. Thus one of the goals in this study was to improve the performance of TiO_2 by increasing its optical activity by shifting the onset of the response from UV to the visible region. Several ways are available for achieving this goal and these include doping,

sensitization with other colourful inorganic or organic compounds and modification of the surface with other semiconductors (Xiaobo 2009). The different ways of improving the optical properties of TiO_2 are shown in Figure 2.7. These include doping metal ions into the TiO_2 lattice and coupling semiconductors or dyes.

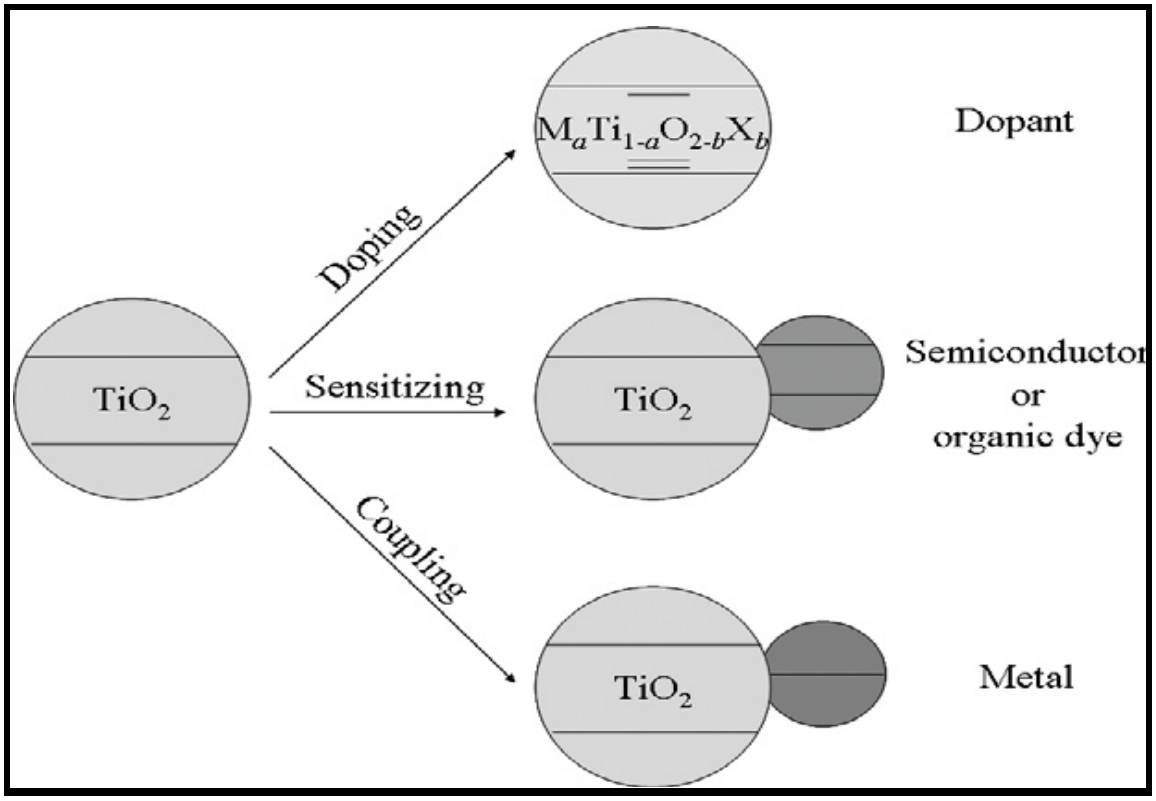

Figure 2.7: Modification paths for TiO_2 nanomaterial (Xiaobao, 2009).

2.9.1 Use of doping

Doping can be done using non metals such as carbon, nitrogen and fluorine or transition metals such as platinum, iron and cobalt. The methods used to prepare doped TiO_2 can be divided into three types: high temperature treatment, wet chemistry and ion implantation. The wet chemistry method which was used in this study involves the hydrolysis of a titanium precursor followed by heat treatment.

The presence of dopants lowers the band gap of the TiO_2 thus producing a more active photocatalyst at higher wavelengths (visible region). There are some drawbacks in metal doping such as low thermal stability of the modified material and increased carrier recombination centres due to strongly localized states within the band gap (Choi et al, 1994). Nonmetal doping may offer a better approach. It has been found that doping with fluorine modifies the electronic structure of TiO_2 by creating oxygen vacancies on the surface due to charge compensation between F^- and Ti^{4+} but without a significant change in spectral response (Li et al, 2005). The oxygen vacancies have been found to enhance photocatalytic activity.

The band structure of doped, stoichiometric and TiO_2 with oxygen vacancies can be described using the model of the band structure. In the band structure of TiO_2, the conduction band is titanium 3d and 4s in character and the valence band is oxygen 2p in character. In TiO_2, all the four electrons from titanium are found in the half-filled oxygen 2p states and this leaves the titanium 3d and 4s orbitals empty forming the conduction band. The filled oxygen 2p orbitals form the valence band. Detailed theoretical analysis confirmed that when an oxygen atom is removed, three 2p orbitals are removed with four electrons and the remaining two electrons from titanium localize on two adjacent titanium atoms reducing them to Ti^{3+} (Henrich, 1976). The schematic representation of the stoichiometric TiO_2, creation of oxygen vacancy, substitutional carbon and interstitial fluorine and boron is shown in Figure 2.8. It is clear that the introduction of dopants such as carbon reduce the band gap by replacing oxygen 2p states in the valence band with 2p states that float up into the band gap. It is believed that this is due to weaker nuclear–electron interaction suggesting that boron doping would reduce the band gap better than

carbon because boron has weaker nuclear-electron interactions than carbon (Nie et al, 2009). The computer band structure $T_{14}O_7B$ supercell is shown in Figure 2.6.

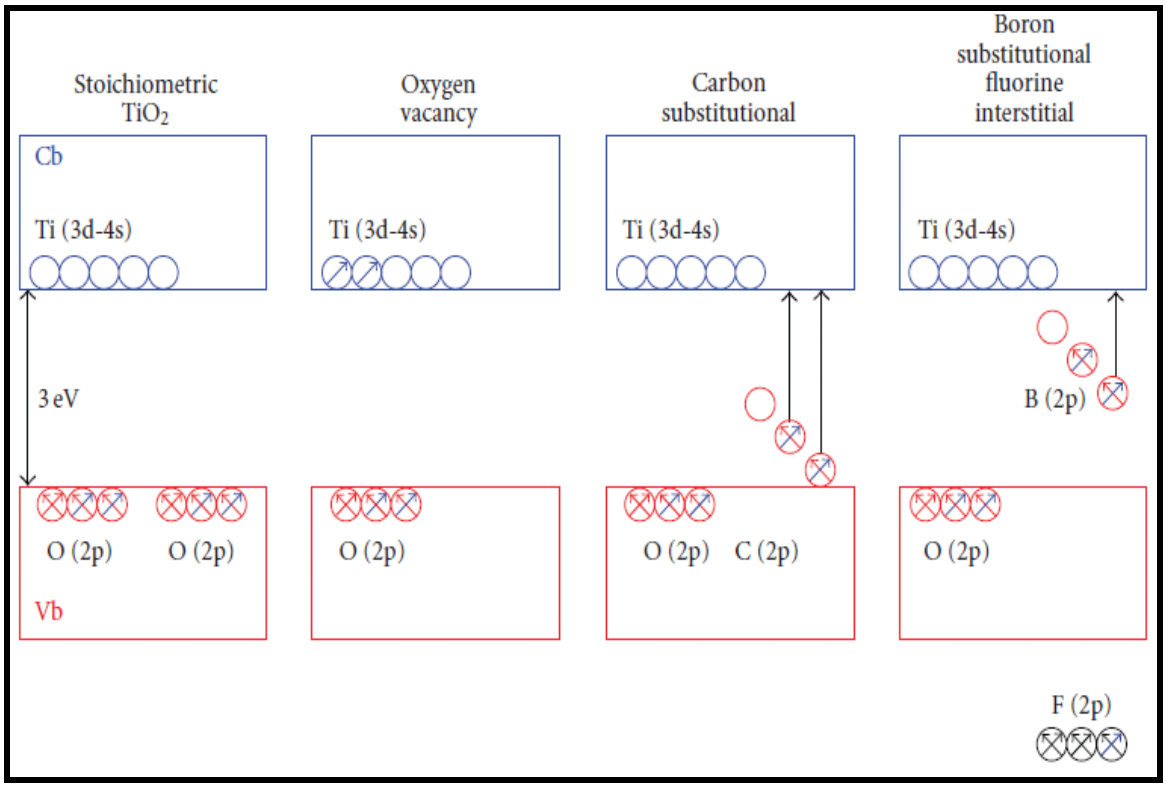

Figure 2.8: Schematic representation of the electronic structure of TiO_2 (Nie et al, 2009).

2.9.1.1 Carbon doping

Titanium dioxide in the anatase form doped with carbon was found to decompose gaseous 2-propanol into carbon dioxide and acetone under visible light irradiation (Irie et al, 2003). The carbon substitutes some of the lattice titanium atoms close to and on the surface of TiO_2 and form a Ti-O-C structure. There are different methods available for doping TiO_2 with carbon and these include flame oxidation, heating titanium carbide (Choi et al, 2004), chemical vapour deposition (Chen et al, 2003), sol-gel process in the presence of glucose or other carbon sources, annealing TiO_2 under carbon monoxide gas

flow at high temperatures (500–800 °C) (Park et al, 2006), or by direct burning of a titanium metal sheet in a natural gas flame (Khan et al, 2002). If flame oxidation is used to prepare carbon doped TiO_2, the carbon partially substitutes for some of the lattice oxygen atoms (Khan et al, 2002). It has been proposed that if glucose is used in doping TiO_2, it may be reduced to carbonaceous species that become embedded in the TiO_2 matrix. This may lead to the formation of new active sites which are also responsible for higher catalytic activity (Ren et al, 2007).

Organic compounds useful for doping should have a decomposition temperature of less than 300 $^{\circ}$C (United States Patent, 2009). Materials containing carbon, such as wood, activated carbon and particularly hydrocarbons with at least one functional group proved to be suitable in other studies. The functional group can be COOH, NH_x, SH_x, OH, CHO and COOR in which R is an aryl or alkyl group (United States Patent, 2009). Glycerol, succinic acid, ethylene glycol, sugars and carbohydrates can be used as the carbon source. A mixture of some of the compounds mentioned above can be suitable, most preferably the water soluble ones. The organic compound should have the greatest possible affinity for the surface of the parent titanium compound, in order to be able to enter into an intimate bond with the latter. The carbon source can be used in the form of a solid or solution.

2.9.1.2 Nitrogen doping

There are different methods that can be used to dope TiO_2 with nitrogen. Sato et al, 2009 prepared nitrogen doped TiO_2 films by atmospheric controlled pulsed laser deposition. Optical absorption studies on nitrogen doped TiO_2 indicated band gap narrowing (Irie et

al, 2003). This was a result of the mixing of nitrogen 2p states with the oxygen 2p states. Based on recent density functional theory (DFT) calculations, nitrogen doping does not result in band gap narrowing, but instead localized N 2p states/dopant-induced energy levels are formed within the band gap just above the valence band thus increasing the electron-hole pair formation under visible light illumination (Valentin et al, 2004). There are also some changes in the electronic and geometric surface structure due to N^{3-} substituting lattice O^{2-}.

When TiO_2 was co-doped with nitrogen and fluorine, it demonstrated high photocatalytic activity in the visible region. Xie et al managed to decompose methyl orange with N-F-TiO_2 (Xie et al, 2007) and Huang et al, 2006 confirmed strong spectral response in the visible region and high photocatalytic activity of N-F-TiO_2 for the degradation of p-chlorophenol and rhodamine under visible light (Huang et al, 2006). Both concluded that there is a synergistic effect of nitrogen and fluorine doping and this has a significant photocatalytic improvement for degradation of organic compounds compared to nitrogen or fluorine doping alone.

2.9.1.3 Transition metal doping

The influence of transition metal doping has become another area of interest in semiconductor modification and different metals have been used. XingGang et al (2009) studied the effect of 3d transition metal doping with vanadium, chromium and iron using the metal ion implantation method and found out that vanadium showed the highest red-shift. Their results also showed that the shift in the absorption spectra to lower energy increased with increase in dopant concentration. The narrowing of the band gap was due

to the 3d state that lies in the band gap. As the atomic number of the transition metal increased, the 3d level shifted to the valence band and a new 3d level would then appear. The super-cell model of a doped anatase structure is shown in Figure 2.9 and from the structure it is seen that the transition metal dopant replaces some titanium ions.

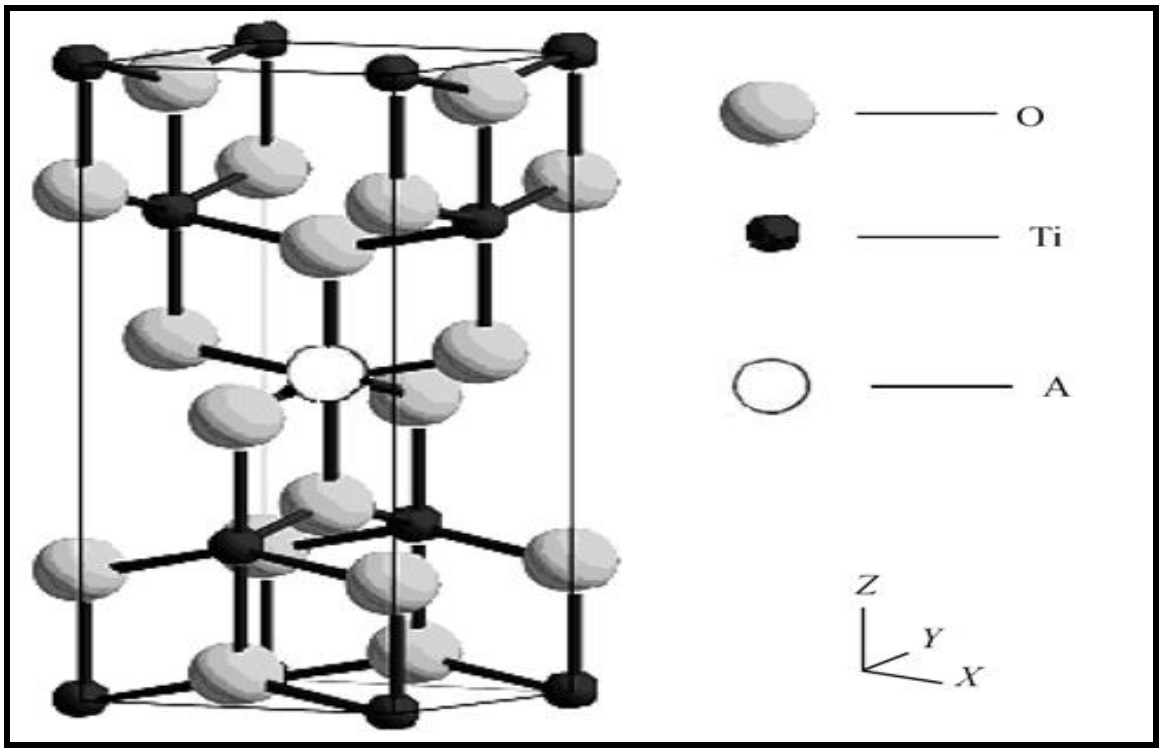

Figure 2.9: The super-cell model of anatase structure, the dark spheres are Ti; the gray spheres are O; the white sphere is the doped atom (XingGang et al, 2009).

Choi et al, 2004 systematically studied TiO_2 doped with 21 metal ions and discovered that the photo-activity improved significantly and influenced the charge recombination rates. Wang et al, 2006 prepared Fe-doped TiO_2 and found out that the dopant promoted the anatase to rutile phase transformation. In general, the photocatalytic activity of transition metal doped TiO_2 depends on several factors such as dopant concentration, electronic configuration of the metal and energy level pattern of the dopant.

2.9.3 Sensitizing mixed oxides

The mixing of semiconductor photocatalysts has a great effect on catalytic activity. Semiconductors that have a narrow band gap have been used as sensitizers to improve the optical absorption properties of TiO_2 in the visible region (Hoyer et al, 1995; Vogel et al, 1994). Semiconductors that can be used as sensitizers include AgI, CdS, PbS, Ag_2S, Sb_2S_3 and Bi_2S_3. It has been reported that TiO_2-SiO_2 binary oxides have a great potential in the degradation of volatile organic compounds (VOCS) (Zou et al, 2006). Figure 2.10 illustrates geometrically the photo-excitation process for a coupled composite semiconductor photocatalyst (Sclafani et al, 1991)

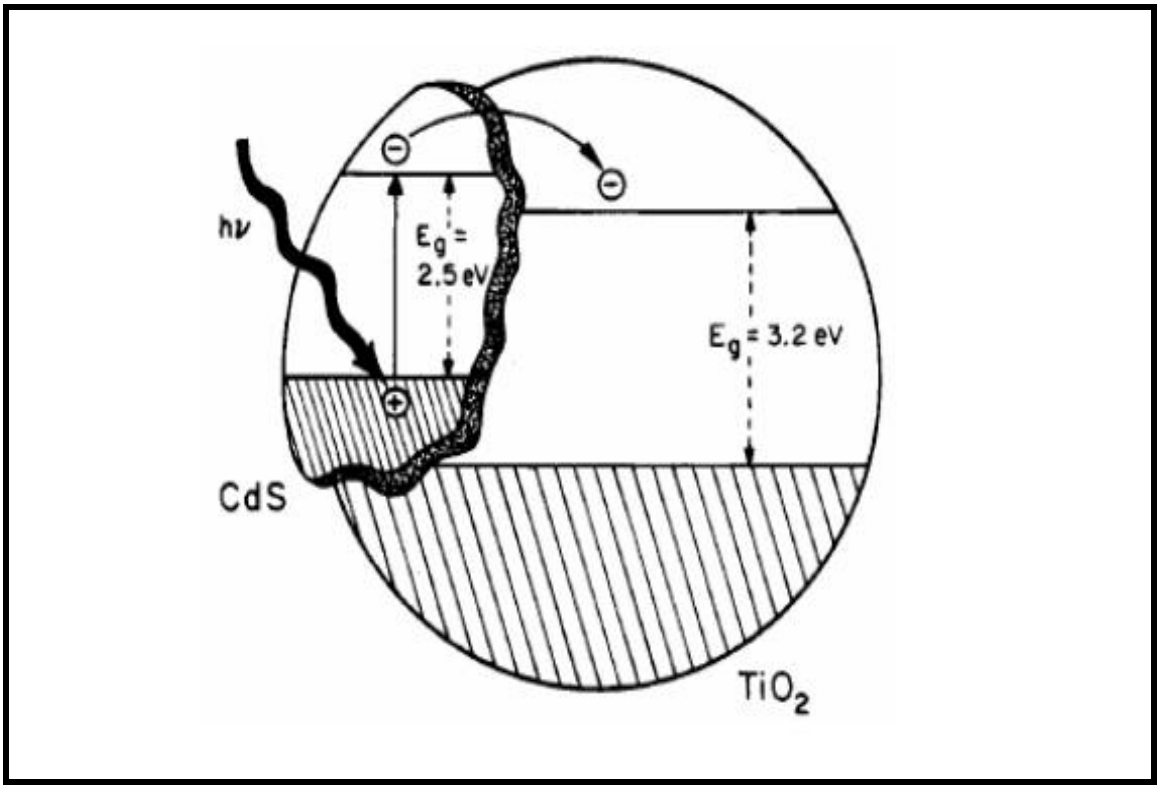

Figure 2.10: Photoexcitation in a composite semiconductor photocatalyst (Sclafani et al, 1991).

When lead sulphide (PbS) nanoparticles of less than 2.5 nm are used as sensitizers, the photo-generated electrons easily move from PbS to TiO_2 leading to strong photo-conductance in the visible region (Hoyer et al, 1995). The use of silver iodide (AgI) results in the stabilization of electron-hole pairs with a lifetime beyond 100 μs and also there will be migration of electrons from AgI to TiO_2 (Fitzmaurice, 1995). The photocatalytic degradation of 2-chlorophenol was found to be enhanced by mixing TiO_2 with CdS due to inter-particle electron transfer (IPET) (Doong, et al, 2001).

The following mechanism for IPET theory has been proposed to describe how electron/hole pairs are generated in photocatalysis (Kuo & Liao, 2006).

$$CdS + h\nu \longrightarrow CdS\,(h^+ + e^-) \qquad (2.10)$$

$$TiO_2 + h\nu \longrightarrow TiO_2\,(h^+ + e^-) \qquad (2.11)$$

$$CdS\,(h^+ + e^-) + TiO_2 \longrightarrow CdS\,(h^+)\,TiO_2\,(e^-) \qquad (2.12)$$

$$CdS\,(h^+ + e^-) + TiO_2\,(h^+ + e^-) \longrightarrow CdS\,(h^+ + h^+) + TiO_2\,(e^- + e^-) \qquad (2.13)$$

The excess electrons on the titanium dioxide nanoparticles can be scavenged by adsorbed oxygen to form superoxide radicals. TiO_2 loaded with ruthenium dioxide showed a very high activity when applied in hydrogen production (Nada et al, 2005).

Instead of semiconductors, organic dyes can also be used as sensitizers to improve their optical properties. The commonly used dyes such as polypyridine complexes, phthalocyanine and metalloporphyrins are the transition metal complexes with low lying excited states. Mg(II), Fe(II), Ru(II), Zn(II) and Al(III) are the common metal centers for

the organic dyes and the ligands include aromatic rings or nitrogen heterocyclics with delocalized π-system (Meyer, 2005; Rehm et al, 1996).

2.9.4 Reduction of particle size

Reduction of particle size increases the surface area of nanoparticles. The smaller the particle size the higher the specific surface area for adsorption of contaminants and the higher the photo-catalytic efficiency since only the molecules that are in direct contact with the catalyst surface undergo degradation. Also the smaller the particle size the shorter the distance the charge carrier travels to the surface where the reaction occurs. It has been reported that the reduction in particle size of titanium dioxide nanoparticles from 29 nm to 17 nm decreased the band gap from 3.23 eV to 3.173 eV then increased from 3.173 to 3.289 eV as the particle size decreased from 17 to 3.8 nm (Lin et al, 2006). Size-control is achieved by varying the initial precursor type, concentration of the precursor, reaction temperature, intermediate injection of precursors and order of addition of water and ethanol.

Decreasing the particle size of the semiconductor increases the band gap and this is indicated by an absorption shift to shorter wavelengths (Hengleinn & Bunsenges, 1997). Besides the increase in surface area due to reduction in particle size, there is also a decrease in the band gap but only above a certain threshold. There is an optimal particle size of TiO_2 for different organic compounds for effective degradation. Generally the particle size should not be less than the Bohr radius because as the dimensions approach the Bohr radius, the effective band gap of the semiconductor increases with decrease in particle size due to quantum confinement effects (Buhro & Colvin, 2003). Therefore, for

optimal photo-catalytic efficiency there is a critical particle size below which the surface recombination of the electron and hole becomes dominant due to increased surface to volume ratio.

Some researchers have reported that TiO_2 normally undergoes an anatase-to-rutile phase transformation between 600-700 °C and a reduction in particle size and a large surface area have been proposed to favor this transformation (Hu et al, 2003). Such a transformation may be affected by factors such as preparation conditions, type of precursor used, presence of impurities and oxygen vacancies (Xia et al, 1999). Somorjai, 1981 suggested that photo-catalytic activity was lower in the rutile phase because the recombination of the electron-hole pairs produced by UV-light occurred more readily on the rutile phase surface than with the anatase phase where recombination was less. Also, small particles have a low light scattering capacity and yield a superior efficiency in photocatalysis (Lee et al, 2002).

2.9.5 Use of a nano-support

Using carbon nanofibres as catalyst support is a promising way to increase specific surface area. It helps to increase the quantum efficiency by retarding charge carrier recombination because of electron scavenging through graphene layers. Basically, the support increases the surface area of catalytic material, governs the useful lifetime of the catalyst, decreases sintering temperature and improves the chemical stability of the catalytic material (Haller, 2003). The support might also improve the activity of the catalyst by acting as a co-catalyst (Haller, 2003). The nanofibres minimize the chance of e–/h+ pair recombination by transporting the charges generated in the photocatalysis process (Hu et al, 2007).

Generally it is believed that a good catalyst support for a titanium dioxide photocatalyst should have the following attributes:

i. Good adsorption capability for the contaminants to be degraded
ii. Be transparent to UV radiation to allow penetration of light so that it reaches the photocatalyst.
iii. Offer a high specific surface area.
iv. Chemically inert
v. Favour strong chemical/physical bonding with TiO_2 particles without affecting their photocatalytic activity negatively i.e. should offer good adherence.
vi. Be in a physical state that allows or favours liquid-solid phase separation (Pozzo et al, 1997).

Several substrates have been proposed as supports for the degradation of organic pollutants in water.

2.10 TiO_2 nanoparticle supports

The use of TiO_2 photocatalyst as a powder has been experimentally proved and used for the degradation of most of organic compounds and removal of heavy metal ions (Vohra & Davis, 1997; Colon et al, 2001). However, there is a problem of filtration to remove and recycle the catalyst after use. To avoid this difficult and costly problem of filtration, many methods and different supports have been proposed and used to immobilize TiO_2. Possible supports for TiO_2 photocatalyst include glass, quartz, stainless steel (Fernandez et al, 1995: Brezova et al, 1995), zeolites (Torimoto et al, 1996), silicon carbide (Nishida et al, 2007), organic fibres and pumice stone (Rao et al, 2004). Silicon carbide is a useful

photocatalyst support for use in the liquid phase and has the advantage of high thermal stability, high mechanical strength, high electrical conductivity and can be easily molded into a filter (Nishida et al, 2007: Guerfi et al, 2005). Fernandez et al, 1995 investigated the effects of different supports on the photocatalytic activity of TiO_2 in the degradation of malic acid and they found out that the photocatalytic activity followed the order: TiO_2/quartz > TiO_2/steel ≈ TiO_2/glass. Silica gel is also another promising support since it has been widely used in the industry and it possesses good light transmission and adsorption of pollutants (Wang et al, 2006). Cheaper support materials are prefentially used for cost effectiveness in some cases.

2.10.1 Polymer/Carbon nanofibre supports

The main purpose of the photocatalyst support is to have an easy separation of the catalyst from the liquid medium and to avoid ultrafine particles filtration. Carbon fibres are high-strength materials that have been described as fibres containing at least 90 % carbon obtained by the controlled pyrolysis of suitable fibers. The diameters of typical carbon nanofibres are in the range from 100 nanometres to 1 micrometre (Chun et al, 1999). Such nanofibres have a wide range of applications due to their unique properties such as high mechanical strength, high specific surface area and high adsorption capacity. Nanofibres with specific surface properties are of interest in technical applications because these surface features affect adsorption, wettability, biocompatibility and electro-optical properties. The surfaces of polymer nanofibres can be modified and a technique for modification is chosen to produce specific chemical and physical properties. The immobilization of titanium dioxide onto polymer nanofibres was found to exhibit very interesting properties due to its unique optical and dielectric properties (Watanabe et al,

1999). Polymers have been proved to be useful in assembling nanoparticles because the stability of the semiconductor nanoparticles can be improved greatly by being assembled in the polymer material (Gao et al, 1994).

In this project polyacrylonitrile based carbon nanofibres were used as the photocatalyst support.

2.10.1.2 Carbon nanofibre precursors

PAN-based carbon fibres have been established to be stronger than most precursor based carbon fibres. Among the precursors that can be used to produce carbon fibres PAN has been the most preferred and most suitable compared to other precursors such as pitch, rayon and cellulosic precursor because of its properties which include:

i. A fast pyrolysis rate without changing its basic structure (Wiles, 2002).
ii. A high melting point and greater carbon yield (>50% of the original precursor mass (Bahl et al, 1974: Wangxi et al, 2003).
iii. It has a continuous carbon backbone and nitrile groups that can ideally be replaced for cyclization to occur producing a ladder.

Although pitch has high carbon content, processing and purifying it to the fibre form is very expensive and the resulting carbon fibres are extremely poor in strength compared to PAN. Table 2.1 shows the carbon content in percent of some of the precursors that can be used to produce carbon fibers.

Table 2.1: Carbon content of some precursors

Precursor	Carbon content %
PAN	68
Cellulosic precursor	45
Pitch	85

To produce fibers with desirable properties the molecular weight of the precursor should be about 100,000 g/mol and the heating rate used during stabilization should be low to control the exothermic reaction.

2.10.1.3 Properties of PAN

Polyacrylonitrile is a vinyl polymer and a derivative of the acrylate family of polymers. It is commonly known as acrylic fibre and is usually made from acrylonitrile by free radical polymerization. There are appreciable electrostatic forces between the dipoles of the adjacent nitrile groups on the polymer molecule and these results in a very high crystalline melting point of 317 $^{\circ}$C (Saunders, 1988). The PAN molecules form extended structures due to the high electronegativity of the nitrile group. The dipoles interact by electrostatic attraction as shown in Figure 2.11. The hydrogen bonding between the polymer chains allows strong fibres to be produced. It has a good chemical stability, good insulation properties, and resistance to aging at high strength.

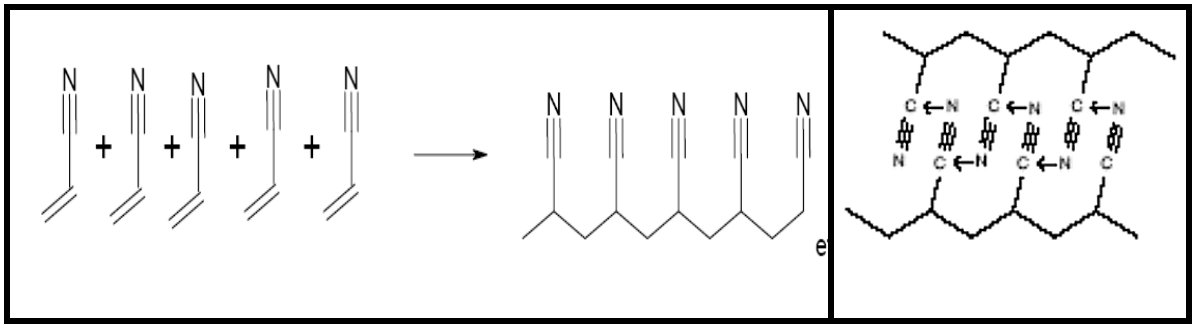

Figure 2.11: Schematic representation of polymerization of homo-PAN and nitrile dipoles.

Polyacrylonitrile has a density between 1.14-1.17g/cm^3. It is discoloured when heated to 160 $^{\circ}$C, softens when heated to 235 $^{\circ}$C and it undergoes structural changes when heated to high temperatures in the presence of oxygen. It is soluble in dimethylformamide, dimethylacetamide, thiocyanate and in aqueous solutions of inorganic salts (Saunders, 1998). The average molecular weight of commercial PAN is in the range 80 000-170 000 g/mol and the glass transition temperature (Tg) is 125 $^{\circ}$C..

PAN fibres characteristically possess low water absorption so they are considered as being hydrophobic in nature (Burkinshaw & Skelton, 1994). The adsorption of water is believed to occur by virtue of three forces of interaction such as dipole-dipole interactions with the highly polar cyano group, hydrogen bonding and various ion-dipole forces between ionic groups in the polymer and water molecules.

PAN can either be wet or dry spun but the wet spun fibre is preferred because it results in a large internal surface area of order 200-300 m^2g^{-1} whereas that of dry spun is less than 1 m^2g^{-1} (Craig et al, 1962).

2.11 Preparation of nanofibres

2.11.1 Electrospinning Process

Electrospinning is a process by which a high voltage is used to produce an interconnected membrane like a web of small fibres with a diameter in the range of 50-1000 nm. It has been recognized as an effective way of producing polymer fibres from polymer solutions and molten states. It can be used with different polymers to produce nanoscale fibrous membranes. Polymers that have been electrospun include rayon in acetone/alcohol solvent (Formhals US Patent, 1934), acrylicresin in DMF (Baugarten, 1971), melted polyester (Kim & Lee, 2000), polyurethane in DMF (Demir et al, 2002) and PAN in DMF (Ali, 2002). The organic solvents that are commonly used to dissolve the polymer for electrospinning are highly volatile. Their presence in the polymer solution and subsequent vaporization during electrospinning is believed to facilitate the formation of nanofibres (Mauck, 2005).

The electrospinning process has been found to be a unique and cost effective way of fabricating high surface area fibres (Doshi & Reneker, 1995). Basically there are three components in the electrospinning process set up and these are:

i. A high voltage power supplier
ii. A capillary tube with a pipette or a needle of small diameter and
iii. A metal collecting screen

The positive electrode is immersed into polymer solution and the negative electrode is connected to the collector. The distance between the collector and the tip of the pipette is

normally varied between 5 and 20 cm. The basic electrospinning setup is shown in Figure 2.12.

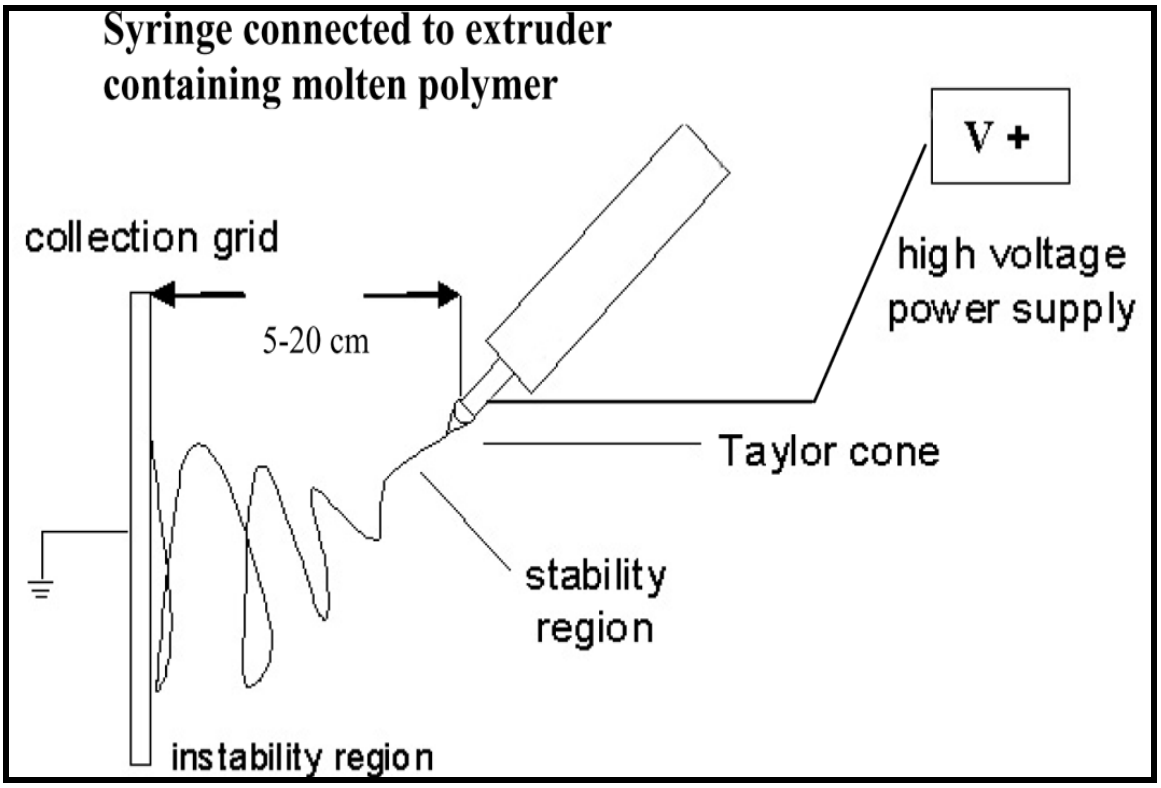

Figure 2.12: Schematic of electrospinning process (Lyons & Ko, 2005).

When a high voltage is applied to a liquid droplet, the liquid becomes charged, and electrostatic repulsion counteracts the surface tension. As the intensity of the electric field is increased the liquid at the tip of the capillary tube elongates to form a conical shape known as the Taylor cone. A critical point is attained with further increase in the electric field at which the repulsive electrostatic force overcomes the surface tension and a stream of liquid erupts from the Taylor cone forming a jet (Taylor, 1969). This solution jet undergoes an instability and elongation process, which allows the jet to become long and thin. The jet may or may not split and if it splits into multiple jets it results in

different fibre diameters. If there is no splitting involved, then one of the most significant parameters influencing the fibre diameters will be the solution viscosity.

There are various parameters affecting the diameter and length of the resulting nanofibres and these include:

i. Solution properties such as conductivity, surface tension, elasticity and viscosity. The higher the viscosity (higher polymer concentration) the larger the diameter of the resulting fibres (Doshi & Reneker, 1995) and the lower the viscosity then the shorter and finer the fibres will be (US Patent, 1996).
ii. Molecular weight and architecture (branched/linear) of the polymer
iii. Flow rate and voltage. A high applied voltage ejects more fluid in a jet, resulting in large fibre diameters (Demir et al, 2002).
iv. Hydrostatic pressure in the capillary tube
v. The distance between the capillary tip and the collecting device/screen. When the distance is short the fibres are short in length and tend to stick to the collecting device as well as to each other due to incomplete solvent evaporation
vi. Ambient parameters (temperature, humidity and velocity of air in the chamber)

These parameters can be varied to allow control of fibre diameter, structure and mat morphology. Some of the advantages of electrospinning include:

i. The fibres can be easily spun from a few milligrams of the polymer compared to the commercial wet-spinning process which requires about 5 kg.
ii. Production of narrow diameter size fibres.

iii. Nanofibres can be stretched up to a draw ratio of 300 000 within a distance of about 20 cm in less than a second.

Due to these advantages, there has been a lot of work done on electrospinning. Since the late 1998 the number of publications on electrospinning and related research is growing exponentially every year as shown in Figure 2.13 (De Vrieze & Clerck, 2008).

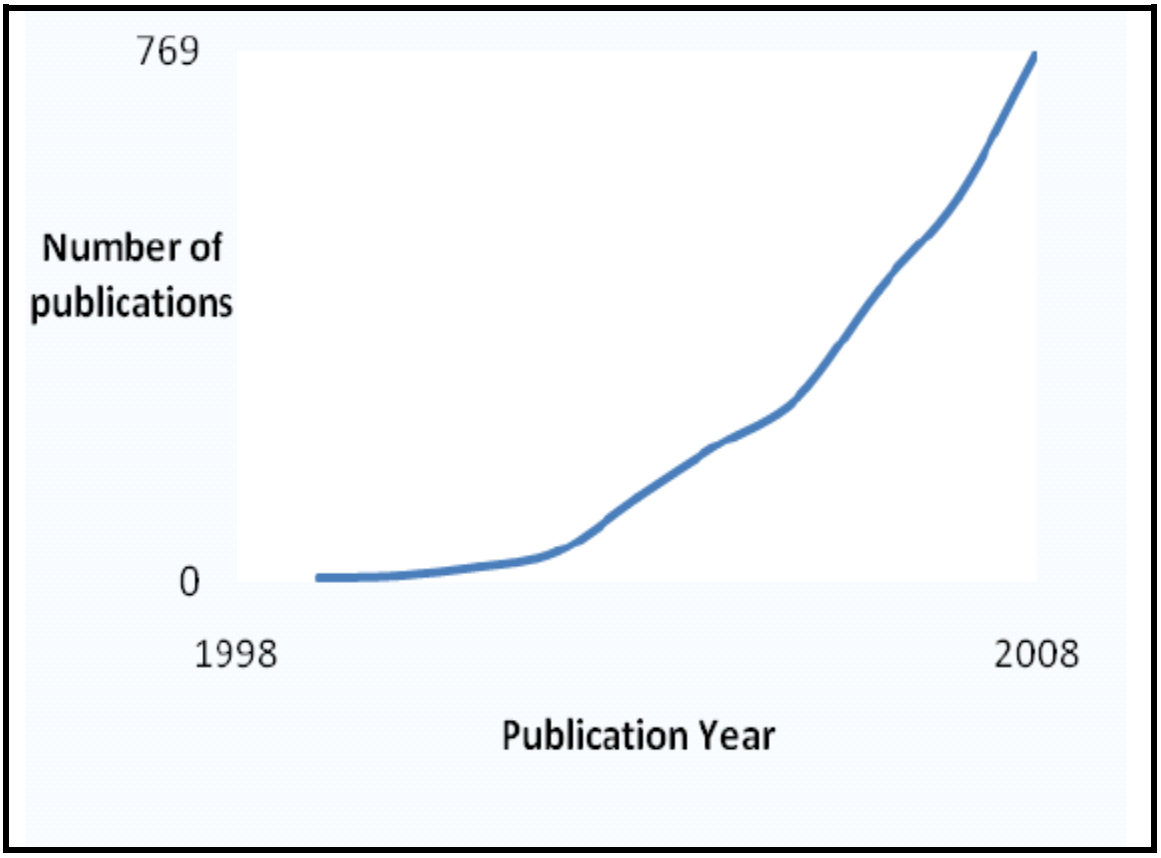

Figure 2.13: A graphical representation of the number of publications on electrospinning between 1998 and 2008 (De Vrieze & De Clerk, 2008).

It is also possible to produce electrospun mats consisting of two polymeric components which are immiscible or miscible. This is achieved by electrospinning the two polymer

solutions at the same time in a side by side fashion allowing the formation of a bicomponent electrospun mat that have properties from each of the polymeric components. The electrospinning set-up for simultaneous electrospinning two polymer solutions is shown in Figure 2.14.

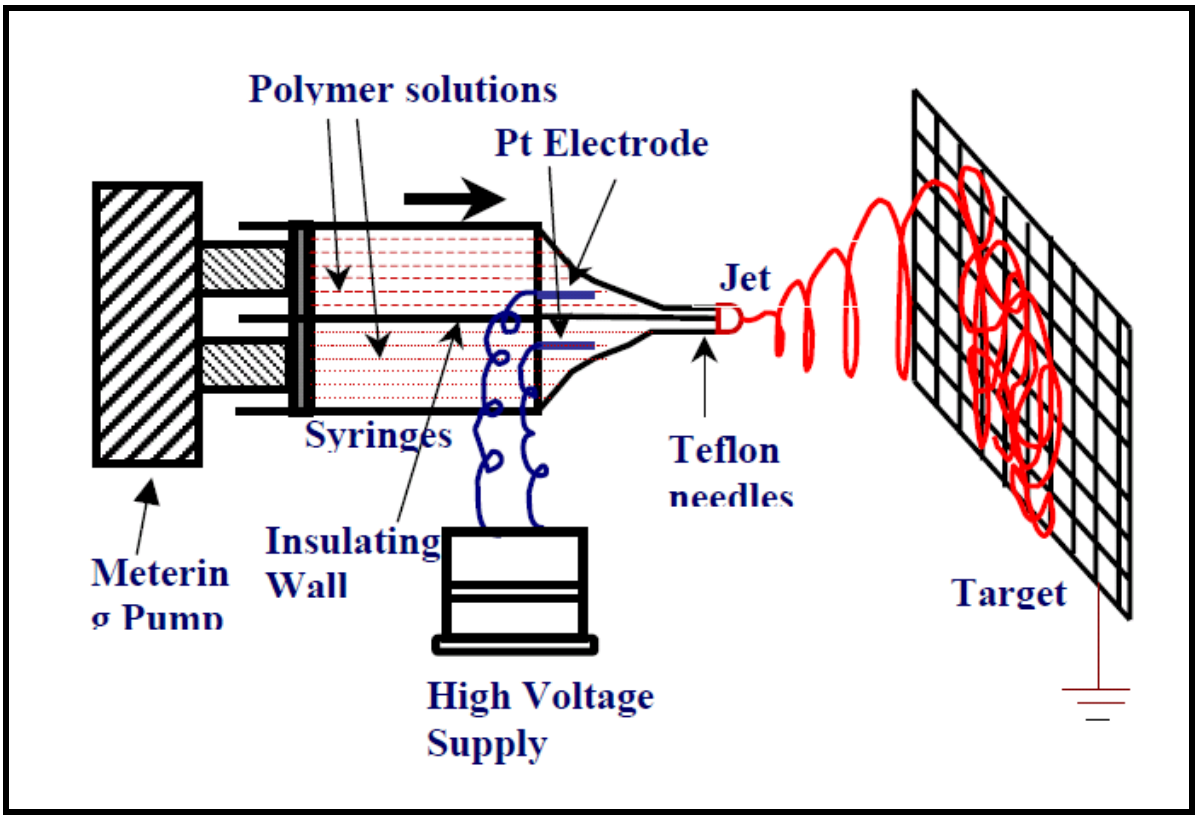

Figure 2.14: A bicomponent electrospinning set-up (Schreuder-Gibson et al, 2004)

The advantages of bicomponent fibres are the improved properties since one polymer could contribute to the mechanical strength while the other could enhance the wettability of the resulting mats for example.

2.12 Preparation of carbon nanofibre supports

2.12.1 Stabilization of PAN fibres

In processing acrylic fibres to produce carbon fibres, an oxidative stabilization treatment is essential. The stabilization is usually done in the temperature range of 200 °C-300 °C in an oxygen containing atmosphere to make the fibres thermally stable so that they can withstand high temperatures during carbonization. There are various chemical and structural changes that take place during stabilization of PAN and these are affected by stabilization conditions such as time, temperature and environment (Bhat, 1990; Gupta & Harrison, 1996). The physical and chemical changes are caused by various exothermic chemical reactions such as oxidation, dehydrogenation, cyclization, cross-linking and aromatization which results in the formation of an infusible stable conjugated ladder structure. The other changes that occur during thermal stabilization are: the loss of thermoplasticity, chain scission and chain breakdown (Saufi & Ismail, 2002). During the course of stabilization there are some colour changes that occur from white to yellow then finally dark brown or black. Of all the reactions that occur, the cyclization reaction is the most important in the stabilization of PAN. It is an exothermic reaction of the nitrile groups with adjacent groups resulting in the formation of the ladder structure (Fitzer & Muller, 1975). This reaction is essential to hold fiber molecules together and increases the stiffness (Grassie et al, 1971).

Stabilization of PAN can be done in an inert environment but an air environment is always preferred because a polymer back-bone with oxygen groups in the ladder structure gives good stability to withstand high carbonization temperature (Rangarajan et al, 2002). Fitzer and Muller, 1975 reported that the activation energy was greater in air than in

nitrogen indicating that oxygen is an initiator in the formation of the active center for cyclization.

Density is believed to be a very good indicator of the extent of stabilization. The density and the oxygen content of the stabilized PAN fibres decreases with an increase in the heating rate (Hou et al, 2008). It has been reported that, for successful carbonization, the stabilized fibres should reach a precursor dependent critical density (Jain et al, 1987).

2.12.2 Carbonization of PAN fibres

Carbonization can be described as a heating process up to 800 °C-3000 °C to bring about an aromatic growth and polymerization typically to 95 % carbon content (Ko, 1991). The carbonization is generally carried out in an inert environment and in most cases a nitrogen rich environment is used because of increase in both tensile strength and modulus (Lee et al, 1997). Carbonization in a hydrogen chloride vapour environment could enhance the fibre yield and help to decrease the expected hydrogen cyanide amount by eliminating nitrogen as ammonia (Rahaman et al, 2007).

Carbonization can be done at different temperatures depending on the required properties of the resulting carbon fibres. The fibres can be divided into three categories and these are:

i. Type I, which are high temperature treated carbon fibres. The final temperature should be above 2000 °C. The resulting fibres have a high modulus.
ii. Type II, medium temperature treated fibres where the final temperature is around 1500 °C. These fibres have a high strength.

iii. Type III are low heat treated carbon fibres. The final heat treatment temperature is less than 1000 °C.

In this study low temperature carbonization which is normally done from 400 °C to 900 °C was used.

It is recommended that the heating rate be controlled as it affects the properties of the resulting fibres. When the carbonization process is done at a heating rate lower than 5 °C/min intramolecular cyclization is the main reaction and above 5 °C/min intermolecular cross-linking reaction becomes the main reaction, so to obtain high-quality carbon fibres, the heating rate should not be higher than 5 °C/min (Hou et al, 2008).

Different gases are released and the amounts released depend on the temperature. The main scission products released from PAN precursor between 400 °C and 1000 °C are hydrogen cyanide, ammonia and nitrogen. Water, carbon monoxide, carbon dioxide, hydrogen and methane are also released in small quantities (Lewin & Preston, 1983). The evolution of different volatiles creates pores within the fibres and as the pyrolysis temperature increases more by-products are released enhancing pore formation (Steel, 2000). The average pore diameter increases with increase in temperature up to 800 °C due to release of the carbon atoms as carbon monoxides (David, 2001). The pores will shrink and collapse due to progressive annealing at very high temperatures (Suda & Haraya, 1997).

The amount of the gases released at different temperatures during stabilization and carbonization are shown graphically in Figure 2.15.

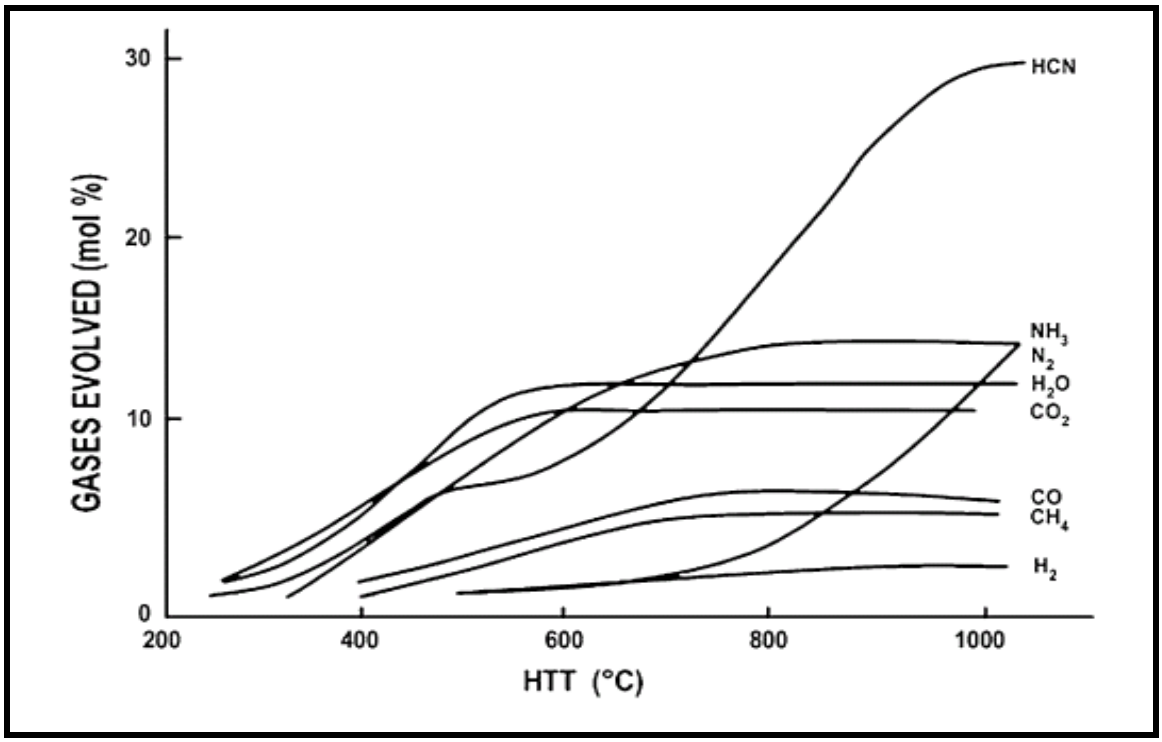

Figure 2.15: Release of non-carbon atoms during carbonization of PAN (Monacha, et al, 1980).

2.13 Stabilization and carbonization mechanism of PAN

The mechanism of carbon fibre formation from PAN is a complex process and a lot of reaction schemes have been proposed. Saufi and Ismail, (2002) proposed a mechanism of the stabilization and carbonization chemistry of PAN (homopolymer) as shown in Figure 2.16. It is clear from Figure 2.16 that in some chains cyclization occurs first followed by dehydrogenation whereas in other straight chains dehydrogenation occurs first before cyclization. Generally these processes occur simultaneously.

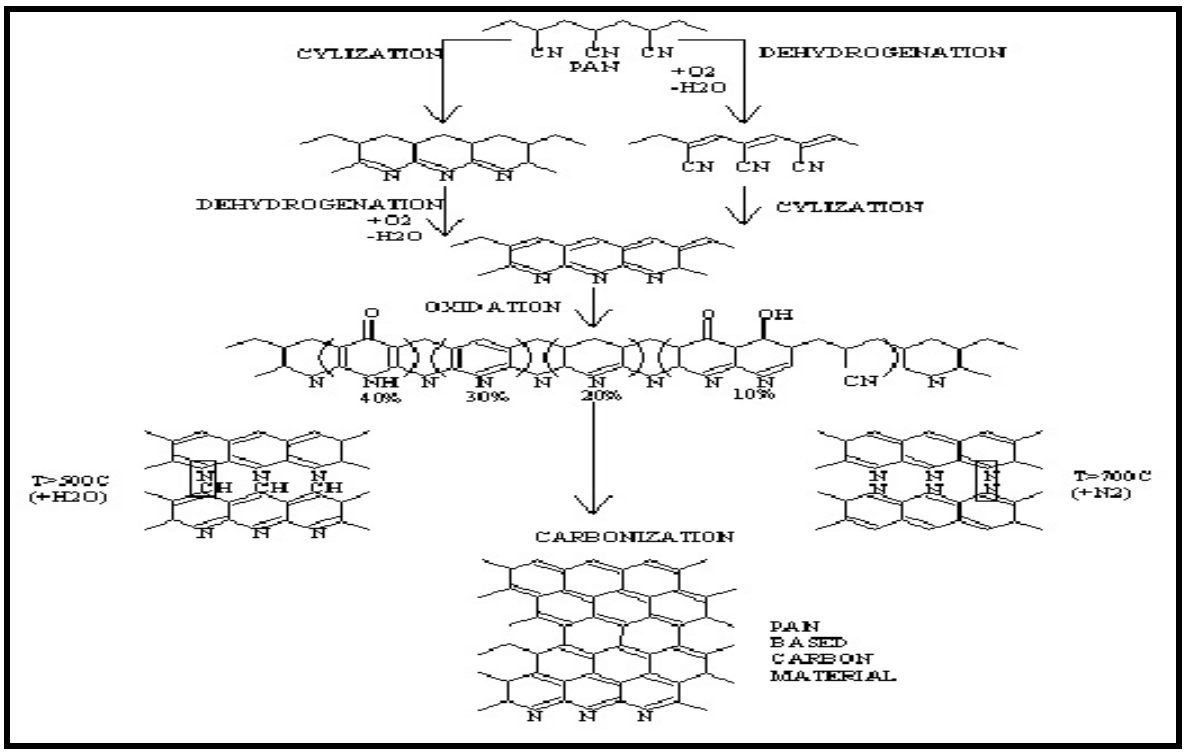

Figure 2.16: Proposed mechanism of reactions taking place during stabilization of the homopolymer PAN (Saufi & Ismail, 2002).

If the PAN is a copolymer the proposed stabilization mechanism is shown in Figure 2.17.

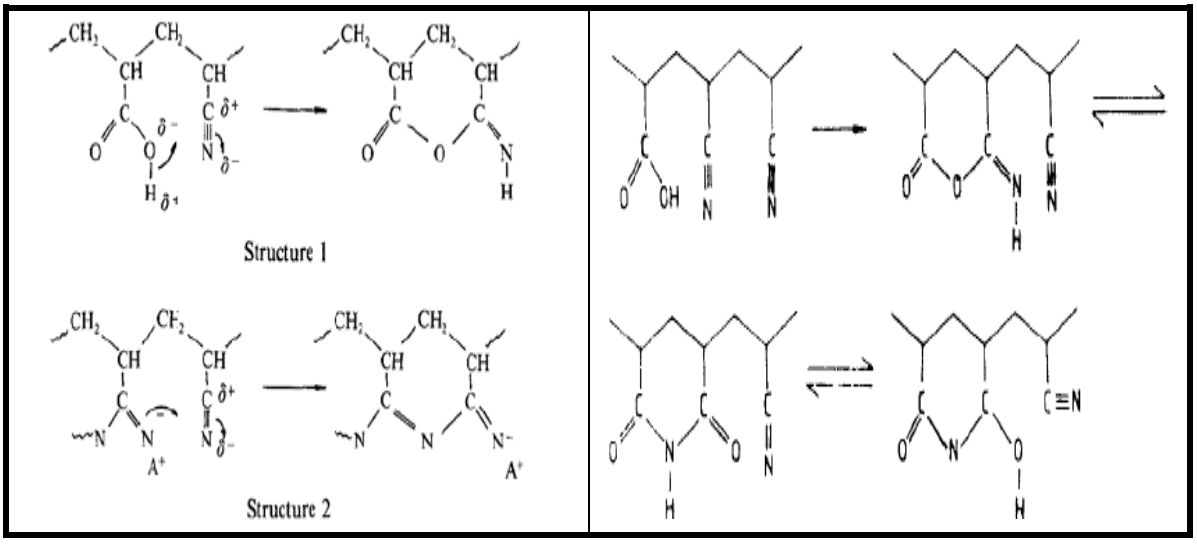

Figure 2.17: Mechanism of stabilization of PAN (copolymer) (Tsai & Lin, 1990)

The extent of stabilization and carbonization can be determined by FT-IR and DSC. The PAN molecule consists of functional groups such as methyl and nitrile and during oxidative stabilization new structures are formed such as ketones, aldehydes and carboxylic acids (Saufi & Ismail, 2002). When carbonization is done, these transition compounds are expected to be released as volatiles but a 100 % conversion is generally impossible due to other compounds in the polymer. Table 2.2 shows a summary of the FT-IR results for PAN pyrolized at different temperatures.

Table 2.2: FTIR frequencies of fuctional groups of PAN pyrolysed at different temperatures (Saufi & Ismail, 2002).

Pyrolysis Temperature	Functional Group	Frequency /cm^{-1}
500 °C	C≡N	2216.42
	C-N	1265.90
	C=C	1595.42
600 °C	C≡N	2224.05
	C=N	1649.36
	C-N	1265.77
	C=C	1539.65
	N-H	3445.29
	C=O (Aldehydes)	1739.53
	C=O (Ketones)	1701.79
700 °C	C=N	1653.23
	C-N	1021.84
	C=C	1540.69
	N-H	3442.13
	C=O (Ketones	1701.01
	C-H	2924.63
800 °C	C=N	1649.58
	C-N	1021.39
	C=C	1541.42
	N-H	3442.97
	C-H	2923.64

2.14 Characterization techniques

This section gives a brief summary of the analytical and characterization techniques used in this study.

2.14.1 Fourier transform infrared spectroscopy

This is a non destructive technique capable of identifying particular functional groups that are present in organic compounds. It is very useful for analyzing organic and certain inorganic substances. In order to analyze a sample, a beam of infrared light is passed through the sample and radiation absorption is measured as a function of frequency. A spectrum is produced which shows wavelengths at which the sample absorbs the IR and this allows identification of functional groups, compounds, chemical bonding and molecular structures.

Clear spectra are normally obtained from pure samples with a few infrared active bonds and complex structures give complex spectra due to more absorption bands. In this study this technique was used to detect the chemical structural changes of stabilized and carbonized PAN nano-fibre supports containing titanium dioxide using a Perkin Elmer FT-IR instrument.

2.14.2 Transmission electron microscopy

This is a technique that uses an electron beam to image a sample. It is used to identify and characterize nanometer sized embedded particles. The information that we get from this technique includes size, shape and arrangement of the particles, agglomeration, effects of annealing and catalyst support coverage/distribution.

2.14.3 Scanning electron microscopy

It is one of the analytical tools that are most widely used in industry due to the detailed images it provides. It gives quick identification of elements present, particle characterization, surface morphology, porosity, rapid and high resolution imaging and material homogeneity (Photometrics website).

2.14.4 Differential scanning calorimetry

DSC is a thermo analytical technique in which the difference in the amount of heat required to increase the temperature of the sample and reference (empty pan) is measured as a function of temperature. Differential scanning calorimeters are able to measure the amount of heat released or absorbed during transitions by observing the difference in heat flow between the sample and the reference. The temperature of both the sample and reference are maintained at nearly the same values throughout the experiment (Karlson, 2010) and it is required that the reference sample/pan should have a well-defined heat capacity over the range of temperature to be scanned.

The principle underlying DSC is that, when a sample undergoes a transformation such as phase transition, more or less heat flows to it than the reference so that both are maintained at the same temperature. It is commonly used for understanding the stability of both organic and inorganic compounds

The properties measured include crystallization, phase changes, glass transitions, oxidative stability and heat capacity (PhotoMetrics website).

2.14.5 Thermogravimetric analysis

Thermogravimetric analysis measures changes in weight of a material as a function of temperature under a controlled environment. The analysis is done by increasing the temperature of the sample in a furnace as its weight is measured on an analytical balance. Mass loss is observed if there is combustion, loss of a volatile component and finally decomposition of the material. The applications of TGA include determining filler and plasticizer content of polymers, carbon content, residual solvent content, oxidative stability, decomposition temperature and moisture content of organic and inorganic materials.

TGA analysis relies upon a high degree of precision in three measurements which are weight, temperature and temperature change. Some applications of TGA include oxidation, decomposition of organic matter, determination of ignition temperature of explosives and kinetics and activation energy measurements.

2.14.6 X-ray photoelectron spectroscopy

XPS is a quantitative surface chemical analysis technique that is based on photoelectric effect. It is a technique used due to its high sensitivity, ease of operation, ease of interpretation of results and the wealth of useful information it gives. It is used for determining what elements and the quantity of those elements that are present within 10 nm of sample surface, empirical formula of pure samples, the binding energy of electronic states, chemical state and electronic state of the elements that exist within a material (Wikipedia, 2010). It also gives information about the types of bonding that occur within various compounds (Chaudhuri et al, 2006). An XPS spectrum is a plot of

the number of electrons versus the binding energy of the detected electrons. Elements produce characteristic peaks at characteristic binding energy values that identify each element that is on the surface or in the material being analyzed. The number of electrons detected in each characteristic peak is proportional to the amount of element present in sample irradiated.

In order for XPS to be successful the following requirements must be met:

i. Experiments should be carried out under UHV (~10^{-9} torr or lower) pressure to reduce the amount of noise in the spectrum and minimize extra peaks due to contaminants (Shafer, 2001; Chaudhuri et al, 1999).
ii. Should have high resolution in order to detect differences between surface and bulk contributions that are statistically significant (Shafer, 2001).
iii. Photons should be monochromated to avoid "ghost" peaks that can make it impossible to recognize surface and bulk contributions.

In this study X-ray photoemission spectroscopy was used to analyze the chemical composition of doped TiO_2 to determine the extent of incorporation of carbon and nitrogen dopants into the TiO_2 framework.

2.14.7 Diffuse reflectance spectroscopy

Diffuse reflectance spectroscopy is a good sampling tool for powdered or crystalline materials. The samples to be run are generally ground and mixed with a non-absorbing matrix such as potassium bromide prior to sampling. It is used to estimate the band-gap energy (also referred as band gap) and the absorption (Murphy, 2007). The diffuse

reflectance of a powder depends on particle size and refractive index of the substance (Lindberg & Snyder, 1972).

In this study this technique was used to estimate the band gap (Eg) using the empirical formula: $Eg = 1239/\lambda_{edge}$ where λ_{edge} is the wavelength of the optical absorption edge (Weng et al, 2005). The calculated band gap values indicate the effects of doping that is, the shift of band gap to lower values indicates that doping was successful.

2.14.8 Ultraviolet-visible spectroscopy

The instrument used is called a spectrophotometer and it consists of three components: the source, the dispersive system and a detector. The commonly used detector is a photomultiplier tube which consists of photo-emissive cathode (which emits electrons when struck by photons of radiation), several dynodes (which emit several electrons for each electron striking them) and an anode.

It operates by passing a beam of light through a sample and then measures the intensity of light that reaches the detector. Different molecules absorb radiation of different wavelengths and an absorption spectrum will show absorption bands corresponding to structural groups in the molecule. It is used in the quantitative determination of the concentrations of absorbing species such as transition metal solutions and conjugated organic compounds. In organic molecules, absorption of ultraviolet and visible radiation is restricted to certain functional groups called chromophores that have valence electrons of low excitation energy.

In this study the technique was used to determine the changes in concentration of methyl orange during the evaluation of the photocatalytic activity of the TiO_2/PAN composite fibres.

2.14.9 X-ray diffraction

This is a powerful technique for characterizing crystalline materials. It gives information on the degree of structural order (crystallinity), structures, average grain size, phases, preferred crystal orientations (texture) and crystal defects. The x-ray diffraction peaks are produced by constructive interference of monochromatic beam of x-rays scattered at specific angles from lattice planes in the sample. This occurs when a mineral contains lattice planes with d-spacings appropriate to diffract x-rays at that value of theta. The strengths of this technique are that it is nondestructive, there is minimal or no sample preparation and ambient conditions are used for analysis and quantitative measurement of phase contents and texture orientation.

Generally, if the samples are thin (<1000 nm) the number of crystal lattices that contribute to X-ray diffraction become less resulting in a reduction of the X-ray diffraction intensity and a rise of the background (Munekwa, 1998). To increase the X-ray diffraction intensities, the thin film diffractometer is designed in such a way that the incident X-rays are fixed at small 2θ values of 3 to 5 so as to lengthen the optical path along which the X-ray beam passes through the thin film.

2.14.10 Raman spectroscopy

Raman spectroscopy is a spectroscopic technique based on inelastic scattering or Raman scattering of monochromatic light, usually from a laser source in the visible, near

ultraviolet or near infrared range. The Raman Effect takes place when light strikes a molecule and interacts with the electron cloud and bonds of that molecule. For a spontaneous Raman Effect, a molecule is excited from the ground state to a virtual energy state, and relaxes to a vibrational energy state that generates Stokes Raman scattering and if the molecule was already in a vibrational energy state, the Raman scattering is called anti-stoke Raman scattering (Gardiner, 1989).

Raman spectroscopy is sensitive to changes in the atomic structure of carbons and has proved to be helpful in understanding the vibration properties and microstructure of graphitic crystals and various disordered graphite materials. It has been demonstrated to be a valuable technique for the characterization of carbon fibres (Tuinstra & Koenig, 1970). The intensities and frequencies of the Raman bands observed have been found to depend on surface treatment and the method used. When used for carbon nanofibres characterization, the Raman scattering manifest D and G peaks centered around 1360 cm^{-1} and 1580 cm^{-1} respectively both being attributed to sp^2 bonded species (Dresselhaus et al, 1999). The intensity of the peak around 1360 cm^{-1} increases as the crystallite size decreases in graphite samples, and the ratio of the intensities of the 1360 cm^{-1} to that of 1580 cm^{-1} has been utilized as an indirect measure of the crystallite size in graphite fibres (Chaudhuri et al, 2006).

The Raman spectra obtained for various fibres gives information mainly about the surface layers because the incident light penetrates only up to 50 nm. This means that the type of bonding between the matrix and the surface region of the fibre can be determined (Chaudhuri et al, 2006). When used for nanoparticles characterization, the Raman bands

shift to a higher frequency if there is a decrease in particle size. Broadening also indicates a decrease in particle diameter.

In this study this technique was used to determine if carbonization had been achieved.

References

Addamo, M.; Augugliaro, V.; Paola, A. D.; Lopez, E. G.; Loddo, V.; Marci, G.; Palmisano, L. Colloids and Surfaces A: *Physicochemical and Engineering Aspects* **2005**, *265*, 23–31.

Anasys: *http://www.anasys.co.uk/library/dsc2.htm* **2010**.

Ali, A. *Carbon Nanotube Reinforced Carbon Nano Composite Fibrils by Electrospinning, in Materials Engineering* **2002**.

Arana, J.; Nieto, J. L. M.; Melian, J. A. H.; Rodriguez, J. M. D.; Diaz, O. G.; Perna, J. P.; Arroyo, R.; Rodriquez, R.; Salinas, P. *Journal of Non-Crystalline Solids* **1993**, *163*, 90.

Attar, A. S.; Ghamsari., M. S.; Hajiesmaeilbaigi, F.; Mirdamadi, S.; Katagiri, K.; Baetzold, R. C. *Journal of the American Chemical Society* **1981**, *103*, 6116.

Bahl, O. P & Manocha, L. M. Characterization of oxidized PAN fibers. *Carbon 12* **1974**, *4*, 417-23.

Barringer, E. A.; Bowen, H. K. *Journal of the American Ceramic Soc*iety **1982**, *65*, 199.

Baumgarten, P. K. *Journal of Colloid Interface Science* **1971** *36***,** , 71.

Bergasa, C. A & Mendez, J. *Chemosphere* **2004**, *55*, 893.

Blossey, R. *Nature Materials* **2003**, *2*, 301–306.

Burkinshaw, S. M & Skelton, H. *Dyes and Pigments* **1994**, *26*, 15.

Boccuzzi, F.; Chiorino, A.; Haruta. M. *Journal of Physical Chem*stry **1996**, *100*, 3625.

Braun, J. H.; Baidins, A.; Marganski, R. E. *Progress in Organic Coatings* **1992**, *20*, 105.

Brezova, V.; Blazkova, A.; Brez, M.; Kottas, P.; Ceppan, M. *Collection of Czechoslovak Chemical Communications* **1995**, *60*,788.

Brinker, C & Scherer, G. *Physics and Chemistry of Sol-Gel Science Processing*, *Academic Press, Toronto* **1990**.

Brus, L. *Journal of Physical Chemistry* **1986**, *90*, 2555.

Burda, C.; Lou, Y. B.; Chen, X. B.; Samia, A. C. S.; Stout, J.; Gole, J. L. *Nano Letters* **2003**, *3*, 1049.

Chai, L.; Yu, Y.; Zhang, G.; Peng, B.; Wei, S. *Nonferrous Metals Society of China* **2007**, *17*, 176-180.

Chaudhuri, S. N.; Chaudhuri R. A.; Benner R. E.; Penugonda M S. *Composite Structures* **2006**, *76*, 375–387.

Chen, Y. F.; Lee, C. Y.; Yang, M. Y.; Chiu, H. T. *Journal of Crystal Growth* **2003**, *247*, 3-4.

Choi, W.; Termin, A.; Hoffmann, M. R. *Journal of physical chemistry* **1994**, *28*, 13669.

Choi, Y.; Umebayashi, T.; Yoshikawa, M. *Journal of Materials Science* **2004**, *39*, 1837.

Citrin, P. H.; Wertheim, G. K.; Baer, Y. *Physical Review B* **1983**, 27, 3161.

Colon, G.; Hidalgo, M. C.; Navio, J. A. *Journal of Photochemistry. Photobiology. A: Che*m **2001**, *138*, 78-85.

Corradi, A. B.; Bondioli, F.; Focher, B.; Ferrari, A. M.; Grippo, C.; Mariani, E.; Villa, C. *Journal of the American Ceramic Society* **2005**, *88*, 2639.

Craig, J. P.; Knudsen, J. P.; Holland, V F. *Textile Research Journal* **1962**, *32*, 465.

Daneshvar, N.; Niaei, A.; Akbari, S.; Aber, S.; Kazemian, N. *Global NEST Journal* **2007**, *9*, 132-136.

Demir, M. M.; Yilgor, I.; Yilgor, E.; Erman, B. *Electrospinning of polyurethane fibres*. *Polymer* **2002**, *43*, 3302.

De Vrieze, S & De Clerck, K. *80 years of electrospinning. Department of Textiles, Ghent University, Technologiepark 907, 9052 Gent, Belgium*

Ding, X.; Qi, Z.; He, Y. *Journal of Materials Science Letters* **1995**, *14*, 21.

Domenech, J & Prieto, A. *Journal of Physical Chemistry* **1986**, 90 , 1123-1126.

Dresselhaus, M. S.; Dresselhaus, G.; Pimenta, M. A.; Eklund, P. C. *Analytical Application of Raman Spectroscopy, Chapter 9, Blackwell, London, UK* **1999**.

Feng, L. *A thesis presented to the University of Waterloo for a Master of Applied Science in Chemical Engineering, Ontario, Canada* **2006**.

Feng, X. J.; Zhai, J.; Jiang, L. *Angewandte Chemie International Edition* **2005**, *44*, 5115.

Fernandez, A.; Lassaletta, G.; Jimenez, V. M.; Justo, A.; Gonzalez-Elipe, A. R.; Herrmann, J. M.; Tahiri, H.; Ait-Ichou, Y. *Applied catalysis B: Environmental* **1995**, *7*, 49-63.

Fitzer, E. & Muller, D. J. *Carbon* **1975**, *13*, 63-9.

Fitzmaurice, D.; Frei, H.; Rabani, J. *Journal of Physical Chemistry* **1995**, *99*, 9176.

Formhals, A. *Process and apparatus for preparing artificial threads. USA* **1934**.

Frank, S. N & Bard, A. J. *Journal of Physical Chemistry* **1977**, *81*, 1484.

Fujishima, A.; Hashimoto, K.; Watanabe, T. *TiO_2 Photocatalysis: Fundamentals and Applications. Best Knowledge Center (BKC), Tokyo, Japan* **1999.**

Gablenz, S.; Voltske, D.; Abicht, H. P.; Neumann-Zoralek J. *Journal of Materials Science Letters* **1998**, *17*, 537–539.

Gao, M. Y.; Yang, Y.; Yang, B.; Bian, F. L.; Shen, J. C. *Journal of the Chemical Society, Chemical Communications* **1994**, 2779.

Gardiner, D. J. *Practical Raman spectroscopy. Springer-Verlag* **1989**.

Grassie, N & McGuchan, R. *European Polymer Journal* **1971**, 7, 1357-71.

Gratzel, M. *Progress in Photovoltaics*, **2000**, *8*, 171.

Gratzel, M. *Nature* **2001**, *414*, 338.

Gressel, M. E, Chaumont, D, Stuerga, D. *Journal of Colloid and Interface Science* **2005**, *285*, 674.

Grunze, M. *Chemical Physical Letters* **1978**, *58*, 409.

Guerfi, K.; Lagerge S.; Meriziani, M. J.; Nedellec, Y. *Thermochemica. Acta* **2005**, *434*, 140.

Henglein, A & Bunsenges, B. *Journal of Physical Chemistry* **1997**, *101*, 1562.

Henrich, V. E.; Dresselhaus, D.; Zeiger, H. J. *Physical Review Letters* **1976**, *36*, 1335–1339.

Hewitt, J. *Cosmetics and Toiletries* **1999**, *114*, 59.

Hoffmann, M. R.; Martin, S. T.; Choi, W.; Bahnemann, D. W. *Chemical Reviews* **1995**, *95*, 69.

Hoyer, P & Koenenkamp, R. *Applied Physics Letters* **1995**, *66*, 349.

Hu, G.; Meng, X.; Feng, X.; Ding, Y.; Zhang, S.; Yang, M. *Journal of Materials Science*, **2007**, *42*, 7162–7170.

Hu, Y.; Tsai, H. L.; Huang, C. L. *Materials Science & Engineering A* **2003**, 344, 209-214.

Huanga, D. G.; Liao, S. J.; Liu, J. M.; Danga, Z.; Petrik, L. *Journal Photochemistry and Photobiology A: Chem* **2006**, *184*, 282–288.

Irie, H.; Watanabe, Y.; Hashimoto, K. *Journal of Physical Chemistry B* **2003**, *107*, 5483.

Ishigaki, T & Li, J. G. *Science and Technology of Advanved Materials* **2007**, *8*, 617–623.

Ishigaki. *Thin Solid Films* **2004**, *457* 186–191.

Jahromi, H. S.; Taghdisian, H., Afshar. S.; Tasharrofi, S. *Surface & Coatings Technology* **2009**, *203*, 1991–1996.

Jang, H. D & Jeong, J. *Aerosol Science and Technology* **1995**, *23*, 553-560.

Kabra, K., Chaudhary, R., and Sawhney, R. L. *Industrial & Engineering Chemistry Research* **2004**, *43*, 7683–7696.

Karlson, J. *Master of Science Thesis, Chalmers University of Technology* **2010**.

Khan, S. U. M.; Al-Shahry, M.; Ingler, W. B. *Junior Science* **2002**, *297*, 2243

Kim, C. S.; Moon, B. K.; Park, J. H.; Choi, B.C.; Seo, H. J. *Journal of Crystal Growth* **2003**, *257*, 309.

Kim, C.S.; Nakaso, K.; Xia, B.; Okuyama, K.; Shimada, M *Aerosol Science and Technology* **2005**, *39*, 104-112.

Kim, S. J & Lee, D. S. *Thermal properties of electrospun polyesters*. *Polymer* **2000**, 32 616.

Kim, S. B & Hong, S. C. *Applied Catalysis B: Environmental* **2002**, *35*, 305.

Kositzi, M.; Poulios, I.; Malato, S.; Caceres, J.; Campos, A. *Water Research* **2004**, *38*, 1147–1154.

Koumoto, K. *Journal of Physics* D*: Applied Physics* **2008**, *41*, 155318.

Kuhn, K. P.; Chaberny, I. F.; Masholder, K.; Stickler, M.; Benz, V. W.; Sonntag, H. G.; Erdinger, L. *Chemosphere* **2003**, *53*, 71– 77.

Leaustic, A.; Babonneau., F.; Livage, J. *Chemstry of Materials* **1989**, *1240*

Lee, K. R.; Kim, S. J.; Song, J. S.; Lee, J. H.; Chung, Y. J.; Park S. *Journal of American Ceramic society* **2002**, *85*, 341-45.

Lee, J. K.; Shim, H. J.; Lim, J. C.; Choi, G. J.; Kim, Y. D.; Min, B. G. *Carbon 35* **1997**, *6*, 837-43.

Li, W. J.; Mauck, R. L.; Tuan, R. S. *Journal of Biomedical Nanotechnology* **2005**, *1*, 259-275.

Lin, H.; Huang, C. P.; Li, W.; Ni, C.; Shah., I. S.; Tseng, Y. H, . *Applied Catalysis B: Environmental* **2006**, *68*, 1–11

Lindberg, J. D & Snyder, D. G. *American Mineralogist* **1972**, *57*, 485-493

Lindgren, T.; Mwabora, J. M.; Avendano, E.; Jonsson J.; Hoel, A.; Granqvist, C. G.; Lindquist, S.E. *Journal of Physical Chemistry B* **2003**, *107*, 5709.

Linsebigler, A. L.; Lu, G.; Yates, J. T. *Chemical Reviews* **1995**, *95*, 735-758.

Livage, J.; Henry, M.; Sanchez, C. *Progress in Solid State Chemistry* **1988**, *18*, 259–341

Liu, S.; Lim, M.; Fabris, R.; Chow, C.; Chiang, K.; Drikas, M.; Amal, R. *Chemosphere* **2008**, *72*, 263-271.

Luo, M.; Bowden, D.; Brimblecombe, P. *Water Air Soil Pollution* **2009**, *198*, 233-241.

Lyons J & Ko, F. *Polymer News* **2005**, *30*, 1–9

Maness, P. C.; Smolinski, S.; Blake, D. M.; Huang, Z.; Wolfrum, E. J.; Jacoby, W. A. *Applied and Environmental Microbiology* **1999**, *65*, 4094– 4098.

Maness, P. C.; Smolinski, S.; Jacoby, W. A. *Applied and Environmental Microbiology* **1990**, *65*, 4094.

Martin, C.; Rives, V.; Sanchez-Escribano, V. *Surface Science* **1991**, *825*, 251-252.

Matijevic, E.; Budnik, M.; Meites, L. *Journal of Colloid Interface Science* **1997**, *6*, 302.

Manocha, L. M & Bahl, O. P. *Fiber Science and Technology* **1980,** *13*, 199-212.

Meyer, G. J. *Inorganic Chemistry* **2005**, *44*, 6852.

Moon, Y. T.; Park, H. K.; Kim, D. K.; Kim, C. H. *Journal of the American Ceramic Society* **1995**, *78*, 2690-94.

Munekwa, S. *The Rigaku Journal* **1998**, *5*, 2.

Murphy, A. B. *Solar Energy Materials & Solar Cells* **2007**, *91*, 1326–1337

Nada, A. A.; Barakat, M. H.; Hamed, H. A.; Veziroglu, T. N. *International Journal of Hydrogen Energy* **2005**, *30*, 687.

Nie, X.; Zhuo, S.; Maeng, G.; Sohlberg, K. *International Journal of Photoenergy* **2009** 10.1155/2009/294042.

Nishida, Y.; Kawasaki, S.; Yuan, S.; Mori, K.; Narisawa, M.; Matsumura, Y.; Ohmich, T.; Katayama, I.; Yamashita, H. *Journal of Materials Online* **2009**, *3*.

Ko, T. H. *Journal of Applied Polymer Science* **1991**, *43*, 589-600.

Ohsaki, Y.; Masaki, N.; Kitamura, T.; Wada, Y.; Okamoto, T.; Sekino, T.; Niihara, K.; Yanagida, S. *Physical Chemistry Chemical Physics* **2005**, *7*, 4157

Oskam, G.; Nellore, A.; Penn, R. L.; Searson, P.C. *Journal of Physical Chemistry B* **2003**, *107*, 1734.

Parala, H.; Devi, A.; Bhakta, R.; Fischer, R. A. *Journal of Materials Chemistry* **2002**, *12*, 1625.

Park, J. H.; Kim, S.; Bard, A. J. *Nano Letters* **2006**, *6*, 24.

Peral, J.; Domenech, X.; Ollis, D. F. *Journal of Chemical Technology & Biotechnology* **1997**, *70*, 117–140.

PhotoMetrics, Inc. 15801: *http://www.photometrics.net/DSC.html* **2010.**

Preuss, H. P. *Pigments in Paint* **1974**.

Pozzo, R. L.; Baltanas, M. A.; Cassano, A. C. *Catalysis Today*, **1997**, *39*, 219-231.

Prieto, O.; Fermoso, J.; Nueez, Y.; Del Valle, J. L.; Irusta, R. *Solar Energy* **2005**, *79*, 376–383.

Rademann, K.; Even, U.; Hensel, F. *Physical Review Letters* **1992**, *69*, 3208

Rangarajan, P.; Bhanu, V. A.; Godshall, D.; Wikels, G. L.; McGrath, J. E.; Baird, D. G. *Polymer* **2002,** *43*, 2699-709.

Rao, C. N. R.; Santra, A. K.; Prins, M. W. J. *Angewandte Chemie International Edition in English* **1992**, *31*, 1062.

Rao, K. V. S.; Subrahmanyam ,M.; Boule, P. *Applied Catalysis B: Environmental* **2004**, *49*, 239–249.

Rasheed, R. A. *Water treatment by heterogenous photocatalysis an overview. Presentation at the 4th Saline Water Conversion Corporation (SWCC) Acquired Experience Symposium held in Jeddah, Saudi Arabia* **2005**.

Rehm, J. M.; McLendon, G. L.; Nagasawa, Y.; Yoshihara, K.; Moser, J.; Gratzel, M. *Journal Physical Chemistry* **1996**, *100*, 9577.

Rocquefelte, X.; Goubin, F.; Koo, H. J.; Whangbo, M. H.; Jobic, S. *Inorganic Chemistry* **2004**, 43, 2246–2251.

Saquib, M & Muneer, M. M. *Dyes and Pigments* **2003**, *56*, 37.

Satterfield, C. N. *Heterogeneous Catalysis in Industrial Practice* **1991**.

Sato, N.; Matsuda, M.; Yoshinaga, M.; Nakamura, T.; Sato, S.; Muramatsu, A. *Topics in Catalysis* **2009**, *11*, 1592-1597

Saufi, S. M. & Ismail, A. F. *Songklanakarin Journal of Science and Technology* **2002**, *24*, 843-854

Seifried, S.; Winterer, M.; Hahn, H. *Chemical Vapour Deposition* **2000**, *6*, 239.

Schreuder-Gibson H. L & Gibson P. *US Army research development and engineering command. http://www.inda.org/subscrip/inj04_4/p39-45-gibson.pdf* **2010**.

Sclafani, A.; Mozzanega, M. N.; Pichat, P. *Journal of Photochemstry and Photobiology. A: Chem* **1991**, *59*, 181.

Shafer, M. *Surface Chemical Shifts by XPS* **2001**.

Somorjai, G. A. *Chemistry in Two Dimensions: Surface* **1981**, 551.

Sugimoto, T.; Okada, K.; Itoh, H. *Journal of Colloid & Interface Science*, **1997**, *193*, 140.

Sun, J.; Wang, J.; Sun, R.; Sun, S.; Qiao, L. *Journal of Molecular Catalysis. A*, **2006**, *260*, 241.

Torimoto, T.; Ito, S.; Kuwabata, S.; Yoneyama, H. *Environmental Science & Technology* **1996**, *30*, 1275-1281.

Tuinstra, F & Koenig, J. L. *Journal of Composite Materials* **1970**, *4*, 492.

Tryk, D. A.; Fujishima, A.; Honda, K. *Electrochimica Acta* **2000**, *45*, 2363.

Tsai, J.S & Lin, C.H. *Journal of materials science letters* **1990**, *9*, 869-871.

United States Patent 7524793. *Titanium dioxide photocatalyst containing carbon and method for its production* **2009**.

Valden, M.; Lai, X.; Goodman, D. W. *Science* **1998**, *281*, 1647.

Varghese, O. K.; Gong, D. W.; Paulose, M.; Grimes, C.A.; Dickey, E.C. *Journal of Materials Research* **2003**, *18*, 156.

Vorkapic, D & Matsoukas, D. *Journal of the American Ceramic Society* **1998**, *81*, 2815–20.

Vogel, R.; Hoyer, P.; Weller, H. *Journal of Physical Chemistry* **1994**, *98*, 3183.

Vohra, M. S & Davis, A. P. *Journal of Colloid Interface Science* **1997**, *197*, 59-67.

Wang, X.; Li, J.; Kamiyama, H.; Katada, M.; Ohashi, N.; Moriyoshi, Y.; Ishigaki, T. *Journal of the American Chemical Society* **2005**, *127*, 10982.

Wang, Y. M.; Liu, S. W.; Xiu, Z.; Jiao, X. B.; Cui, X. P. *Materials Letters* **2006**, *60*, 974-978.

Wangxi, Z.; Jie, L.; Gang, W. *Carbon* **2003**, *41*, 2805-12.

Weng, W.; Ma, M.; Du, P.; Zhao, G.; Shen, G.; Wang, J.; Han, G. *Surface & Coatings Technology* **2005**, *198*, 340– 344.

Wikipedia: *http://en.wikipedia.org/wiki/X-ray_photoelectron_spectroscopy* **2010.**

Wiles, K. B. *M.Sc thesis, Faculty of the Virginia Polytechnic Institute and State University: Blacksburg, Virginia* **2002**.

Wu, J. M.; Zhang, T. W.; Zeng, Y. W.; Hayakawa, S.; Tsuru, K.; Osakav. A. *Langmuir* **2005**, *21*, 6995.

Wu, J. J & Yu, C. C. Journal of Physical Chemistry B **2004**, *108*, 3377.

Wu, X.; Jiang, Q. Z.; Ma, Z. F.; Fu, M., Shangguan, W.F. *Solid State Communications* **2005**, *136*, 513.

Yu, J. C.; Yu, J. G.; Ho, W.; Zhang, L. Z. *Chem Communications* **2001**, 1942.

Xiaobo, C. *Chinese Journal of Catalysis* **2009,** 30, 839–851.

Xia, B.; Huang, H.; Xie, Y. *Materials Science & Engineering.* B57, **1999,** 150-154.

XingGang, H.; MeiDong, H.; XiaoLing, W.; AnDong, L. *Science in China Series G: Physics, Mechanics & Astronomy* **2009.**

Xu, Y.; Zheng, W.; Liu, W. *Journal of photochenistry and photobiology* **1999**, *122*, 57-60.

Yu, F. H & Wang, S.M. *Journal of Non-Crystalline Solids* **2000**, *261*, 260-267.

Zhang, H & Banfield, J. F. *Journal of Physical Chemistry, B,* **2000**, *104*, 3481.

CHAPTER 3

3. Preliminary studies on titanium dioxide support materials

3.1 Introduction

One of the objectives of this study was to produce strong supports for the TiO_2 nanoparticles so that they do not wear out easily and could be used repeatedly. Thus, before studies, the major parameter (heating rate) that affects the properties of the resulting fibres was determined so that the best possible carbon fibres using the available materials and equipment could be obtained.

The major requirement for production of carbon nanofibres with desirable mechanical properties from PAN nanofibres was that the PAN nanofibres became completely stabilized (Farsani et al, 2007). Cyclization reactions are extremely exothermic (Paiva et al, 2003) and they occur mainly in the temperature range 220–235 $^{\circ}$C (Qin, 2009). The heat evolved during stabilization is not good for high performance carbon fibres so it should be minimized (Ouyang et al, 2008). Different sources reported different rates and criteria for stabilization and carbonization. Therefore it was very important to be careful when choosing these parameters. In this study, before stabilization and carbonization, DSC analysis of the blank PAN was done at different heating rates to determine the effect of heating rate on the amount of heat released. On the other hand DSC was also used to determine the purity of the PAN. In this chapter, the preparation of electrospun PAN nanofibres and thermal analysis of the supplied PAN powder and stabilized fibres are

described. In Section 3.3 the materials used and the results are briefly discussed in Section 3.4.

In view of the above background, the objectives of these preliminary studies were to (i) determine the purity of PAN powder and authenticity; (ii) establish suitable conditions for complete stabilization and carbonization of electrospun nanofibres.

3.2 Experimental

3.2.1 Materials and methods

The purity of the supplied homopolymer PAN was unknown so it was necessary to determine it.

3.2.2 DSC analysis of PAN powder

The analysis was done on a Perkin-Elmer DSC 7 differential scanning calorimeter equipped with Pyris Software and coupled to a Perkin-Elmer TAC 7/PC instrument controller. An aluminium pan with 10 mg of PAN powder was placed in the sample chamber and an empty aluminium pan was placed in the reference chamber, and scanned from 25 °C to 500 °C at 5 °C/min. The analysis was repeated using heating rates of 15 °C/min and 20 °C/min. The temperature range used accommodated all the expected changes of pure PAN such as Tg and cyclization. A plot of the heat flow against sample temperature resulted in a thermogram on which the onset temperature of cyclization of PAN was shown.

3.2.3 Preparation of nanofibres

A 10 % (w/w) PAN solution was prepared by dissolving 2g of PAN in 18.98 ml of DMF. The PAN solution was stirred for 2 hours to make sure all the PAN dissolved to make a homogenous solution.

3.2.3.1 Electrospinning experimental set-up

The electrospinning apparatus consisted of a syringe needle, a high voltage power supply that is capable of generating voltages up to 50 kV and an aluminum foil for collecting the nanofibres. The photograph of the electrospinning set-up used in this study is shown in Figure 3.1.

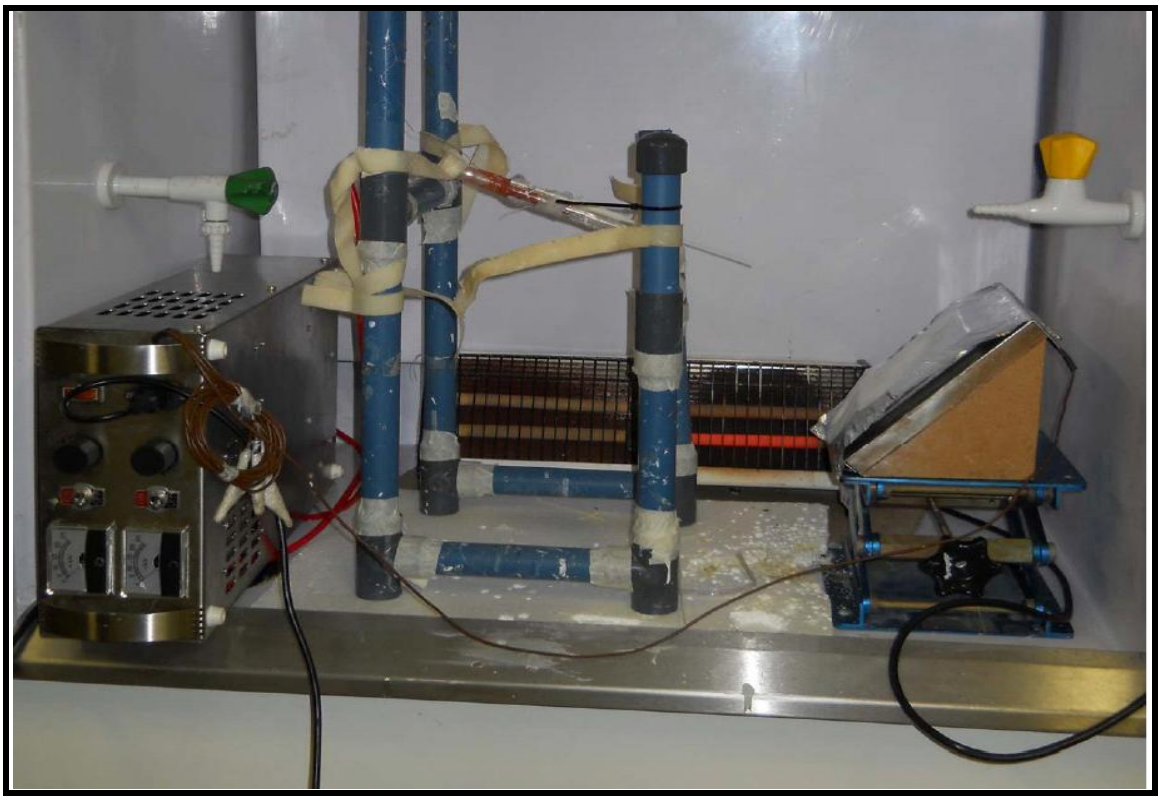

Figure 3.1: Photograph of the electrospinning set-up used in this study.

Using a syringe, the PAN solution was placed in a glass pipette with a diameter of 0.5 mm inclined at 45° to minimize dripping of the PAN solution. The distance from the tip of the glass syringe and the collector was fixed at 20 cm and the voltage used was 20 kV. A copper wire electrode used was inserted into the pipette until it was 4 cm from the end. The nanofibres to be stabilized were collected on an aluminium foil and those to be carbonized were collected on steel plates. The temperature in the fume hood was maintained between 30 °C and 35 °C by means of a heater to make sure that all the solvent evaporated to prevent the fibers from being re-dissolved

3.2.4 Stabilization of PAN nanofibres

A lot of stabilization conditions are reported in the literature (Sedghi et al, 2008; Farsani et al, 2007; Klata et al, 2005). Farsani et al, 2007 studied thermal characteristics of PAN and they managed to stabilize the polymer by heating in four stages which are: 25 °C to 205 °C for 60 minutes, 205 °C to 215 °C for 30 minutes, 215 °C to 230 °C for 30 minutes then finally from 230 °C to 260 °C for 30 minutes. Each stage was held for an hour. In this study the stabilization was done in a programmable furnace supplied by MET-UED, South Africa. The electrospun nanofibers were put at the centre of the furnace and then heated at a rate of 1 °C /min up to 280 °C. The temperature was maintained at 280 °C for 2 hours in an oxygen environment. This temperature was chosen based on DSC thermal analysis.

3.2.5 Characterization

3.2.5.1 Fourier transform infrared (FT-IR) spectroscopy

It was important to verify if the PAN nanofibres were completely stabilized and to check the extent of carbonization. The sample for analysis was prepared using potassium

bromide. A small amount (~0.001 g) of dried nanofibres was mixed with potassium bromide (~0.01 g) and ground in a pestle and mortar. The mixture was then pressed into pellets by means of a hydraulic pressing tool and an IR spectrum was obtained.

3.3 Results and discussion

3.3.1 DSC curves of PAN at different heating rates

As the heating rate was increased the exothermic peaks due to cyclization shifted and were seen to occur at higher temperatures. The exothermic peaks were centered at 295.78 °C, 281.78 °C and 270.75 °C for the heating rate of 20 °C, 15 °C and 5 °C respectively as shown in Figure 3.2.

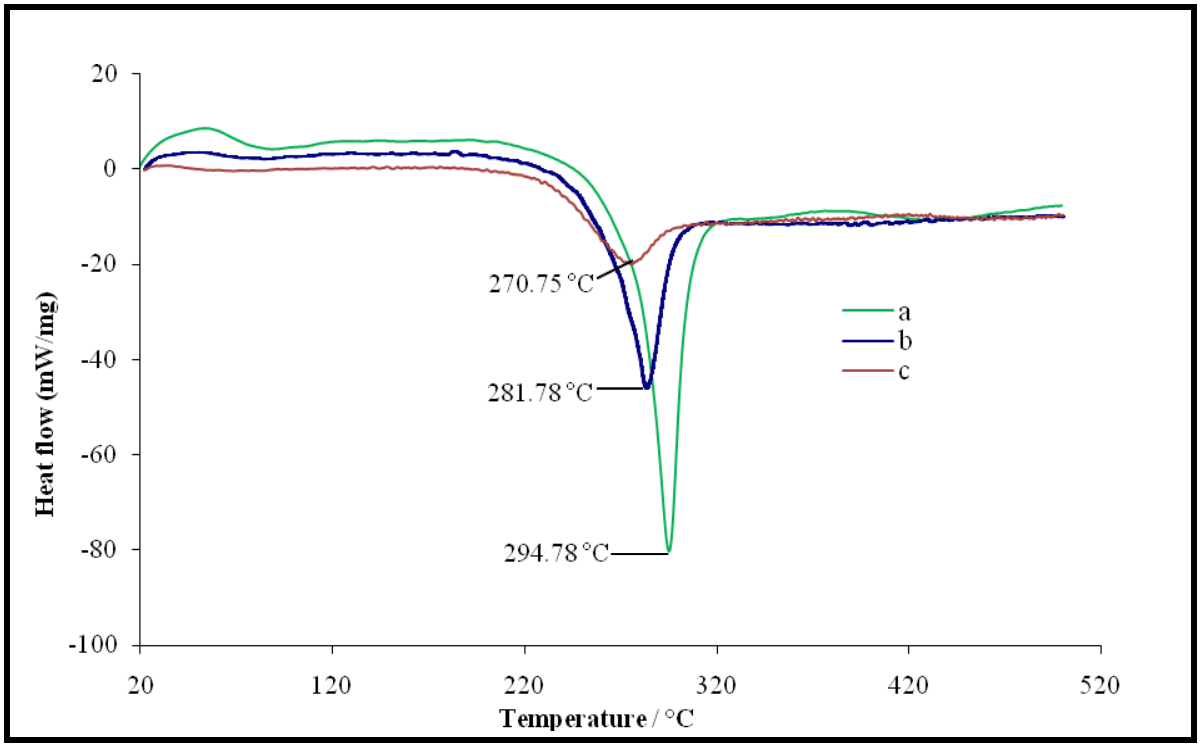

Figure 3.2: DSC curves of PAN at different heating rates: (a) 20 °C per minute (b) 15 °C per minute and (c) 5 °C per minute.

It can be seen from the DSC thermograms that the higher the heating rate the more heat was produced as shown by the size of the exothermic peaks. This was because the cyclization reactions were enhanced at high heating rates resulting in a great release of heat over a short period of time (Ouyang et al, 2008). For the homopolymer PAN, cyclization reactions followed a free radical mechanism thus the peak must have been due to both free radical cyclization reactions and other exothermic reactions such as oxidative reactions (Bajaj et al, 2001).

The endothermic peak around 50 °C was due to adsorbed moisture and it was more pronounced at high heating rates and it is negligible at low heating rates. Since only one exothermic peak was observed in the DSC thermogram it indicated that the PAN was a homopolymer and that it was pure.

3.3.2 Stabilization

3.3.2.1 Analysis of extent of cyclization using DSC

DSC measurement was used to check if the chosen heating rate and the holding times brought about complete stabilization. Since heat is only produced during cyclization to form a ladder structure, a DSC thermogram of the stabilized PAN fibres should show no exothermic peak. The DSC curves of the stabilized and the control are shown in Figure 3.3.

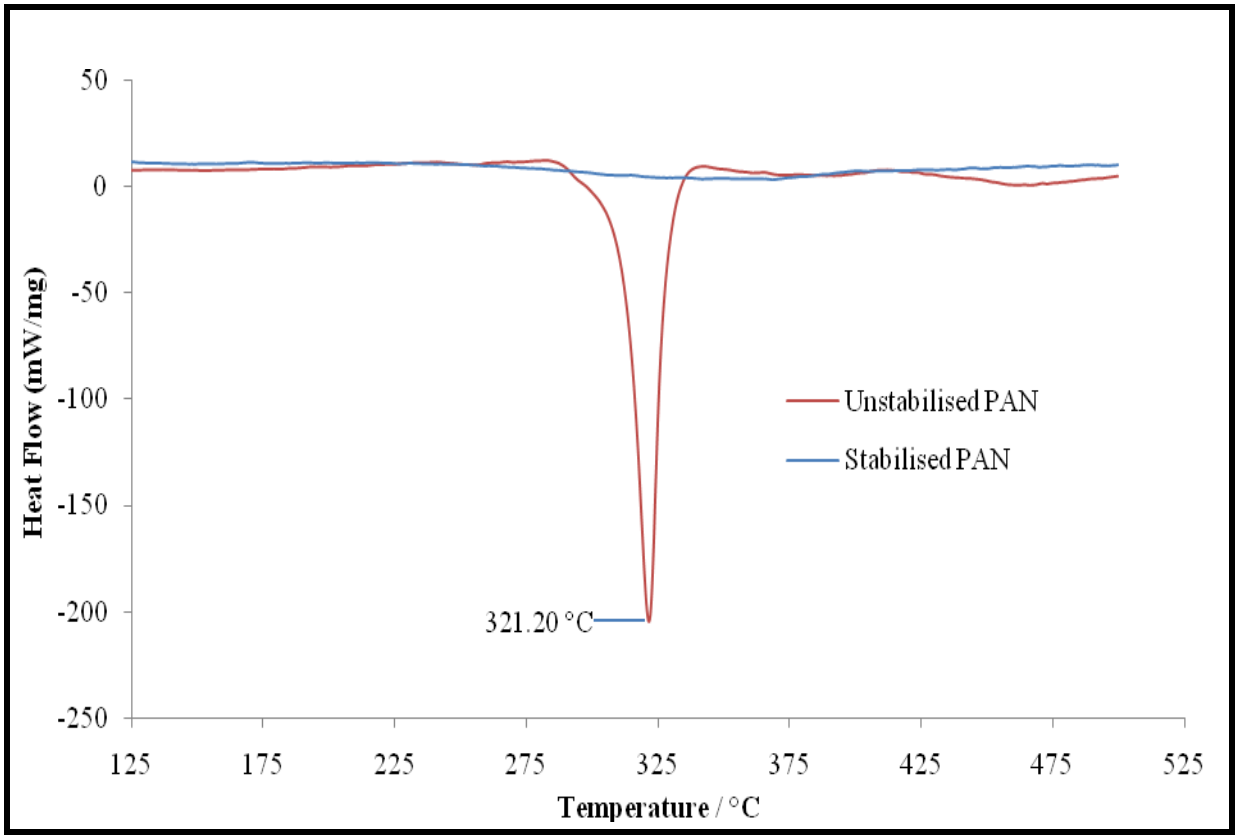

Figure 3.3: DSC curves of the stabilized and unstabilized PAN.

It was clear that there was a heat release peak for the unstabilised PAN nanofibres at 321.2 °C. This may have been due to crosslinking and cyclization of PAN. Cyclisation reactions are extremely exothermic (Paiva et al, 2003) and they occur mainly in the temperature range 220–235 °C (Qin, 2009). The stabilized PAN did not show an exothemic peak indicating that cyclization was basically complete and a heat resistant ladder structure had been formed. Therefore in this work cyclization was basically complete at 280 °C.

3.3.2.2 Analysis of extent of cyclization using FT-IR

It was also important to further confirm the stabilization of the PAN nanofibres by FT-IR. The spectra of the unstabilized PAN showed many peaks compared to the spectra of the

stabilized PAN. The proposed structure of the stabilized PAN is shown (insert in the spectra) in Figure 3.4. From this structure it can be seen that most of the hydrogen had been lost and only few remained.

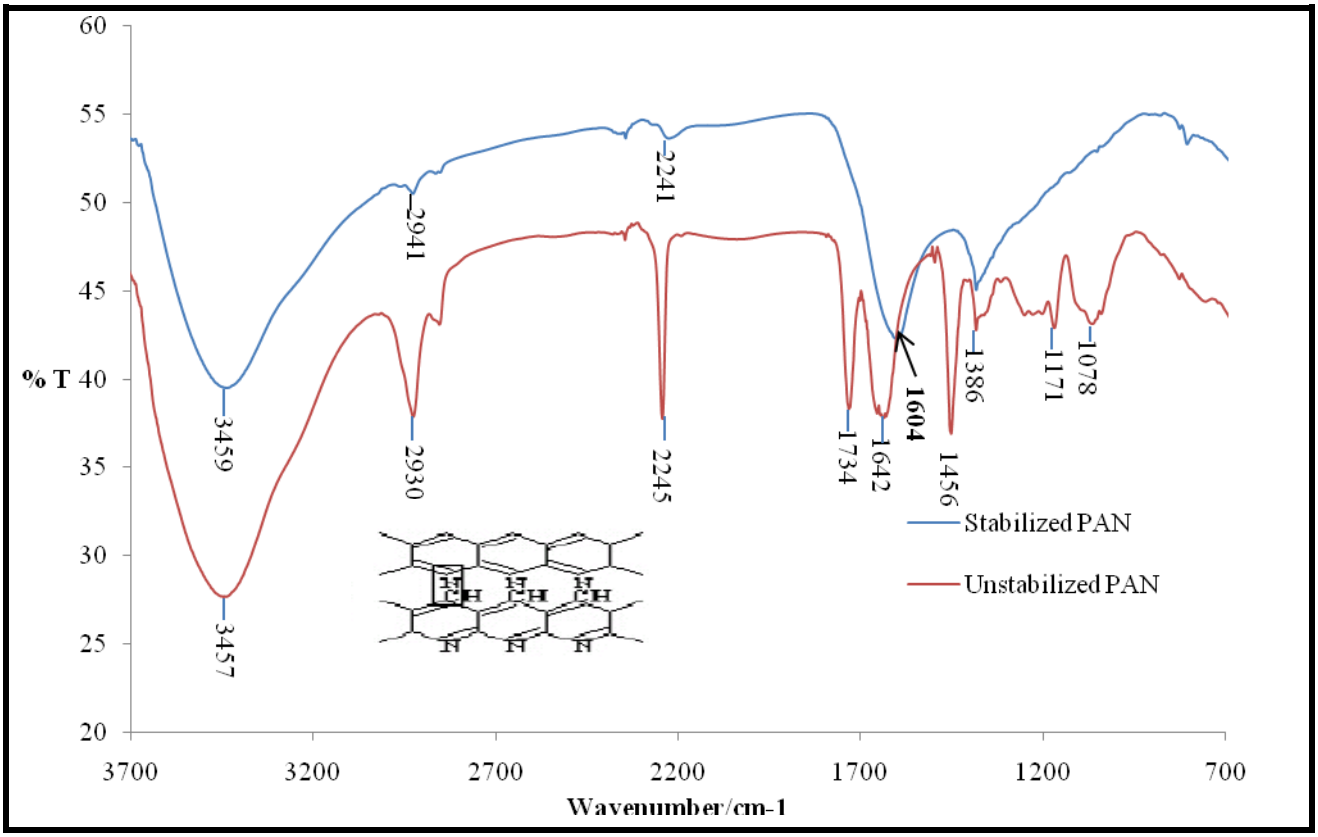

Figure 3.4: FT-IR spectra of stabilized and unstabilized PAN nanofibres.

FTIR spectra clearly showed that the band at 2245 cm^{-1} assigned to –C≡N stretching decreased considerably compared to the same peak in the spectrum of the unstabilised PAN. A new peak appeared in the spectrum at 1604 cm^{-1}, indicating that –C = C– (aromatic) had been formed during the stabilization process which showed that cyclization, dehydrogenation reaction had occurred during thermal/oxidative stabilization and an aromatic heat-resistant structure had been formed. This absorption peak around

1600 cm^{-1} could also be due to –C = N– band. The peak around 3457 cm^{-1} is due to the OH group. The peaks at 1171 cm^{-1} medium and 1734 cm^{-1} were very sharp due to C=O of the residual DMF and these peaks are absent in the spectrum of the stabilized PAN.

3.3.3 Carbonization

With the available furnace and equipment the best carbon fibres that could be prepared were those carbonized up to a maximum temperature of 600 °C. To determine whether carbon nanofibres had been obtained, Raman spectroscopy and FT-IR were used to analyze the samples. Micro-Raman spectrum was acquired with a microscope attachment Jobin-Yvon T64000 Raman triple spectrometer operated in single spectrograph mode with a 600 lines/nm grating. The 514.5 nm line of an argon laser was used as the excitation source. Power on the sample was ~1.2 mW to minimize heating and a 20 x objective was used to collect the backscattered light. A liquid nitrogen-cooled CCD detector and LabSpec v.4.18 software was used to record the spectra.

The Raman spectrum of the carbon fibres is shown in Figure 3.5. The spectrum shows two intense peaks at 1362.6 cm^{-1} and 1568.936 cm^{-1} indicating that the carbonization process was achieved. The peak centered at 1362.6 cm^{-1} is called the D peak and the one at 1568.936 cm^{-1} is called the G peak and both are attributed to sp^2 bonded species (Dresselhaus et al, 1999).

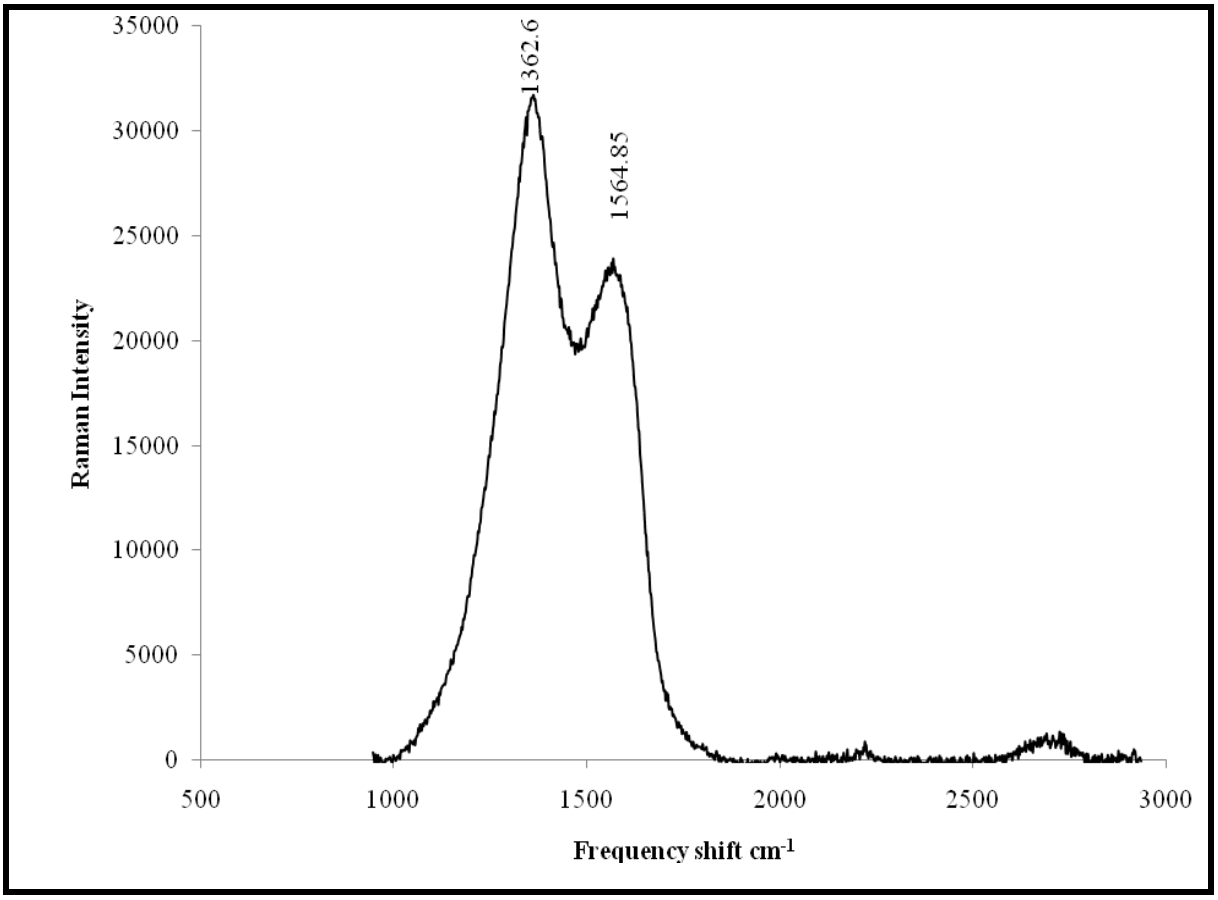

Figure 3.5: A Raman spectrum of carbonized nanofibres using 514.5nm laser excitation

To further confirm carbonization of the fibres, FT-IR was used. The FT-IR spectra of the carbonized and stabilized PAN are shown in Figure 3.6. From the spectra it can be seen that the peak due to asymmetric and symmetric in CH, CH_2, and CH_3 groups around 2928 cm^{-1} and 2861 cm^{-1} (Deng, 2003), had completely disappeared showing that almost all the hydrogen had been lost. Some workers (Rong, 2005; Zhu, 2004) reported that the peak around 1630 cm^{-1} and 1379 cm^{-1} indicates the presence of –C = C– bond. From the given spectra the peaks at 1600 cm^{-1} and around 1377 cm^{-1} are therefore due to the aromatic –C = C– bond.

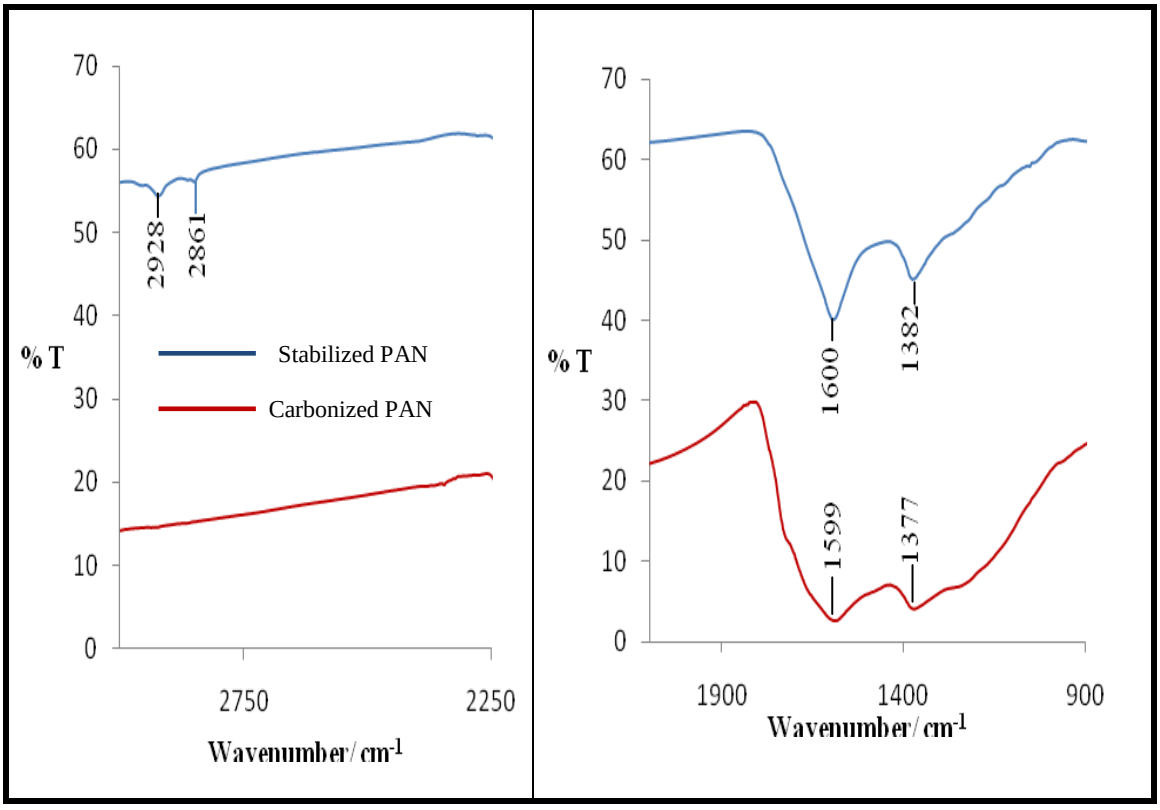

Figure 3.6: IR spectra of carbonized and stabilized PAN nanofibres.

3.4 Conclusions

The DSC analysis of PAN powder showed that low heating rates made cyclization start at a slightly lower temperature and less heat was produced. This means that there was less damage and fragmentation of the structure of polymer chains resulting in high performance carbon nanofibers (catalyst support). From these two techniques it was established that the fibres were successfully stabilized at a heating rate of 1 °C per minute up to 280 °C and the stabilized nanofibres carbonized at a heating rate of 5 °C per minute up to 600 °C.

References

Bajaj, P.; Screekumar, T. V.; Sen, K. *Polymer* **2001**, *42*, 1707–18.

Dresselhaus, M. S.; Dresselhaus, G.; Pimenta, M. A.; Eklund,P. C. *Analytical Application of Raman Spectroscopy* **1999**.

Deng, S.; Bai, R.; Chen J. P. *Journal of Colloid and Interface Science* **2003**, *260*, 265-272.

Farsani, R. E.; Raissi, S.; Shokuhfar, A.; Sedghi, A. *Materials Science* **2007**, 25.

Farsani, R. E.; Shokuhfar, A.; Sedghi, A. *International Journal of Mechanical, Industrial and Aerospace Engineering* **2007**, *1*, 4.

Klata, E.; Babel, K.; Krucinska, I. *Fibre and textiles in Eastern Europe* **2005**, *13*, *1*.

Ouyang, Q.; Cheng, L.; Wang, H.; Li K. *Polymer Degradation and Stability* **2008**, 93, 1415–1421.

Paiva, M. C.; Kotasthane, P.; Eddie, D. D.; Ogale, A. A. *UV stabilization route for melt-processible PAN-based carbon fibres* **2003**, *41*, 1399-1409

Qin, X. H. *Journal of Thermal Analysis and Calorimetry* **2009**.

Rong, Y.; Chen, H. Z.; Wu, G.; Wang, M. *Materials Chemistry & Physiscs* **2005**, *91*, 370.

Sedghi, A.; Farsani, R. E.; Shokuhfar. *Journal of materials processing technology* **2008**, *198*, 60-67.

Zhu, M.; Xing, Q.; He, H.; Zhang, Y.; Chen, Y.; Potschke, P.; Adler, H. J. *Macromolecular Symposia* **2004**, *210*, 251.

CHAPTER 4

4. Synthesis of titanium dioxide and its immobilization on PAN based carbon nanofibres

4.1 Introduction

The purpose of this study is to synthesize titanium dioxide nanoparticles using the sol-gel method and then immobilize them on carbon nanofibres. Many methods are available for synthesis of TiO_2 but the sol-gel method was chosen because it is very simple and allows easy control of particle size, shape and distribution (Barringer et al, 1985; Chen et al, 1995). The compositional and micro-structural tailoring is achieved by controlling precursor chemistry and processing conditions.

The Sol-gel process is a wet-chemical technique which has been widely employed in the fields of materials science, ceramic engineering and preparation of photocatalysts. This method is used for the fabrication of materials starting from a chemical solution which acts as a precursor for an integrated network (gel). It involves the formation of a metal-oxo-polymer network from molecular precursors. Typical precursors are metal alkoxides and metal chlorides which undergo hydrolysis and polycondensation reactions forming a system that contains both solid and liquid phases. Separation of the solid phase from liquid and drying is necessary resulting in shrinkage and densification. After drying, thermal treatment is also necessary to prevent further poly-condensation and to enhance structural stability.

Great care should be taken to control the reaction conditions because alkoxides hydrolyze intensely in air. Sivakumar et al, 2002, synthesized nanocrystalline anatase TiO_2 with a high surface area by homogenous precipitation of aqueous titanyl sulphate at ambient temperature. In this study titanium tetrachloride was used as the precursor. It reacts violently with water to produce toxic hydrogen chloride gas. When only water is used to synthesize TiO_2 particles, it is difficult to control the rate of hydrolysis. In order to control the rate of hydrolysis, modify the size and morphology of TiO_2 nanoparticles in aqueous phase, a stock solution of titanium ethoxide into which a few drops of glacial acetic acid were added was prepared. The molecules of ethanol and acetic acid could be adsorbed onto the amorphous precursor and this is likely to be oxidized to carbon dioxide during calcination thereby creating oxygen vacancies in the lattice thus enhancing rutile transformations at lower temperatures (John et al, 2005).

Various parameters of the sol-gel process influence the properties of the resulting TiO_2 nanoparticles. These parameters include the pH of the reaction medium, nature and concentration of catalyst, temperature, nature of hydrolytic solvent, precursor concentration and reactivity (type) among others. Of the parameters listed above, pH, concentration and temperature are usually suggested as the most important.

In this study the effect of concentration and temperature on the properties of the TiO_2 nanoparticles was investigated. It was expected that the temperature and precursor concentration would affect the hydrolysis rate resulting in formation TiO_2 nanoparticles with different size and shape.

4.2 Experimental

4.2.1 Materials

In this study all the chemicals were used as received without further purification. Titanium tetrachloride (99 %), absolute ethanol and *N*, *N* dimethylformamide (DMF) were supplied by Merk. Polyacrylonitrile (PAN) in the form of powder was supplied by Stellenbosch university.

4.2.2 Sol preparation

A 2.24 M stock solution of titanium ethoxide solution was prepared by mixing 12.46 ml of cooled titanium tetrachloride with 37.54 ml of absolute ethanol in a volumetric flask immersed in an ice water bath with vigorous stirring. The reaction was highly exothermic and it produced high quantities of hydrogen chloride gas fumes. The colour of titanium ethoxide stock solution was yellow and was stable with no formation of precipitate even after standing for a week at room temperature.

To 120 mmol of titanium ethoxide, ice cold ethanol/water mixture was added drop wisely with stirring to give a final concentration for Ti^{4+} of 0.78 mol dm^{-3}. A few drops of glacial acetic acid were added to control the rate of hydrolysis. The solution was stirred for 2 hours with heating at 60 °C to help eliminate chloride ions as hydrogen chloride gas. This treatment turned the solution white and turbid and the sol was aged for 12 hours at ambient temperature for gelation of the sol to occur.

4.2.3 Preparation of PAN/$Ti(OH)_4$ composite

Some titanium dioxide nanoparticles were so small that they were difficult to separate from the solution. Even after centrifugation for some time, the nanoparticles did not settle

down. To overcome this problem, polymer powder was added to the sol so that the polymer became coated with the nanoparticles. After the gelation process, PAN (2 g) was added followed by centrifugation and washing several times with water and anhydrous ethanol. Washing with ethanol helped to prevent agglomeration between the precipitates (Lee et al 2002). The PAN/$Ti(OH)_4$ complex was then air dried.

The above procedure was repeated at 25 °C, 40 °C, 80 °C and 120 °C. At each of the above temperatures the precursor concentrations were also varied and 1.3 M, 0.7841 M, 0.392 M and 0.0492 M were used. The ratio of water to ethanol was varied so as to keep the percentage of water which brings about hydrolysis the same in all experiments. A chart showing the different variations of the parameters used is shown in Figure 4.1.

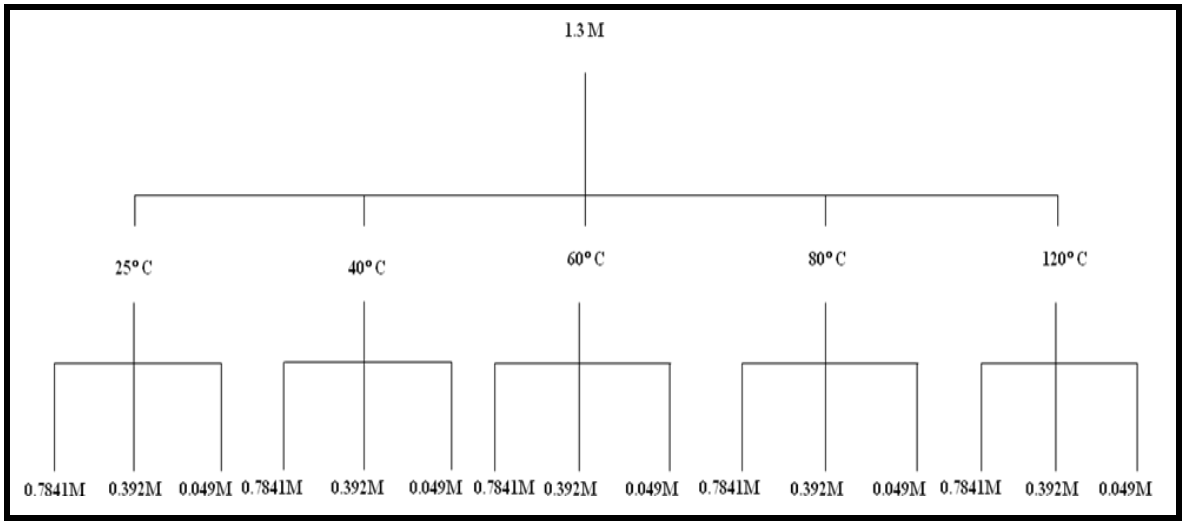

Figure 4.1: A graphical representation of the variations of sol-gel parameters.

The experimental conditions used for each run and the labels used for the samples are shown in Table 4.1.

Table 4.1: Experimental conditions for each run

Experiment Number	Concentration of $TiCl_4$ (mol/dm^{-3})	Temperature (°C)	Water content (vol. %)	Label
Exp. 1	1.3000	25	34.6	C4T1
Exp. 2	0.7841	40	34.6	C3T2
Exp. 3	0.3922	60	34.6	C2T3
Exp. 4	0.0492	80	34.6	C1T4
Exp. 5	1.3000	120	34.6	C4T5
Exp. 6	0.7841	25	34.6	C3T1
Exp. 7	0.3922	40	34.6	C2T2
Exp. 8	0.0492	60	34.6	C1T3
Exp. 9	1.3000	80	34.6	C4T4
Exp. 10	0.7841	120	34.6	C3T5
Exp. 11	0.3922	25	34.6	C2T1
Exp. 12	0.0492	40	34.6	C1T2
Exp. 13	1.3000	60	34.6	C4T3
Exp. 14	0.7841	80	34.6	C3T4
Exp. 15	0.3922	120	34.6	C2T5
Exp. 16	0.0492	25	34.6	C1T1
Exp. 17	1.3000	40	34.6	C4T2
Exp. 18	0.7841	60	34.6	C3T3
Exp. 19	0.3922	80	34.6	C2T4
Exp. 20	0.0492	120	34.6	C1T5

4.2.4 Preparation of TiO_2-encapsulated electrospun nanofibres

When titanium dioxide is used as a powder, its catalytic activity is higher than when encapsulated but there is a problem associated with the use of powder in water treatment.

There is need for separation of the nanoparticles from the water system and this limits its application. In this study immobilization on PAN-based carbon nanofibers was used to solve this problem.

The dried PAN/$Ti(OH)_4$ was dissolved in 18.98 ml of DMF and homogenized by magnetic mixing to give a 10 % polymer solution. After all the PAN had dissolved, the solution was stored at room temperature with magnetic stirring until it was ready for electrospinning to avoid the formation of a gel network. The solution was also sealed to prevent loss of solvent due to evaporation.

4.2.4.1 Electrospinning

The electrospinning apparatus set-up was described in Section 3.3.3.1 of Chapter 3. The conditions were the same as those used in Chapter 3.

4.2.4.2 Stabilization, calcination and carbonization

Stabilization is necessary to form a ladder structure that can withstand high temperatures during carbonization. During stabilization and carbonization, calcination of TiO_2 also occurs and it is important because it increases the crystallinity of the nanoparticles which enhances photocatalytic activity.

Using a programmable furnace supplied by MET-UD, the TiO_2/PAN nanofibre mats produced from electrospinning were heated at a rate of 1 °C/min up to 280 °C and maintained at this temperature for 2 hours. A photograph of the programmable furnace used in this study is shown in Figure 4.2.

Figure 4.2: A photograph of the furnace used for stabilization, calcination and carbonization.

After the stabilization process, nitrogen gas was purged into the furnace to remove unwanted air or oxygen. This was done to prevent oxidation of fibres at high temperatures. The PAN/TiO_2 composite nanofibres were then heated at a rate of 5 °C/min up to 600 °C in a nitrogen environment. This brought about both carbonization of the nanofibres and calcination of the embedded titanium dioxide nanoparticles. This process was done with the furnace in a fume hood to remove the toxic gases such as hydrogen cyanide produced during carbonization. The resulting carbon nanofibres were cooled down to room temperature in an inert gas atmosphere before they were taken out of the furnace. A chart outlining the methodologies used is shown in Figure 4.3.

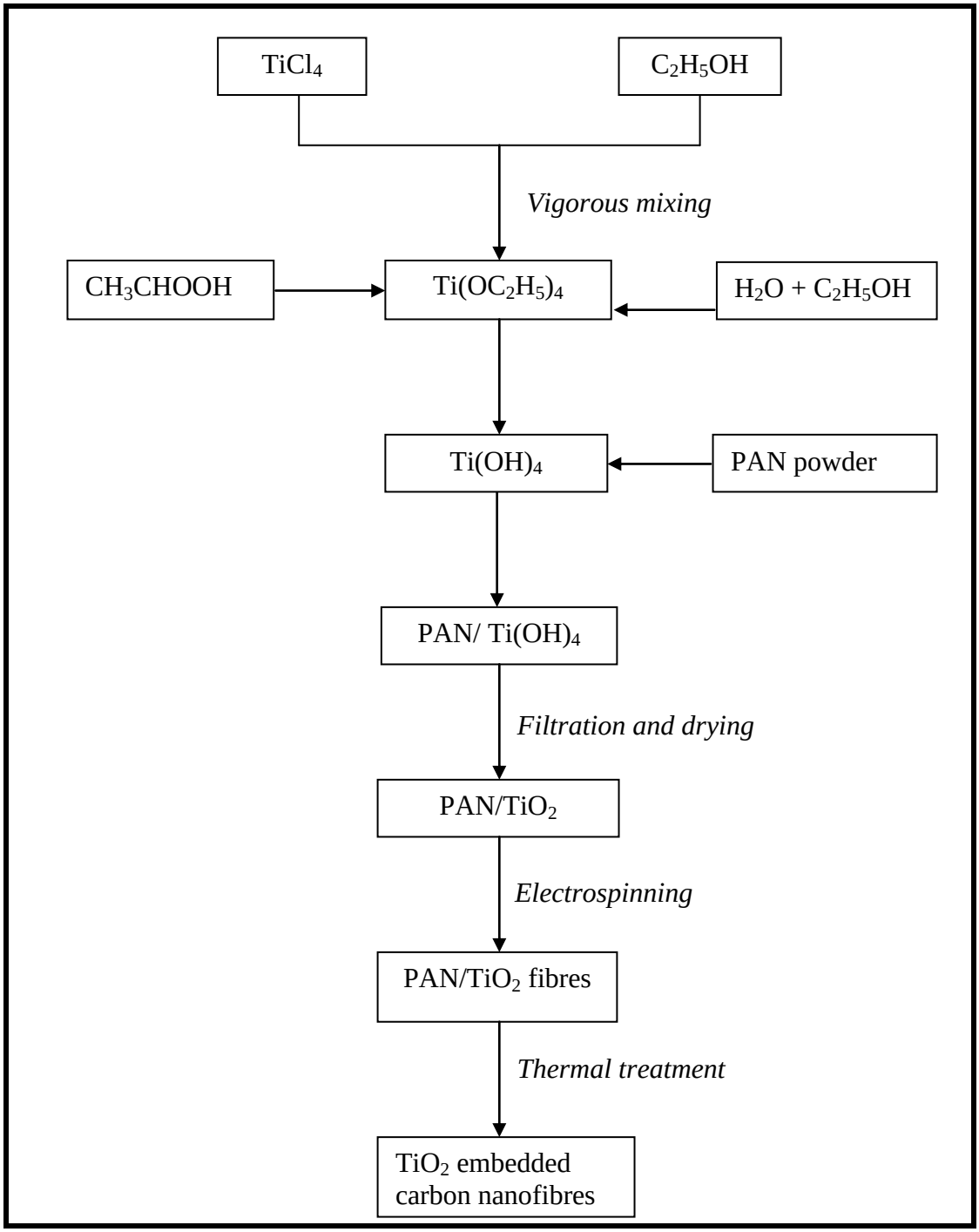

Figure 4.3: A Graphical representation of the methodology for the preparation of TiO_2 embedded carbon nanofibres.

4.3 Results and discussion

The $TiCl_4$ has been often used as a precursor by other researchers for the preparation of TiO_2 nanoparticles (John & Surender, 2005: Hosseinnia et al, 2010: Qourzal et al, 2006: Ouyang et al, 2008). In this study, TiO_2 nanoparticles were synthesized by controlling the hydrolysis of the precursor, $TiCl_4$. The prepared samples had different properties which all depended on the preparation conditions, including sol-gel temperature and precursor concentration. During the sol-gel process the reaction is thought to have taken place as follows (John & Surender, 2005).

$$TiCl_4 + 4C_2H_5OH \longrightarrow Ti(OC_2H_5)_4 + 4HCl \quad (5.1)$$

$$Ti(OC_2H_5)_4 + 4H_2O \longrightarrow Ti(OH)_4 + 4C_2H_5OH \quad (5.2)$$

$$Ti(OH)_4 \xrightarrow{-H_20} TiO_2{\cdot}H_2O \xrightarrow{-H_20} TiO_2 \quad (5.3)$$

When the sol-gel temperature was being varied it was noticed that as the temperature was increased, the time for formation of the sol decreased as indicated by the turbidity of the solution. The sol prepared at 25 °C and 40 °C took two hours to form but it was not as intense as those prepared at high sol-gel temperatures. At temperatures of 60 °C and 80 ° C the sol formed after forty minutes and at 120 °C it took 20 minutes. This shows that the hydrolysis rate increased with increase in temperature. Major differences in times taken for sol formation were observed at high precursor concentrations since at high concentrations and low temperatures the reaction seemed to be too slow. The yellowish colour of the ethoxide was still evident in the sol and gels prepared at 25 °C and 40 °C.

In the variations of concentrations, the hydrolysis rate increased with an increase in concentration at high temperatures and at low temperatures the reaction was very slow for high precursor concentrations. A concentration of 1.3 M was used in this study as the highest precursor concentration and this showed that particle formation was slow at low temperatures (25 °C and 40 °C). This was indicated by colour of the solution which had the yellowish colour of ethoxide.

4.4 Conclusions

Temperature and concentrations are important parameters in controlling the hydrolysis rate of titanium tetrachloride. It was observed that, for the same precursor concentration, an increase in temperature increased the hydrolysis rate. Concentrations above 1.2 M tended to prevent formation of the titanium dioxide nanoparticles at low temperatures. Hence it can be concluded that for the complete hydrolysis of $TiCl_4$ enough water should be added to the reaction mixture.

References

Barringer, E. A & Bowen, H. K. *Synthesis and Physical Properties*, *Langmuir* **1985**, *1*, 414–20.

Chen, Q.; Qian, Y.; Chen, Z.; Zhou, G.; Zhang, Y. *Materials Letters* **1995**, *22*, 77–80.

John, A.K & Surender, G.D. *Journal of Material of Science* **2005**, *40*, 2999 – 3001.

Lee, K. R.; Kim, S. J.; Song, J. S.; Lee, J. H.; Chung, Y. J.; Park, S. *Journal of American Ceramic society* **2002**, *85*, 341-45

Sivakumar, S.; Pillai, P. K.; Mukundan, P.; Warrier, K. G. K. *Materials Letters* **2004**, *58*, 2664-2669.

Hosseinnia, A.; Keyanpour-Rad, M.; Pazouki, M. *World Applied Sciences Journal* **2010**,*8*, 1327-1332.

John, A. K & Surender, G. D. *Journal of Materials Science* **2005**, *40*, 2999-3001.

Ouyang X.; Li, X.; Yan, H.; Qu, Y.; Mo, F. *Combustion, Explosion, and Shock Waves* **2008**, *44*, 597-600.

Qourzal, S.; Tamimi, M.; Assabbane, A. *Journal of Applied Sciences* **2006**, *6*, 1553-1559.

CHAPTER 5

5. Characterization of photocatalyst and nanofibres

5.1 Introduction

The unidirectional alignment, nanofibre diameter and rough estimate of nanoparticle size were examined by scanning electron microscope. The degree of crystallinity of PAN/TiO_2 nanofibres was investigated with an X-ray diffractometer. DSC and FT-IR were used to determine the extent of stabilization and carbonization of the PAN/TiO_2 nanofibres. XPS was used to determine whether the carbon and or nitrogen were incorporated in the TiO_2 lattice structure.

5.2 Experimental

In order to get the phase transition temperature of TiO_2 from anatase to rutile and the cyclization temperature of the PAN nanofibres containing $Ti(OH)_4$, a Perkin-Elmer DSC 7 differential scanning calorimeter equipped with Pyris software was used. An aluminium pan with 15 mg of PAN/$Ti(OH)_4$ nanofibres was placed in the sample chamber and an empty aluminium pan was placed in the reference chamber, and scanned from 25 °C to 600 °C at 5 °C/min. This temperature range used accommodated all the expected changes of PAN, PAN/$Ti(OH)_4$, and the TiO_2 . A plot of the heat flow against sample temperature was obtained as the thermogram. The onset temperature of the cyclization of PAN, Tg of PAN, conversion $Ti(OH)_4$ to TiO_2 and crystallization of TiO_2 was identified on the DSC thermogram.

To get detailed information on the thermal behavior of the titanium dioxide nanoparticles encapsulated by PAN nanofibres, a DTA analysis was done and compared with TGA and DSC.

Information about the functional groups and type of bonds present in the samples was obtained using FT-IR. The samples were mixed with KBr, ground and pressed into thin pellets.

The SEM analysis was performed on a JEOL JSM-6390LV Scanning Electron Microscope fitted with a secondary electron detector. The samples were gold coated first before analysis.

In order to determine the crystallinty of the TiO_2 nanoparticles, XRD patterns patterns were collected at iThemba Materials Laboratories in Faure, South Africa using a Bruker AXS instrument with a D8 Advance Diffractometer. The X-ray tube used a Cu-K_α radiation ((λ =1.5406 Å) and a gas positron sensitive detector, PSD Vantec-1 with 1600 channels.

5.3 Results and discussion

5.3.1 DSC analysis

The DSC thermograms of blank PAN and PAN/$Ti(OH)_4$ composite nanofibres are shown in Figure 5.3. There were minor discontinuities at the start of the thermograms which do not seem to be thermal events. The discontinuities are an undesired alteration in data related to the start of the DSC heating program (Brown, 1988).

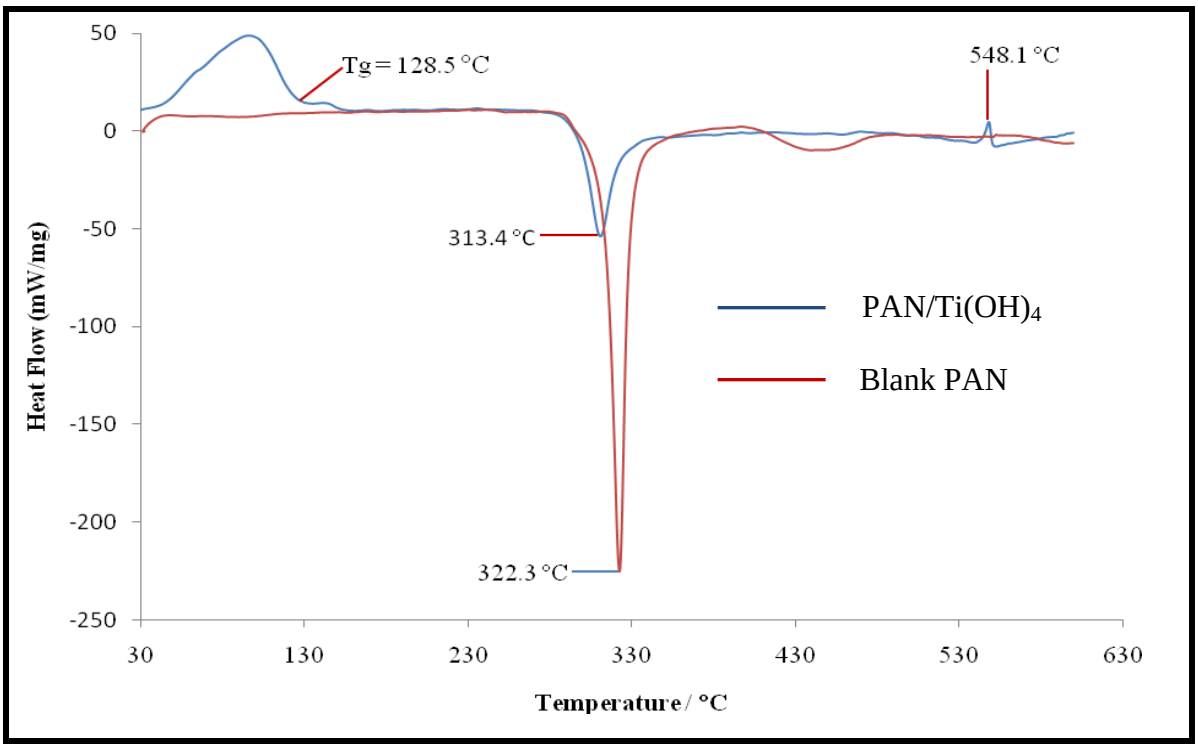

Figure 5.1: DSC curves of blank PAN and PAN/Titanium tetrahydroxide composite nanofibres.

There is an endothermic peak between 30 °C and 150 °C centered with a maximum at 90 °C due to the conversion (thermal decomposition) of $Ti(OH)_4$ to TiO_2, volatilization of some organic materials and evaporation/desorption of physically adsorbed water and solvent (ethanol) (Yu et al, 2000: Wen et al, 2001). The exothermic peak around 310 °C was common to both samples and can be attributed to the cyclization of the nitrile groups of PAN in both curves. The exothermic peak for the blank PAN was sharp and occurred at a higher temperature (322.3 °C) compared to that of PAN/$Ti(OH)_4$ which was small and occurred at a lower temperature (313.4 °C) and was probably due to the presence of titanium hydroxide which affected the exothermic reaction. This means that initiation of cyclization reaction occurred at a lower temperature due to titanium in the polymer compared to the neat PAN. The endothermic peak at 548.1 °C was due to amorphous to crystalline anatase-phase transformation of TiO_2 (Navio et al, 1992). It was also due to

tightly bound water probably in the form of hydroxyl groups since nanoparticles contain both tightly bound water and loosely bound water (Levechenko et al, 2006).

The presence of titanium hydroxide in the PAN helped in the determination of the glass transition temperature as shown in Figure 5.1. This is not clear in the curve of the pure PAN.

The literature value of glass transition temperature (Tg) of pure PAN is 125 °C and from the curves in Figure 5.1 the Tg of PAN containing titanium tetra-hydroxide is 128.5 °C showing an increment of 3.5 °C. This increment is probably due to the additive titanium tetra-hydroxide.

5.3.2 Characterization by TGA

Thermogravimetric analysis was used to determine the weight ratio between TiO_2 and carbon nanofibres in the composite, because the nanofibres can be readily burnt and eliminated at high temperatures around 790 °C as shown in Figure 5.2. It should be noted that, although the preparation conditions except the varied parameters had been kept constant there were some challenges such as the weather (humidity) which could not be controlled hence the moisture content of the hygroscopic samples prepared on different days could be different. All thermograms showed a decrease in weight between 0 °C and 300 °C due to evaporation of traces of the solvent and water. Samples PAN-T80 and PAN-T25 showed a huge weight loss between 20 °C and 120 °C perhaps because the samples did not dry completely during the drying process so they contained more water and solvent. The weight loss between 120 °C and 280 °C was small suggesting that there was only cyclization occurring in this step. After the entire polymer was completely burnt

between 700 °C and 800 °C the thermogram showed a constant weight suggesting that only TiO_2 remained.

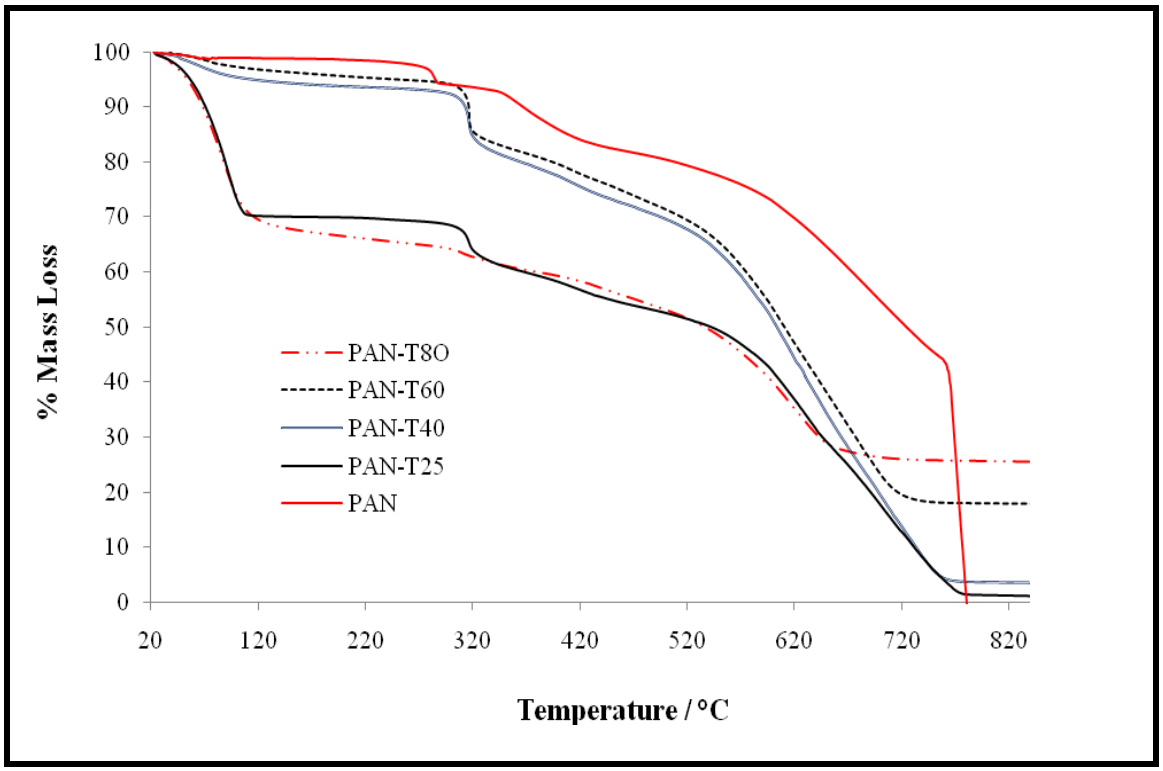

Figure 5.2: Thermograms of pure PAN and PAN/TiO_2 composite nanofibres. (PAN-T60 is PAN with TiO_2 prepared at 60 °C and PAN-T40 is PAN with TiO_2 prepared at 40 °C).

The amounts of TiO_2 nanoparticles formed at various temperatures differed and the thermograms showed that the yield increased as the temperature of the sol-gel process increased. At 25 °C, the TiO_2/PAN composite nanofibres contained roughly 2 % TiO_2, at 40 °C (5 %), at 60 °C (16 %) and at 80 °C contain 25 %.

The results also indicate that the onset of degradation for the TiO_2/PAN nanocomposite fibres occurred at a higher temperature than for the pure PAN nanofibres. The

degradation of pure PAN started at 283.3 °C, PAN-T40 at 314.9 °C and PAN-60 TiO_2 at 316.5 °C.

5.3.2.1 TGA and DTA analysis

The thermograms of PAN nanofibres with titanium dioxide prepared at a sol-gel temperature of 25 °C are shown in Figure 5.3.

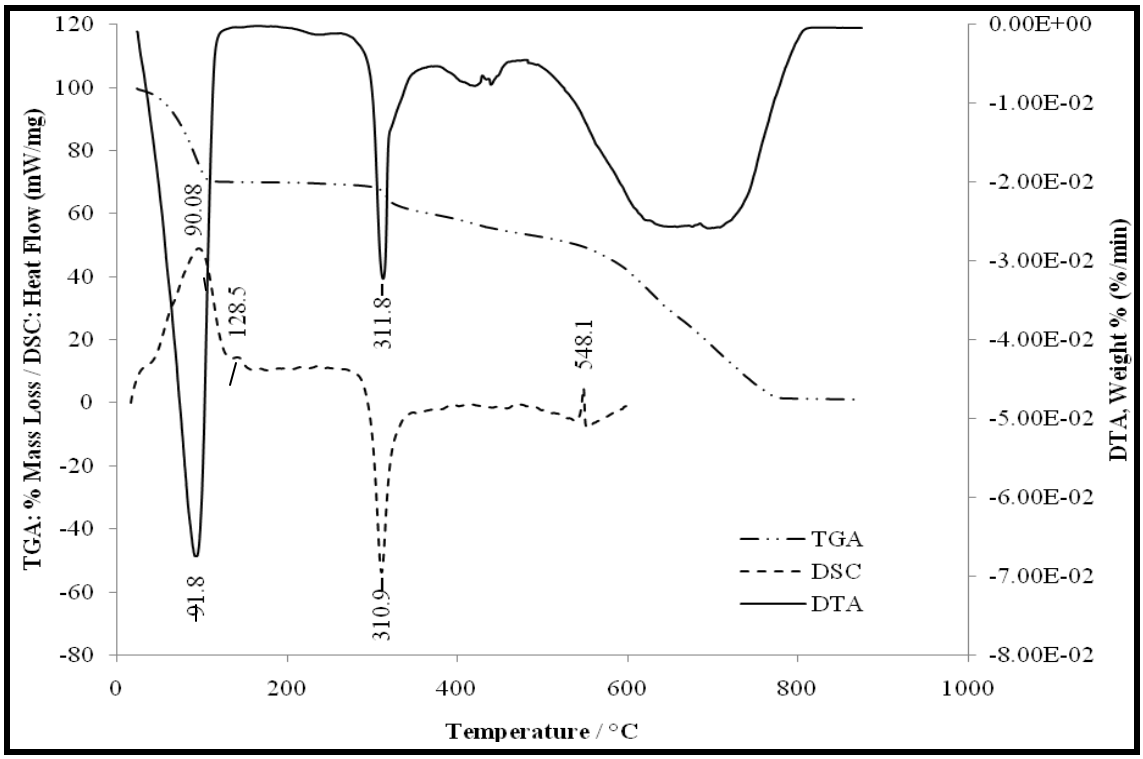

Figure 5.3: TGA, DTA and DSC curves of PAN-C3T1.

The TGA thermogram showed that there was a 30 % weight loss between 23.2 °C and 341.3 °C centered at 91.8 °C due to evaporation and desorption of solvent molecules and adsorbed water. The DTA peak at 91.8 °C corresponds to the endothermic peak observed in the DSC curve at 90.08 °C. The second weight loss ~5 % was between 265.2 °C and 341.23 °C with a maximum at 311.8 °C which was probably due to cyclization of the

nitrile groups. The maximum weight loss occurred between 472 °C and 810.7 °C corresponding to 95 % weight loss, this was probably due to elimination of the polymer through decomposition leaving only TiO_2 nanoparticles.

5.3.3 Characterization by FT-IR

The FT-IR spectra of the neat carbonized and stabilized PAN have already been reported in Section 3.4.2.2 of Chapter 3. In this section the spectra of PAN nanofibres containing titanium dioxide nanoparticles are given. The FT-IR spectra were obtained for the stabilized and unstabilized nanofibres containing TiO_2. The FT-IR spectra are shown in Figure 5.4 and they clearly show that the band at 2243 cm^{-1} which is assigned to –C≡N stretching decreased considerably in stabilized PAN/TiO_2 nanofibre compared to the same peak in the spectrum of the unstabilized PAN/TiO_2 nanofibres. The absorption peak of –C = N– band characteristic at 1590 cm^{-1} features in the spectrum of the stabilized PAN/TiO_2. This indicates that cyclization and dehydrogenation reaction have occurred during thermal/oxidative stabilization of PAN nanofibres. A new peak appears in the band at 1604 cm^{-1}, indicating that –C = C– (aromatic) has developed during the stabilization process which shows that an aromatic and more heat-resistant structure has formed. The peak around 3457 cm^{-1} is due to the OH group. Exposure of TiO_2 to water vapour causes hydroxylation of the surface by chemisorptions of water molecules. The peak between 500-700 cm^{-1} corresponds to Ti-O-Ti vibration of anatase (Hu et al, 2007).

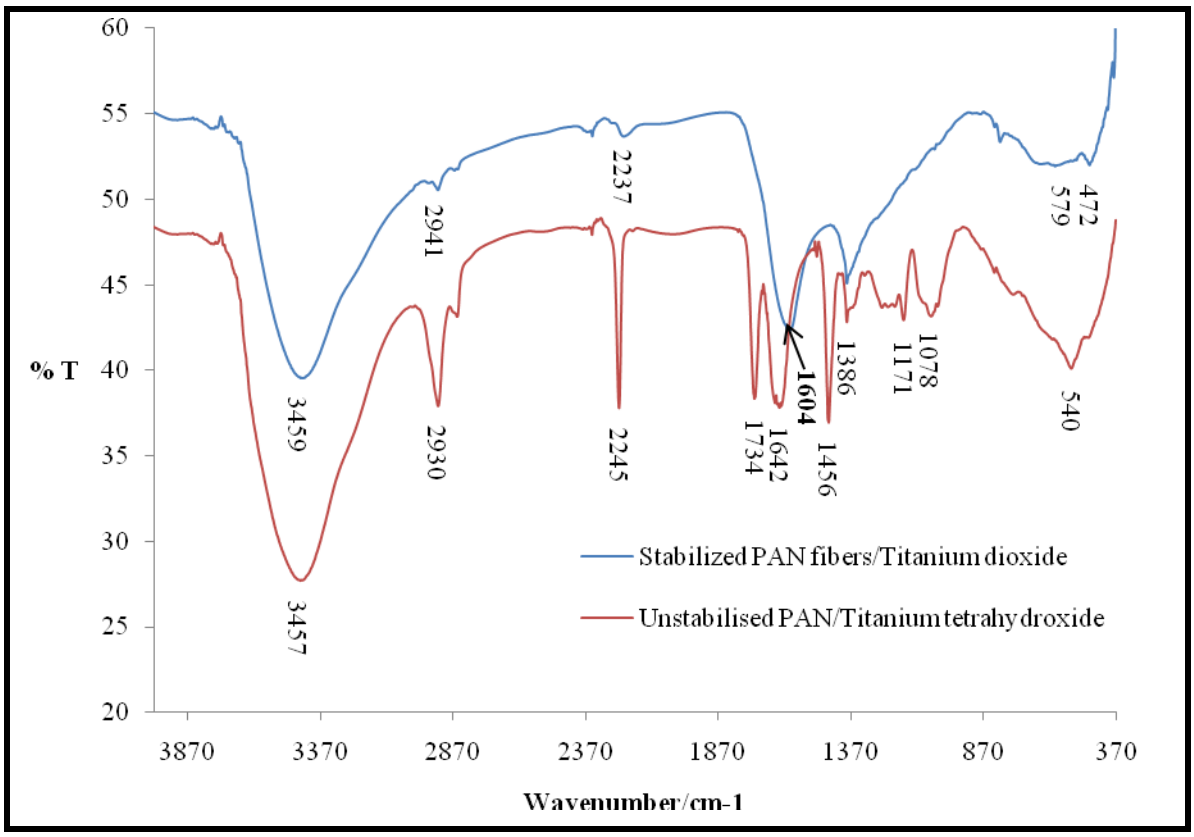

Figure 5.4: Infrared spectra of TiO_2 embedded stabilized nanofibres (SNF/TiO_2) and TiO_2 embedded carbonized nanofibres (CNF/TiO_2).

In the spectrum of unstabilized PAN/TiO_2, the peak at 1642 cm^{-1} is due to the –C = C– bond. The peaks at 1171 cm^{-1} (medium) and 1734 cm^{-1} (very sharp) are probably due to C=O of the residual DMF, since these peaks disappear in the spectrum of the stabilized PAN.

5.3.4 Characterization by SEM

The SEM images of the nanofibres containing TiO_2 nanoparticles prepared at different temperatures but from the same precursor concentration are shown in Figure 5.5. For these samples the precursor concentration used was 0.7841 M.

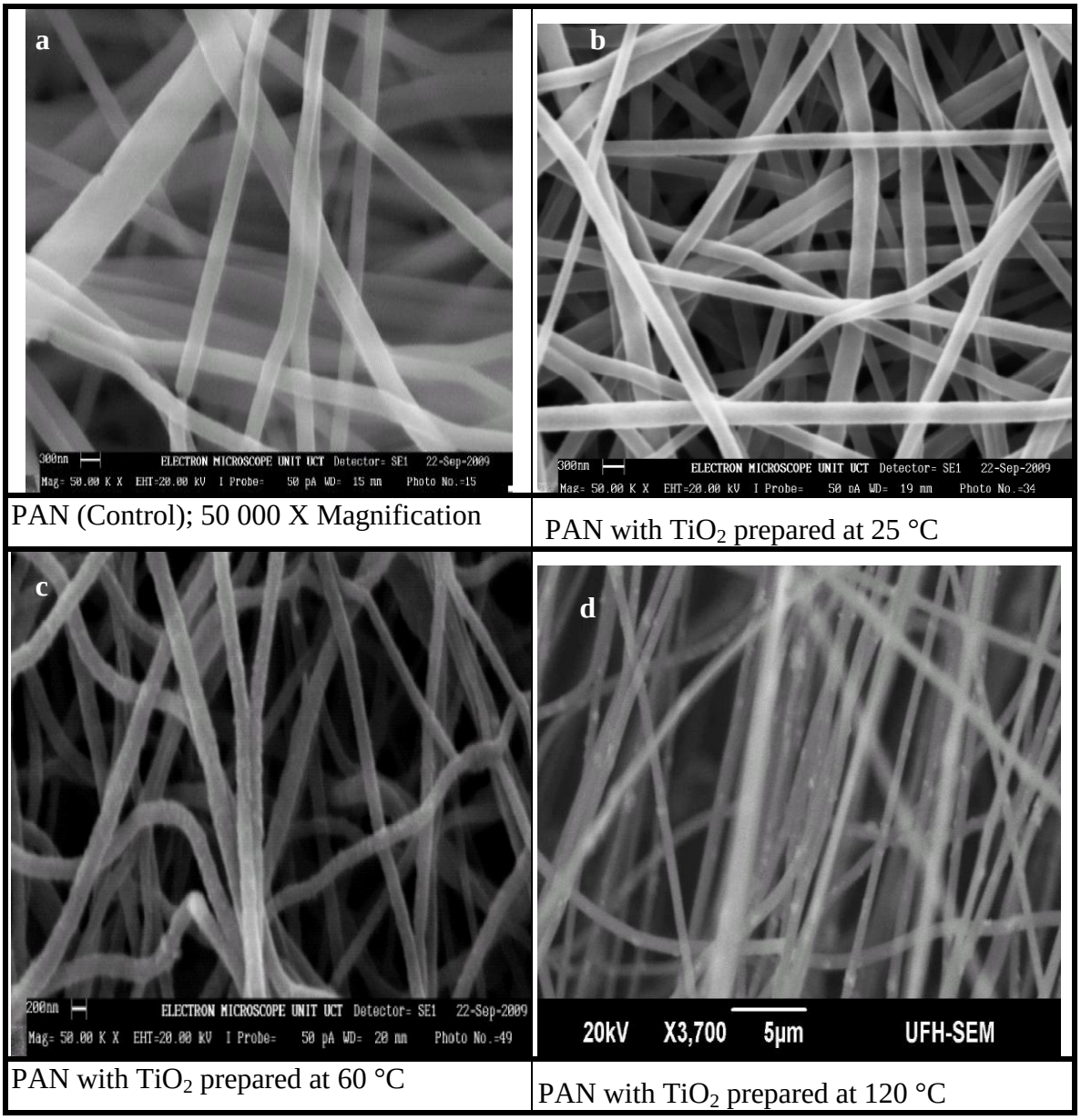

PAN (Control); 50 000 X Magnification

PAN with TiO_2 prepared at 25 °C

PAN with TiO_2 prepared at 60 °C

PAN with TiO_2 prepared at 120 °C

Figure 5.5: SEM images of TiO_2 embedded PAN fibres (magnification of b and c is 50 000).

The SEM images show that as the sol-gel temperature was increased, the size of the nanoparticles increased. The nanoparticles prepared at 60 °C and 120 °C could be seen on the fibres. Increase in sol-gel temperature increases the hydrolysis rate which results in larger particle size. Also an increase in temperature results in an increase in the thermal energy of the colloid, a decrease in the viscosity and the dielectric constant of the solvent,

thus lowers the electrostatic barrier against aggregation. These factors enhance the rate of aggregation resulting in bigger particles (Moon et al, 1995).

The SEM images of the PAN containing TiO_2 prepared at 40 °C did not show clearly the presence of TiO_2 particles indicating that they were either too small or they were very few since the reaction was slow. In this study the gelation time was the same in all experiments so hydrolysis at 25 °C and 40 °C was slow hence the reaction and gelation were not as complete as for temperatures of 60 °C, 80 °C and 120 °C as indicated by the turbidity of the solution. It was then decided to give the solutions more time for gelation so as to get gels comparable to other gels. The resulting particles formed were fewer and bigger as indicated by the SEM images in Figure 5.6 because at low temperatures, the particle number intensity decreases due to the increasing coagulation time.

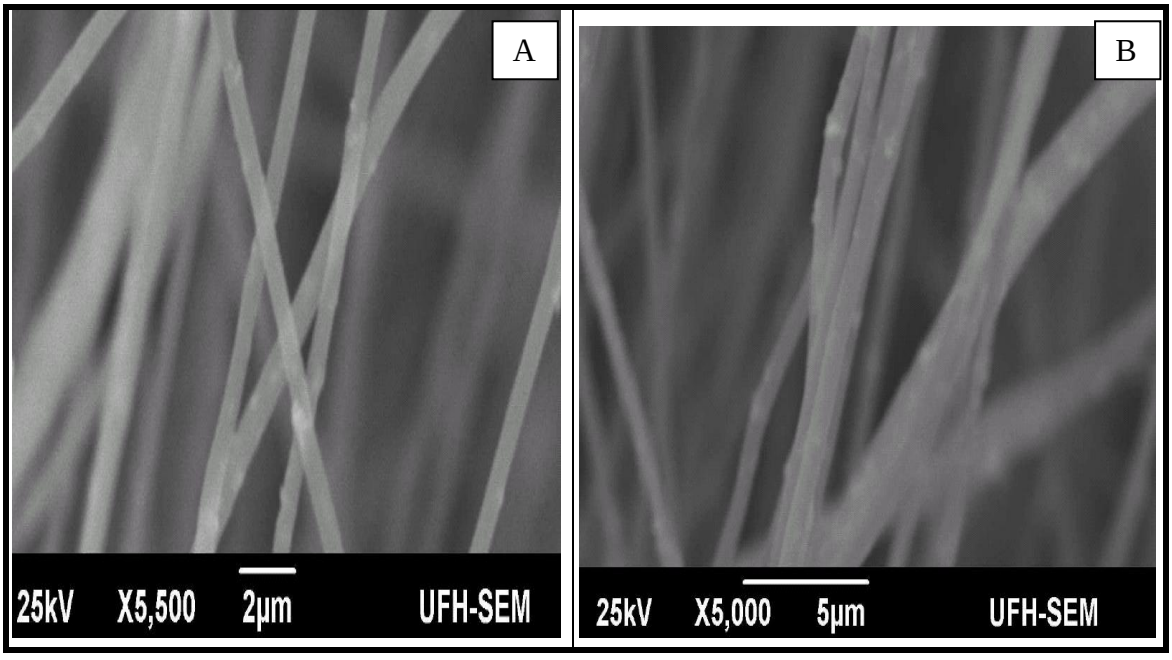

Figure 5.6: SEM Images of PAN nanofibres with TiO_2 prepared at 25 °C (A) and 40 °C (B).

For the chosen temperatures, the SEM images showed that the best temperatures for small particle size should be above 40 °C but below 120 °C.

The EDX results of the carbon nanofibres containing TiO_2 with codes C2T1 and C2T5 (Table 4.1) showed that all the expected elements were present in the samples. Carbon nanofibres containing C3T5 have 49.13 % C, 29.1 4 % O, 8.76 % Ti and carbon fibers containing C2T1 have 30.69% C, 37.36% O and 16.43% Ti. The EDX results of the chosen two samples are shown in figure 5.7.

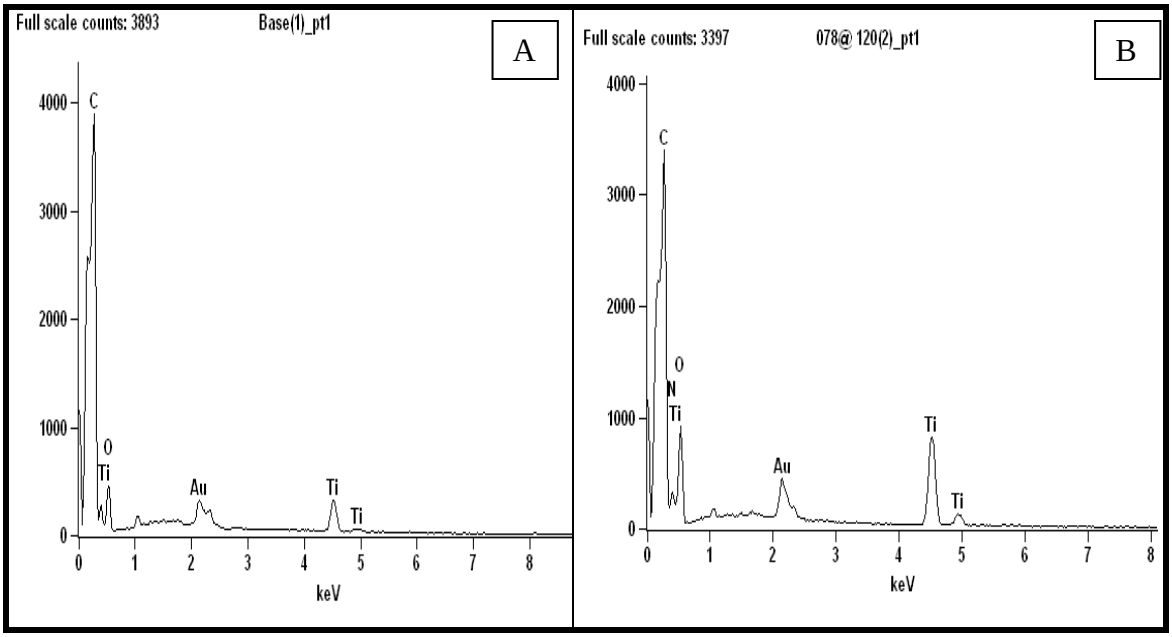

Figure 5.7: EDX spectra of carbon nanofibres containing TiO_2 prepared at (A) 25 °C and (B) 120 °C.

From the EDX spectra it can be seen that the amount of oxygen and titanium is lower for the sample prepared at 25 °C than that prepared at 120 °C indicating that at 120 °C more TiO_2 was produced (sol-gel process was basically complete at high temperatures).

When the concentrations were varied at constant temperatures of 60 °C, 80 °C and 120 °C it was noticed that as the precursor concentration increased, the particle size also increased. At temperatures of 25 °C and 40 °C, there seemed to be little or no formation of titanium dioxide at high precursor concentrations. The SEM images of the fibres were smooth and no visible particles were observed but when analysed by EDX, the presence of titanium was evident. It could be confirmed whether it was elemental titanium or the titanium of TiO_2 but there could be very few particles in the fibres. This is in agreement with what was reported by Zhou et al, 2008, that concentrations above 1.2 M tended to prevent formation of the titanium dioxide nuclei. In this study the best concentrations among those used were found to be 0.3922 M using a sol-gel temperature of 60 °C and 0.7841 M using a sol-gel temperature of 40 °C.

5.3.5 Characterization by XRD

Samples analyzed by XRD were given codes and the descriptions are shown in Table 5.1

Table 5.1: Sample codes for samples analyzed by XRD; carbon nanofibres with TiO_2 prepared at 25 °C to 120 °C

Sample Code	Temperature
CNF-T25	25 °C
CNF-T40	40 °C
CNF-T60	60 °C
CNF-T80	80 °C
CNF-T120	120 °C

The XRD patterns of PAN based carbon fibres containing TiO_2 nanoparticles prepared at different sol-gel temperatures are shown in Figure 5.8. The XRD pattern of pure PAN based carbon nanofibres is also shown as an insert.

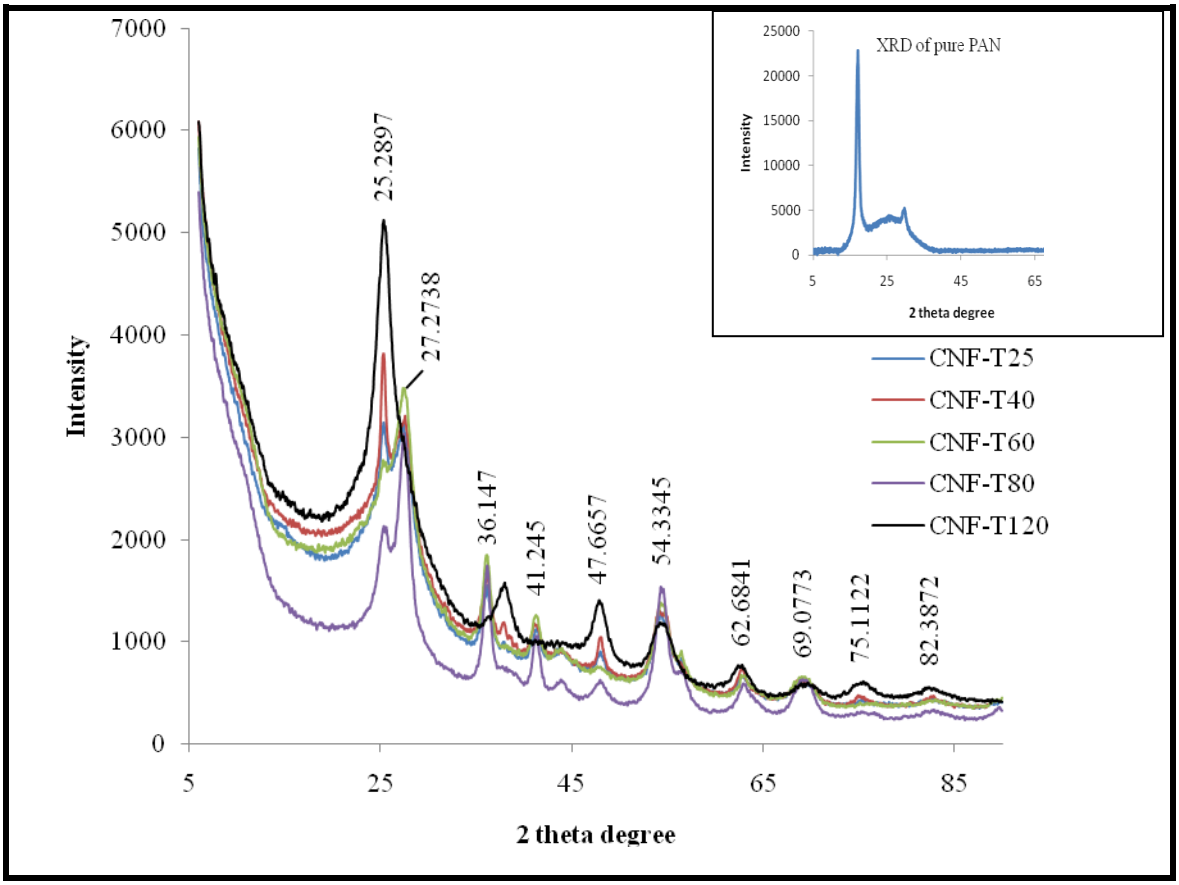

Figure 5.8: XRD patterns of TiO_2 embedded carbon nanofibres. The TiO_2 nanoparticles were all prepared with 0.3922 M $TiCl_4$ but at different temperatures.

Typically the nanofibres exhibit an equatorial peak (Zussman et al, 2005). In this study two equatorial peaks were observed at 2θ=17.1° and 2θ=29.1°. These peaks disappeared upon carbonization and post-oxidation as these peaks could not be seen in the XRD patterns of the TiO_2/carbonized nanofibres. The peaks at 2θ=27°, 36° and 54.3° indicate the presence of the TiO_2 in the rutile phase while peaks at 2θ=25.5°, 37.2°, 48°, and 62.6°

indicate the presence of the anatase phase. All the samples contained rutile and anatase phases, the difference was in the relative amounts as shown by the intensity of the peaks.

The XRD patterns for all the samples were similar except for CNF-T120 which did not show peaks at 2θ=27.2° and 36.1°, instead it had a sharp and very intense peak 2θ=25.2° meaning it contained more TiO_2 in the anatase phase. Generally the intensity of the peaks was higher for samples prepared at sol-gel temperatures above 60 °C. Kasetsart et al, 2008 reported that the intensity of diffraction peaks increases with particle size and Speakman reported that very small nanocrystallites produce weak signals, so from these results we can conclude that at 0.3922 M $TiCl_4$, temperatures between 25 °C and 60 °C gave the smallest crystalline nanoparticles. The results also prove that a sol-gel temperature of 120 °C does not favour rutile phase formation.

The XRD patterns for carbon nanofibres containing TiO_2 prepared at 60 °C but using different precursor concentrations are shown in Figure 5.9 and the sample codes are shown in table 5.2.

Table 5.2: Sample codes and description

Sample code	Description
PAN-C4T3	CNF with TiO_2 prepared with 0.0490 M Ti^{4+}
PAN-C3T3	CNF with TiO_2 prepared with 0.3922 M Ti^{4+}
PAN-C2T3	CNF with TiO_2 prepared with 0.7841 M Ti^{4+}
PAN-C1T3	CNF with TiO_2 prepared with 1.3000 M Ti^{4+}

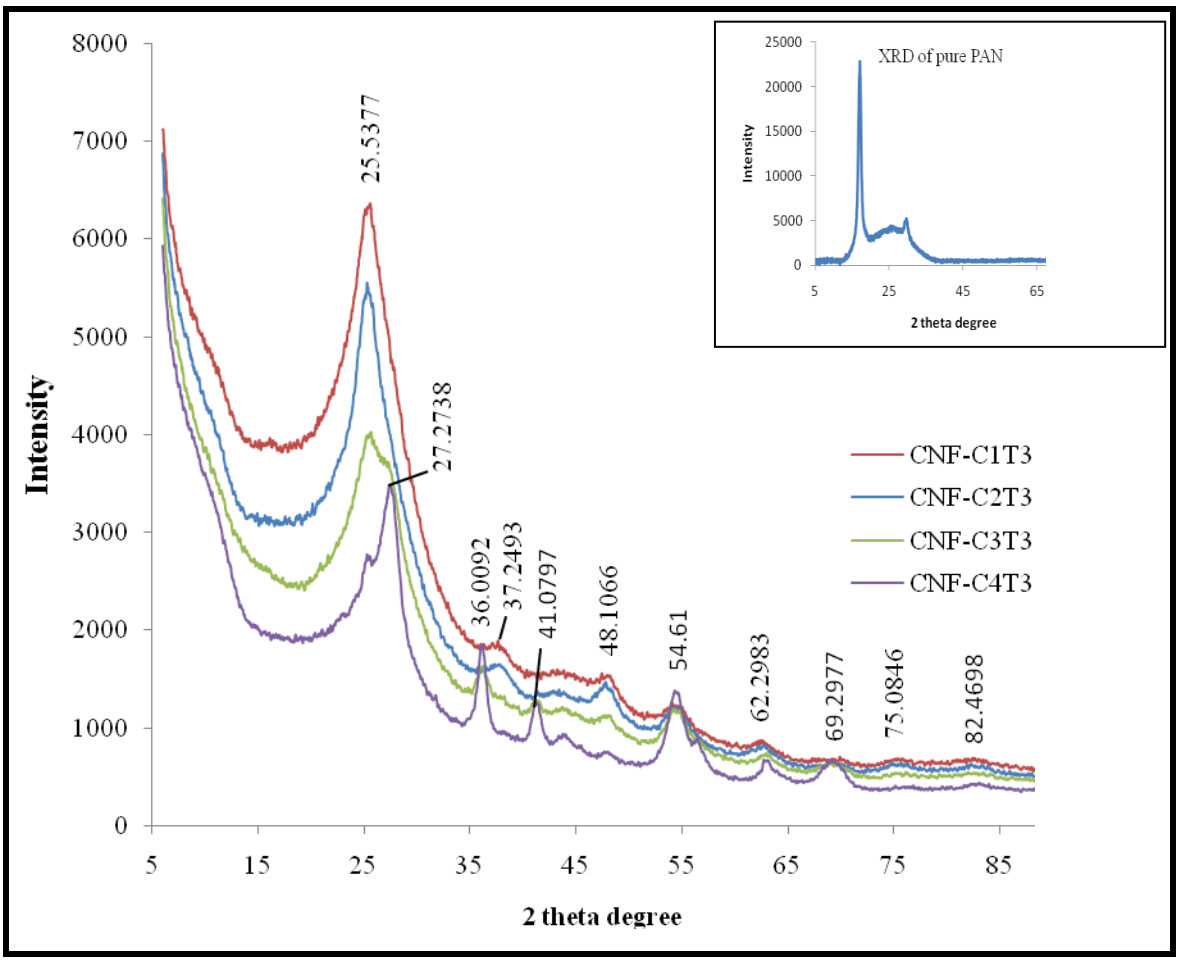

Figure 5.9: XRD pattern of PAN containing TiO_2 prepared at 60 °C with different concentrations.

The XRD patterns agree well with the patterns of TiO_2 in literature and they all show the presence of both anatase and rutile phases. As reported in the previous section, peaks at 2θ = 27°, 36° and 54.5° indicate the presence of the TiO_2 in the rutile phase while peaks at 2θ=25.5°, 37.2°, 48°, and 62.2° indicate the presence of the anatase phase. Sample PAN-C1T3 shows three strong peaks due to the rutile phase while the other three samples prepared at lower concentration show only one peak at 2θ=54.5° due to rutile. In this sample a peak due to anatase at 2θ=25° is very small compared to other samples showing that the anatase phase is the major phase at low precursor concentrations and rutile is the

major phase at high precursor concentrations. From the previous section it was shown that the largest particle size was obtained with a concentration of 1.3 M, so these results show that the diffraction peak intensity of the TiO_2 increases with an increase in particle size and this is in agreement with what was observed by Kasetsart et al, 2008. The results also show that if the concentration is high, the crystallinity of TiO_2 increases as shown by the sharpness of the peaks, and the transformation from anatase to rutile occurs easily. The broadness of the peaks indicates either particles of very small crystalline size or the particles were semicrystalline (Yeha et al, 2004). The transformation from anatase to rutile is due to formation of large particle sizes at high concentration. Zhang & Banfield, 1998) reported that the critical size at which anatase starts to transform to rutile is ~14 nm and if the size of the particle is above 14 nm, rutile is favoured since it will be more stable than anatase.

5.3.6 Characterization by TEM

TEM is a powerful technique for the determination of particle size. Based on SEM results, two samples were chosen for TEM observation. The analysis was done on a JEM-100S TEM instrument. In this study particle size determination was based on direct measurement of the particles on the TEM images. The images of the TiO_2 embedded carbon nanofibres are shown in Figure 5.10. They show that particle size distributions are in the range 2 nm - 5 nm for the sample prepared at 60 °C using a concentration of 0.3922 M and 15 nm – 30 nm for a sample prepared at 80 °C using a concentration of 0.7841 M.

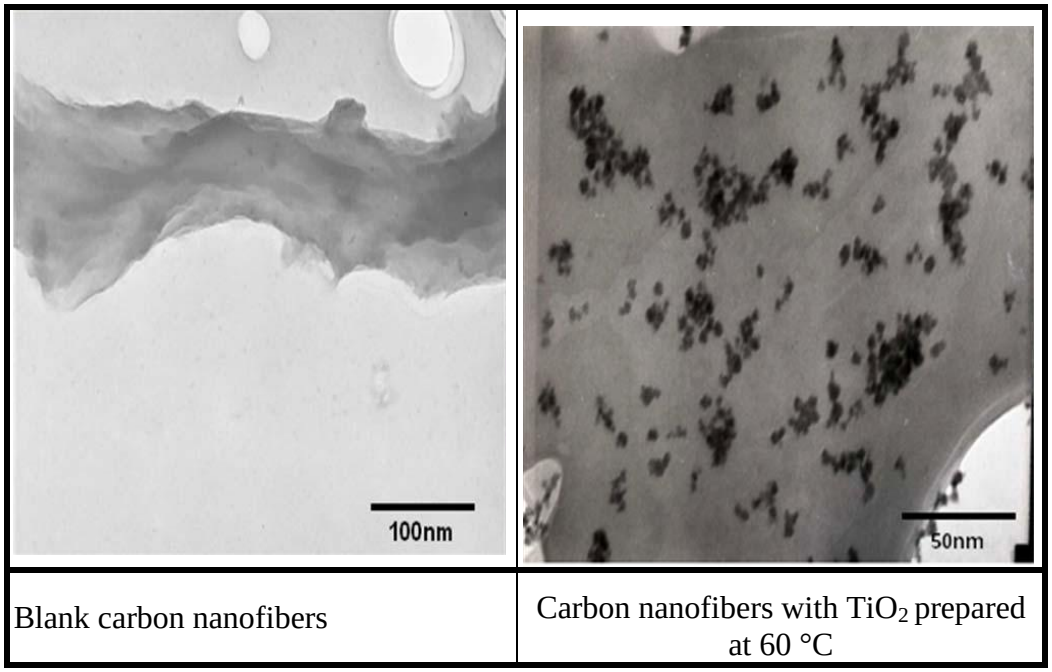

Blank carbon nanofibers

Carbon nanofibers with TiO_2 prepared at 60 °C

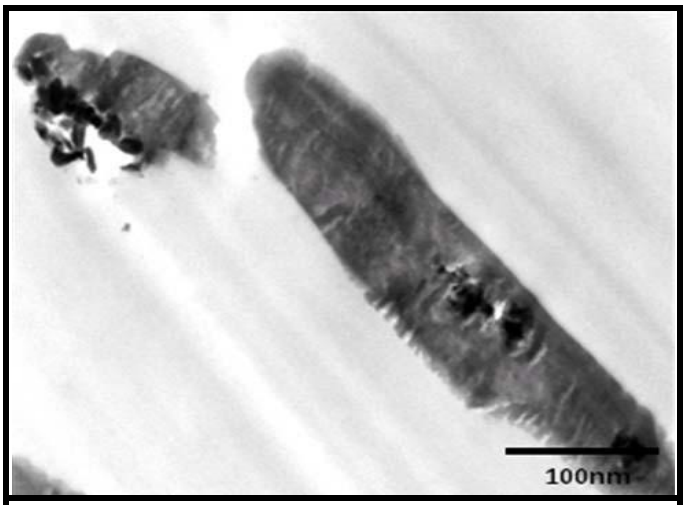

Carbon nanofibers with TiO_2 prepared at 80 °C

Figure 5.10: TEM images of some of the TiO_2 embedded carbon nanofibres.

5.4 Conclusions

In this study, based on the SEM results, the best concentrations among those used were found to be 0.3922 M when the sol-gel temperature was 60 °C and 0.7841 M when the sol-gel temperature was 40 °C. When the samples were further analyzed by TEM and XRD, we can conclude that the best sol-gel temperature was 60 °C using a precursor

concentration of 0.3922 M. Increase in both temperature and precursor concentration resulted in an increase in particle size. From the XRD results it can be concluded that, temperature is a more important parameter than concentration in controlling the properties of TiO_2 such as crystallinity and particle size. At high sol gel temperatures, rutile phase formation was not favoured.

References

Farsani, R. E.; Shokuhfar, A.; Sedghi, A. *International Journal of Mechanical, Industrial and Aerospace Engineering* **2007**, *1*, 4.

Ouyang, Q.; Cheng, L.; Wang, H.; Li, K. *Polymer Degradation and Stability* **2008**, 93, 1415–1421.

Hu, G.; Meng, X.; Feng, X.; Ding, Y.; Zhang, S.; Yang, M. *Journal of Materials Science* **2007**, *42*, 7162–7170

Navio, J. A.; Macias, M.; Gonzalez-Catalan, M.; Justo, A. *Journal of Materials Science* **1992**, *27*, 3036.

Yu, J. G.; Xiujian. Z.; Qingnan Z. *Thin Solids Films* **2000**, *379*, 7.

Wen, T.; Gao, J.; Shen, J.; Zhou, Z. *Journal of materials science* **2001**, *36*, 5923-5926

Levchenko, A. A.; Li, G.; Boerio-Goates, J.; Woodfield, B. F.; Navrotsky, A. *Chemistry of Materials* **2006**, *18*, 6324–6332

Zussman, E.; Chen, X.; Ding, W.; Calabri, L.; Dikin, D. A.; Quintana, J. P.; Ruoff, R. S. *Carbon* **2005**, 43, 2175–2185.

Brown, M. E. *Introduction to Thermal Analysis Techniques and Applications* **1988**.

Yeha, C. L.; Yeh, S. H.; Ma, H. K. *Powder Technology* **2004**, *145*, 1.

Zhang, H. & Banfield, J. F. *Journal of Materials Chemistry* **1998**, *8* 2073-2076.

CHAPTER 6

6. Preparation of carbon and nitrogen doped TiO_2 and photocatalytic activity evaluation

6.1 Introduction

Titanium dioxide is a good photocatalyst for the degradation of organic pollutants but it has a wide band gap of 3.2 eV and can only absorb light of wavelength of less than 388 nm. To be able to utilize a wide range of the solar spectrum, the band gap should be narrowed. A lot of studies have been done with the goal of improving the optical absorption that is to shift the optical response from UV to the visible region (Chen et al, 2007, Huanga et al, 2006, Rengaraji & Li, 2006). Among these studies, it is the doping with nitrogen and carbon which lowers the band gap through introduction of 2p states. The dopant-induced energy levels within the band gap make it easy for the formation of electron-hole pairs under UV illumination. It can also be achieved by using transition metals but the metal doped TiO_2 suffers from thermal instabilities and formation of carrier recombination centres (Choi et al, 1994). The experimentally observed trend for the band gaps of the polymorphs of TiO_2 follow the trend Eg (rutile) < Eg (anatase) < Eg (brookite) when all are computed consistently (Mo & Ching, 1995).

In this chapter the modification of TiO_2 nanoparticles by doping with carbon and nitrogen using different loadings of the dopant source is described. The band gap of doped TiO_2 can be determined typically by diffuse reflectance spectroscopy or by applying the Kubelka-Munk treatment to the diffuse reflectance spectra.

6.2 Experimental

6.2.1 Preparation of carbon doped TiO_2

The procedure for the preparation of carbon doped TiO_2 is the same as that reported in Section 5.2 with the addition of glucose during the sol-gel process. In this preparation, a 0.3922 M $TiCl_4$ was used and the sol-gel temperature was 60 °C. To investigate the effect of loading level, three different concentrations of glucose were used and these were 0.093 M, 0.185 M and 0.278 M. A schematic of the preparation of the carbon doped TiO_2 is shown in Figure 6.1.

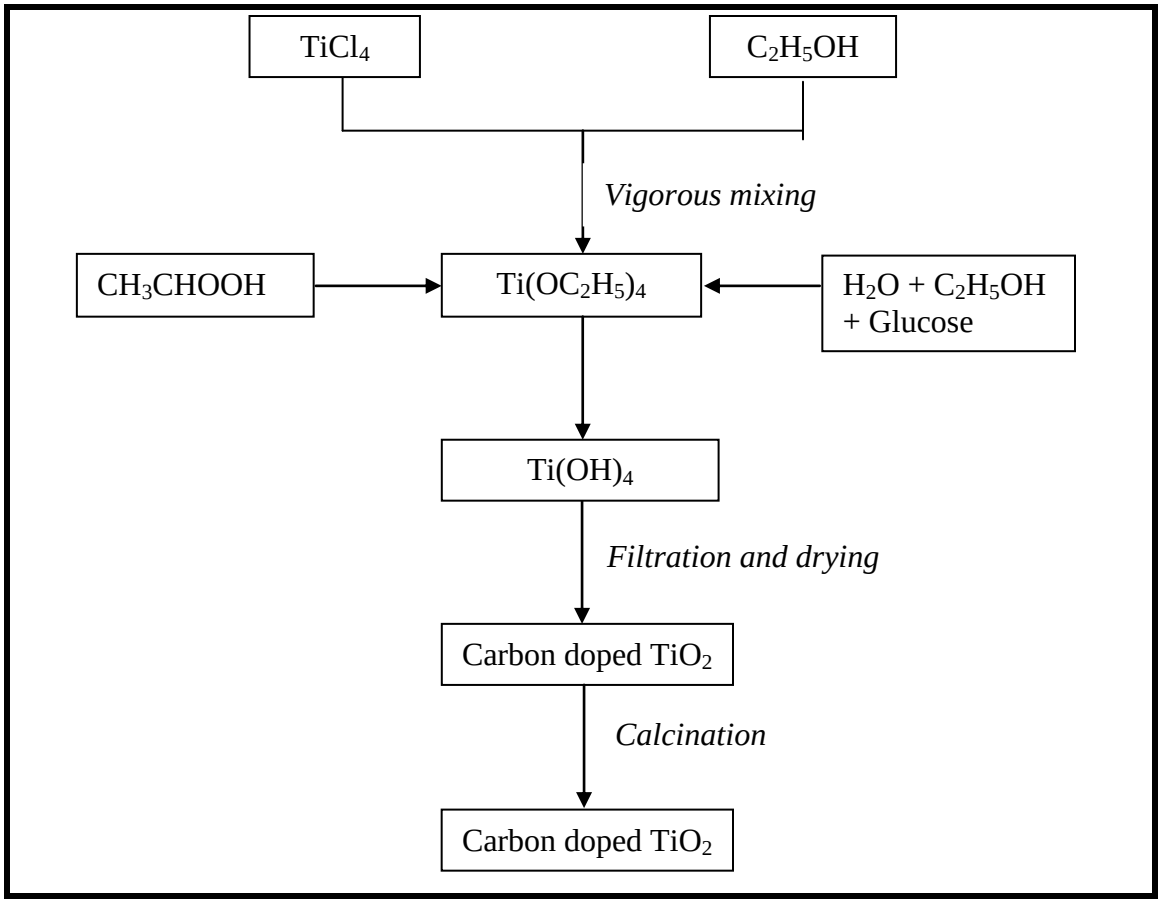

Figure 6.1: A graphical representation of the preparation of doped TiO_2.

6.2.2 Preparation of nitrogen doped TiO_2

The procedure for the preparation of the nitrogen doped TiO_2 is the same as reported in Section 6.2.1 but with the addition of urea as the nitrogen source. The same concentrations and experimental conditions were used.

6.2.3 Photocatalytic activity measurements

The methyl orange was obtained from Saarchem, South Africa and was used without further purification. Before the photocatalytic activity evaluations, the UV-Vis spectrum of the methyl orange was obtained on a Perkin Elmer Lambda 35 UV–Vis spectrometer and recorded from 200 nm to 600 nm to determine maximum absorption wavelength (λ_{max}). A standard solution of methyl orange (5 mg/L) prepared in double distilled water was used for the λ_{max} determination.

The time needed to reach adsorption equilibrium was also determined before the photocatalytic degradation experiments. This was done by immersing TiO_2/PAN nanofibres (0.1 g) in 100 ml of methyl orange in a flask and wrapped with aluminium foil. The reactor with a cylindrical geometry was then placed in the dark with stirring. After every thirty minutes aliquots of methyl orange were taken and the concentration determined using a UV-Vis spectrometer. When there was no change in absorbance, this suggested that there was no change in concentration thus implying that equilibrium had been reached.

The photocatalytic degradation of methyl orange by TiO_2/PAN fibres under UV illumination was monitored by using a lamda 35 UV–Vis spectrometer manufactured by

PerkinElmer Singapore at λ_{max} = 468 nm. The spectrum was recorded from 200 nm to 600 nm. A 40 W UV, 220V (50/60Hz) lamp was used as the source of light.

In all experiments a 100 ml of 5 ppm methyl orange solution was placed in a conical flask and then 0.1 g of TiO_2/PAN nanofibre sheet immersed in the solution. The flask was wrapped with aluminum foil then placed in the dark for an hour for adsorption to take place. The system was then irradiated with UV light from a lamp that was fixed in the middle of the system and 12 cm above the surface of the solution. A few drops of hydrogen peroxide were added to capture the electrons. To detect changes in concentration, aliquots of methyl orange (5 mL) were taken after every 30 minutes and centrifuged. The absorbance of the clean solution was measured by UV-Vis spectrometer.

The extent of methyl orange decolourisation was calculated using the equation $C(\%) = (A_0 - A)/A_0 \times 100$, where C is the decolourisation degree, A_0 the initial absorbance of methyl orange solution, and A the absorbance of the methyl orange solution after photocatalysis.

6.3 Results and discussion

6.3.1 Characterization: DRS, ESR, SXPS, FTIR

6.3.1.1 Analysis by Diffuse reflectance spectroscopy

The diffuse reflectance spectra (DRS) of the samples were acquired at room temperature using a diffuse reflectance attachment of a Cary 500 UV-Vis –NIR spectrophotometer. The spectra were acquired from 800 nm to 200 nm.

(i) Carbon doped TiO_2

The diffuse reflectance spectra of the carbon doped TiO_2 is shown in Figure 6.2. The UV-visible absorption spectra were shifted by 7 nm~36 nm according to the doping level. The highest shift was due to TiO_2 doped with 0.093 M glucose. The absorbance increased with a decrease in the loading of the glucose indicating that a higher amount of the glucose had an effect on the sol-gel process and also on the particle size. The higher the amount of glucose added the smaller the particle size hence absorption occured at short wavelengths since the band gap increases as particle size decreases. The results show that the carbon doped TiO_2 behaved as a photocatalyst under visible light illumination but at low dopant loading.

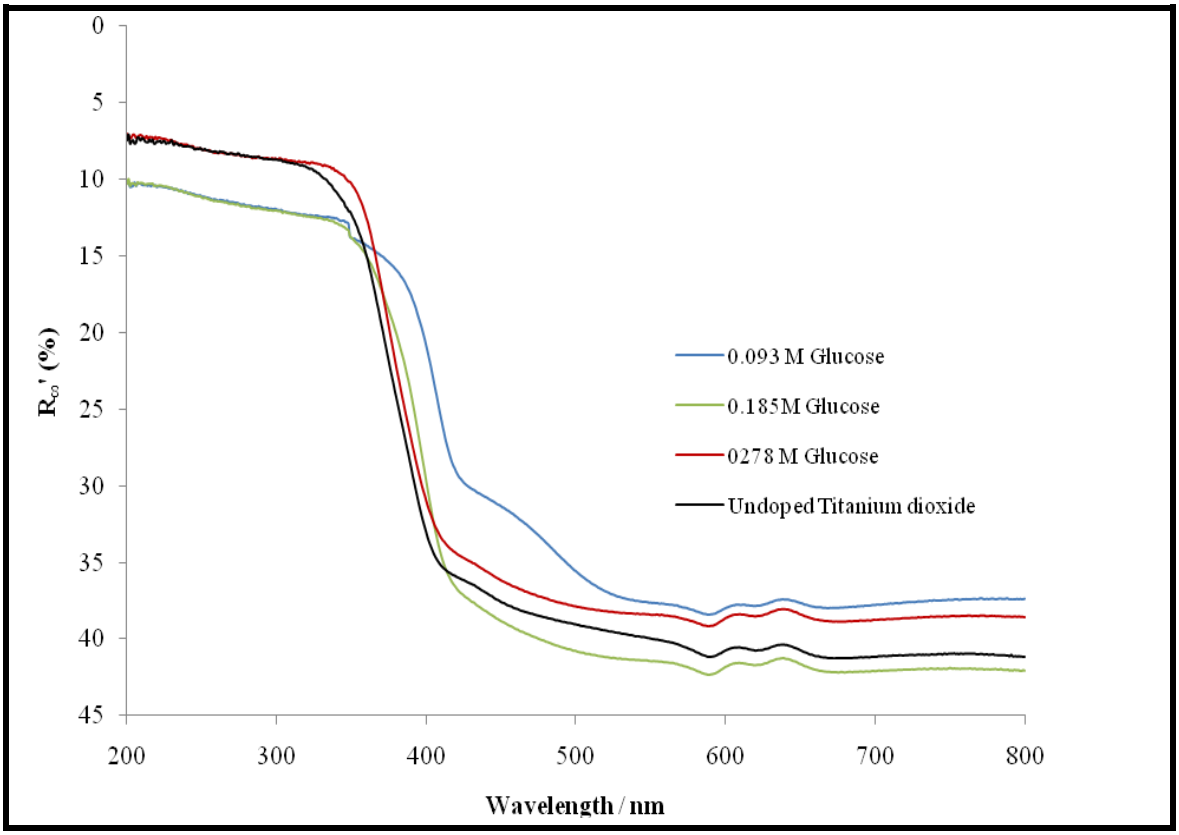

Figure 6.2: Diffuse reflectance spectra of carbon doped TiO_2 with different carbon concentrations.

The band gaps of the doped samples were determined by the equation Eg =1239/λ_{edge} (where λ_{edge} is the wavelength of the optical absorption edge) (Weng et al, 2004). The calculated band gap energies are shown in Table 6.1.

Table 6.1: λ_{edge} and the calculated band gap energies of TiO_2 with different carbon concentrations.

Glucose concentration (M)	λ_{edge} (nm)	Band gap (eV)
0.000	420	2.95
0.093	456	2.72
0.185	432	2.87
0.278	427	2.90

(ii) Nitrogen doped TiO_2

The diffuse reflectance spectra of the nitrogen doped TiO_2 is shown in Figure 6.3. The UV-visible absorption spectra were shifted to higher wavelength by 2 nm~8 nm. The absorbance of nitrogen doped samples increased as the dopant source concentration was increased from 0.093 M to 0.185 M but when the concentration was 0.278 M, the absorbance shifted to a shorter wavelength showing a reduction in band gap.

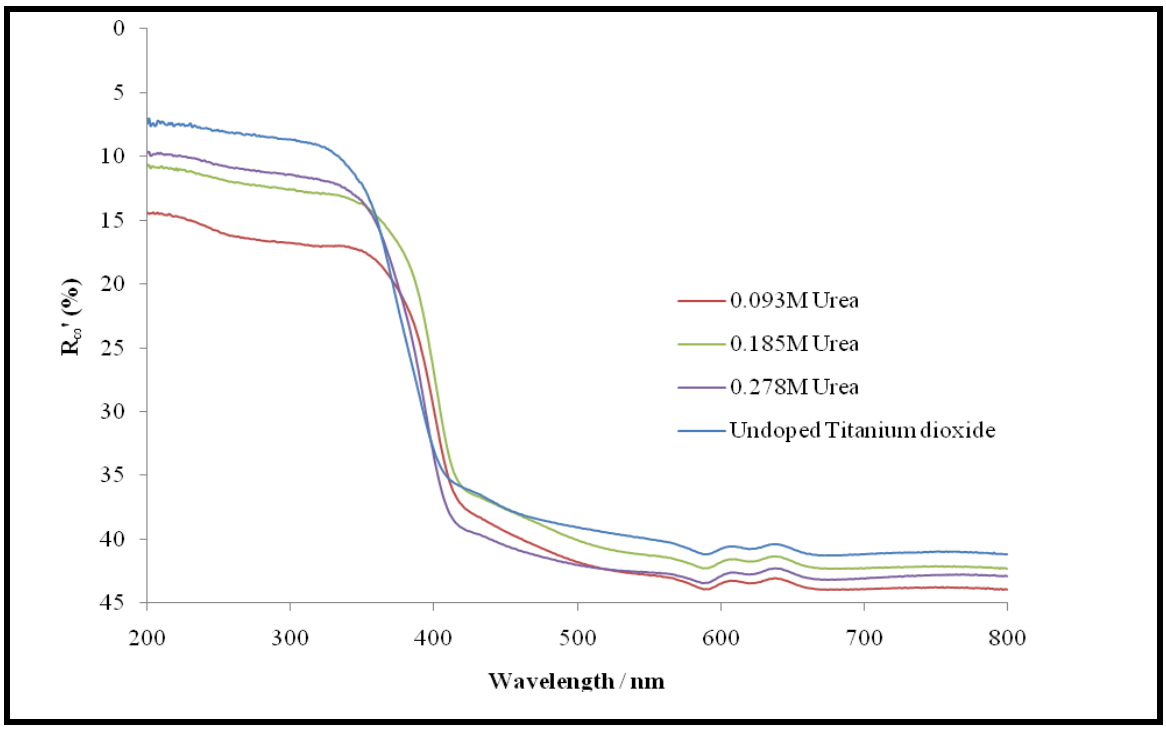

Figure 6.3: Diffuse reflectance spectra of nitrogen doped TiO_2 with different nitrogen concentrations.

The calculated band gap energies for the nitrogen doped titanium dioxide nanoparticles using different concentrations of urea are shown in Table 6.2. The smallest band gap energy achieved by nitrogen was 2.89 eV showing a reduction in band gap of 0.06 eV from 2.95 eV for the undoped TiO_2.

Table 6.2: Wavelength (λ_{edge}) values and the calculated band gap energies of TiO_2 with different dopant (urea) concentrations.

Urea concentration (M)	λ_{edge} (nm)	Band gap (eV)
0.000	420	2.95
0.093	426	2.91
0.185	428	2.89
0.278	422	2.94

(iii) Comparison of carbon and nitrogen doped TiO_2

The diffuse reflectance spectra of TiO_2 doped with the same loadings of carbon and nitrogen source are shown in Figure 6.4.

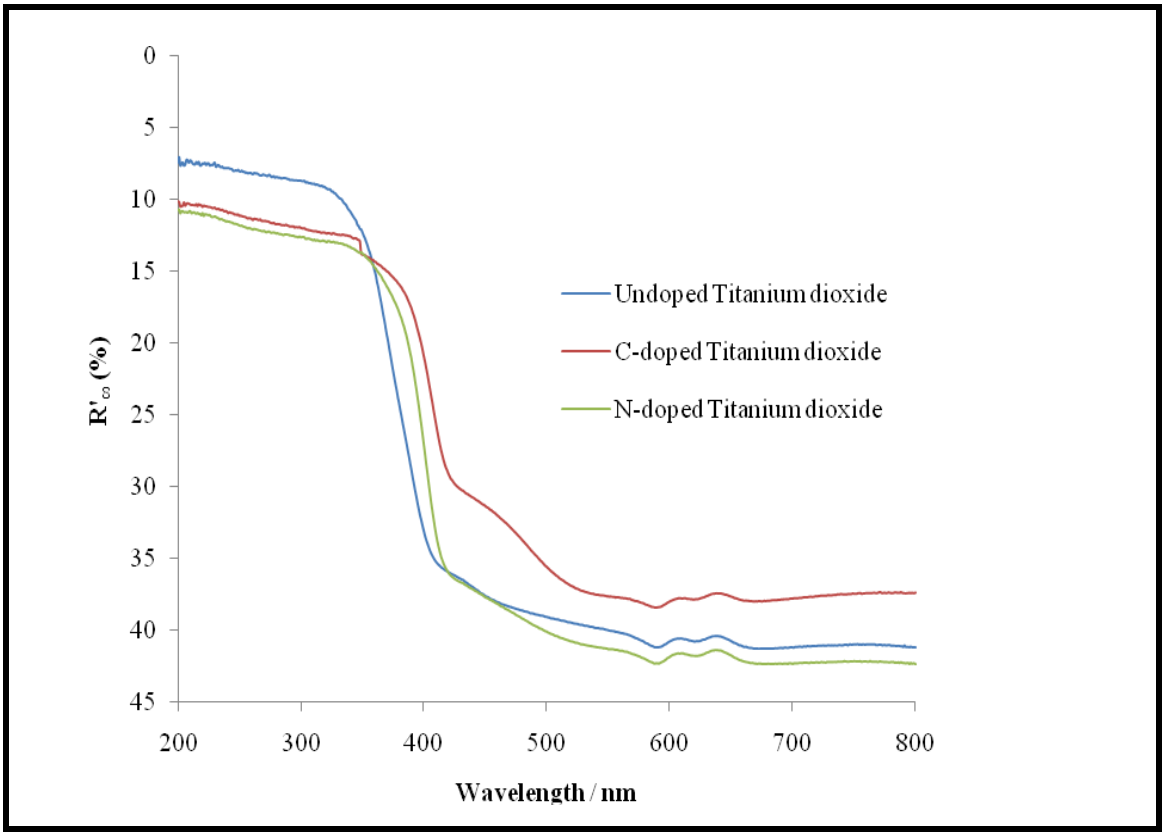

Figure 6.4: Diffuse reflectance spectra of undoped, carbon and nitrogen doped TiO_2.

Comparing the carbon doped TiO_2 to nitrogen doped TiO_2 with the same dopant concentration we can see that carbon is more effective in reducing the band gap than nitrogen. Compared to undoped TiO_2, the band gap changed from 2.95 eV to 2.72 eV and 2.91 eV for the carbon and nitrogen doped TiO_2 respectively. These results show that carbon doping is a promising approach for increasing the photocatalytic activity of TiO_2 photocatalyst.

6.3.1.2 Characterization by BET

The surface area and pore size of undoped TiO_2, C-doped TiO_2 and N-doped TiO_2 are shown in table 6.3. The results show that the pore size of TiO_2 is reduced and the surface area is increased when it is doped. The highest reduction in pore size and increase in surface area was observed when carbon was used as a dopant. This increase in surface area was due to a decrease in particle size. This implies that introducing dopants into TiO_2 reduces the growth of the crystallites.

Table 6.3: BET surface area of undoped TiO_2, C-doped TiO_2 and N-doped TiO_2.

Parameter	Blank TiO_2	C-doped TiO_2	N-doped TiO_2
Pore size (nm)	10.00928	6.52049	9.27362
Surface area (m^2/g)	62.2450	83.0444	67.0010
Langmuir (m^2/g)	85.5739	114.8131	91.1497

6.3.1.3 Characterization by electron spin resonance spectroscopy (ESR)

Electron Spin Resonance is also called electron paramagnetic resonance (EPR) or electron magnetic resonance spectroscopy (EMR). It measures the transition frequency between different electron spin states. ESR is very sensitive and allows the detection and characterization of paramagnetic defects which are believed to be significant for photocatalytic properties (Rajh et al, 2003). In this study the technique was used to characterize the nitrogen and carbon doped TiO_2 in more detail and to get basic information on the nature of the dopants. The ESR spectra were obtained on a standard Bruker ESR spectrometer.

The electron g-values were calculated using the formula: $g_e = hv/\mu_B B_0$ where

$\mu_B = 9.2741010 \times 10^{-24}$ Joule. $Tesla^{-1}$

B_0 = magnetic field

h = Plank's constant (6.63×10^{-34} J.s)

v = the microwave frequency used in the analysis

(i) Nitrogen doped-TiO_2

The nitrogen based paramagnetic species was labelled $N_b^{\cdot}$ in literature (Livraghi et al, 2006). The nitrogen doped TiO_2 is characterized by the presence of NO^{2-} or $N_b^{\cdot}$ species. These species lie above the valence band and are selectively excited by visible light. They are seen as an interstitial nitrogen atom stuck to oxygen and this is responsible for optical absorption (Livraghi et al, 2009). The ESR spectrum of the nitrogen doped TiO_2 is shown in Figure 6.5 and the ESR intensity is due to paramagnetic $N_b^{\cdot}$ species (Livraghi et al, 2006).

The signals at g-factor values of g =2.005 and g = 2.004 are due to $N_b^{\cdot}$ species (Livraghi et al, 2006), confirming that there is nitrogen in the doped TiO_2. The peak at g-factor value of 2.003 is due to the presence of oxygen vacancies in the TiO_2 ((Livraghi et al, 2006). We suspect that the intense signal at g-factor value of 1.947 is due to Ti^{3+} because it is very close to the literature value of 1.948 for Ti^{3+}. Some of the peaks on this nitrogen doped TiO_2 were due to noise.

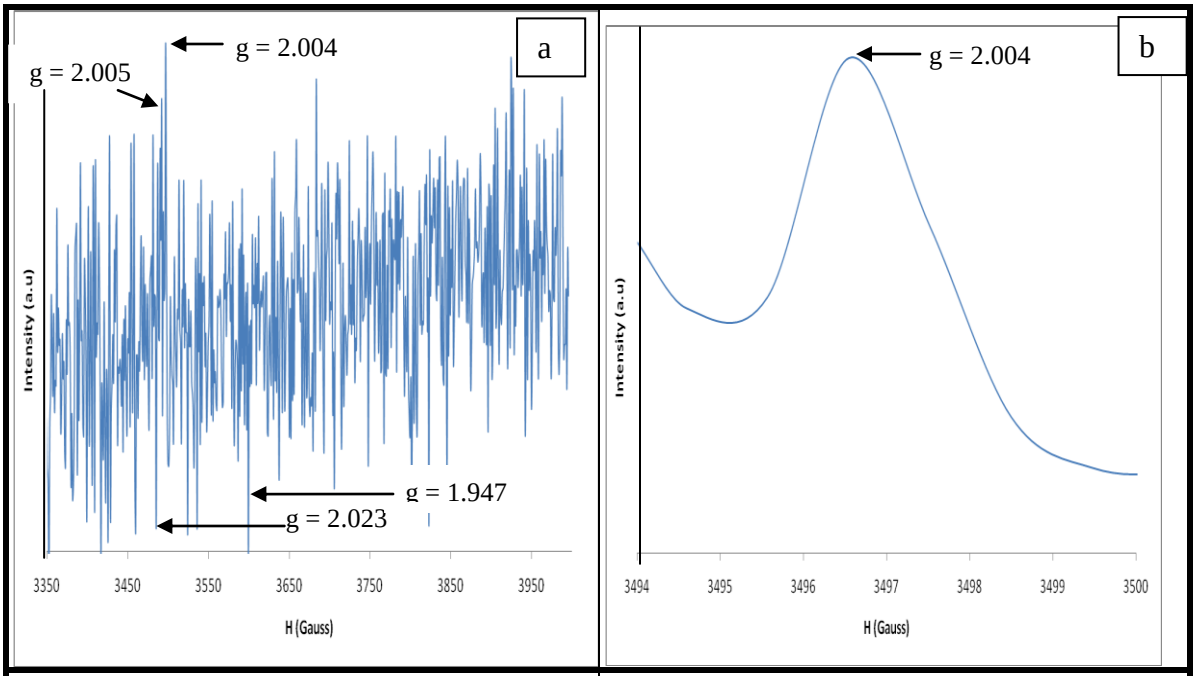

EPR spectra of nitron doped TiO_2.	Enlarged peak at g = 2.004

Figure 6.5: ESR spectra of nitrogen doped TiO_2; (a) full spectra; (b) enlarged peak at g = 2.004.

(ii) Carbon doped-TiO_2

The ESR spectrum of the carbon doped TiO_2 only showed one intense symmetrical signal at g = 2.0032 as shown in Figure 6.6. This signal is assigned to the carbon dopant which was in agreement with a typical literature value (2.003 ± 0.0005) reported by Konstantiinova et al, 2007.

It is reported that ESR signal arises after carbon doping, the g-value is typical for carbon radicals and the samples with a high content of carbon in general have more paramagnetic centers (Konstantiinova et al, 2007). Hence in this study it was deduced that the signal was due to carbon dopant.

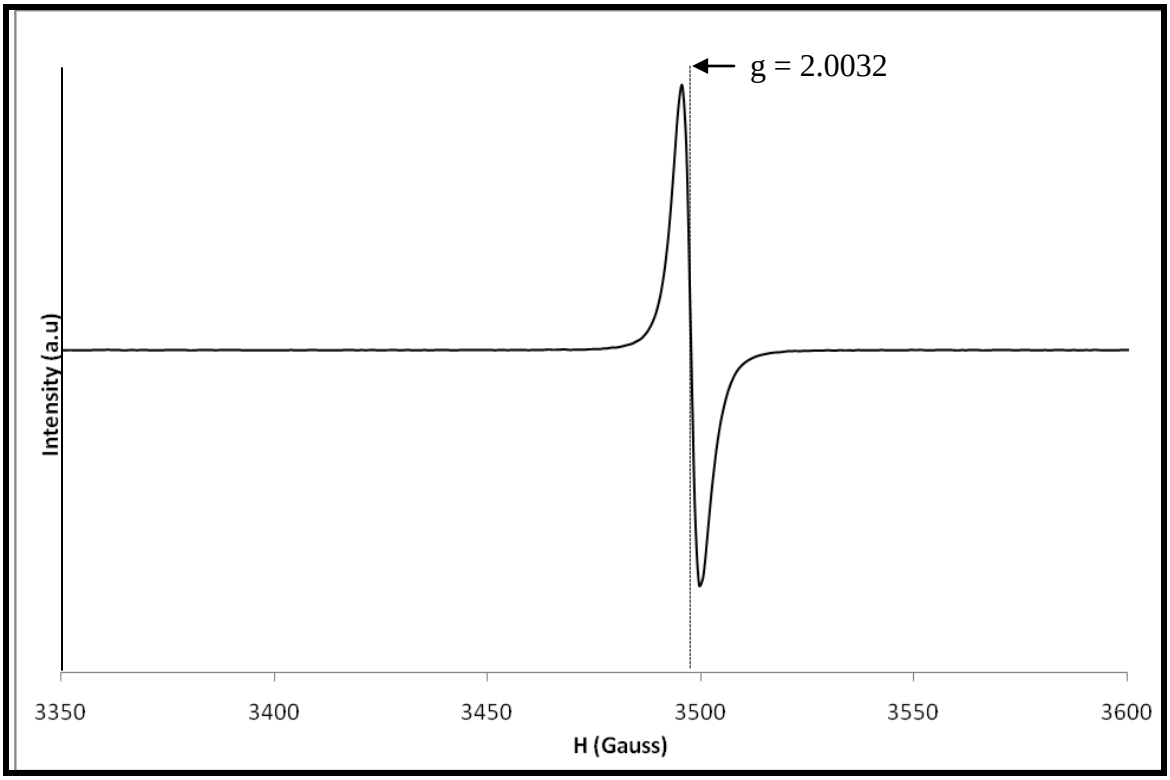

Figure 6.6: ESR spectrum of carbon doped TiO_2.

6.3.1.4 Characterization by SXPS

SXPS measurements were done to determine the atomic composition and concentrations of carbon in the doped TiO_2. The analysis was carried out at NMISA (Pretoria) using a Physical Electronics Quatum200 instrument which uses Al Kά X-rays (1486 eV) with a power of 20 W. The beam diameter was 100 μm and the pass energies were 117.4 eV (wide) and 29.35 eV (narrow). The analysis was done at an ambient temperature of 20 °C ± 5 °C and a relative humidity of 50 %RH ± 25 %RH.

From the SXPS spectra, the carbon doped TiO_2 contained only the elements carbon, titanium and oxygen and their surface atomic concentrations were 12.6 %, 24.4 % and 63.0 % respectively. The SXPS spectra of the carbon doped TiO_2 is shown in Figure 6.7.

The XPS signals of Ti 2p were observed at binding energies around 458.4 eV (Ti $2p_{3/2}$ and 465 eV (Ti $2p_{1/2}$). Reduction of the valence state of titanium from Ti^{4+} to Ti^{3+} shifts the binding energy of Ti $2p_{3/2}$ to lower energies (Yang et al, 2006). In this study the binding energy of Ti 2p was 458.4 eV showing a red shift of 0.2 eV from 458.6eV, for pure anatase (Li et al, 2005: Yang et al, 2007). This suggests that Ti^{3+} species were formed in the doped TiO_2 (Chen et al, 2004). This shift in XPS signals to low binding energies in the carbon doped TiO_2 suggests successful incorporation of carbon TiO_2 into the lattice.

To investigate the carbon states in the TiO_2, the C 1s core shells were measured. The deconvolution of the C 1s core levels revealed three signals at binding energies of 284.7 eV, 286.4 eV and 288.9 eV as shown in Figure 6.7 D. The binding energy at 286.4 eV is attributed to C-O bond and the signal at 284.7 eV is assigned to C-C due the carbon of the organic compound that remained in the TiO_2. In a study by Ren et al, 2007, it was reported that one kind of carbonate species with a binding energy of 288.6 eV was observed and revealed that carbon may substitute some of the titanium atoms resulting in a Ti-O-C structure. In this study the peak at 288.9 eV could be assigned to Ti-O-C structure in the carbon doped TiO_2 by substituting some of the lattice titanium atoms with carbon atoms. The O 1s spectrum shows binding energy at 529.7 eV due to Ti^{4+}-O which is in agreement with the work of Xiao et al, 2008.

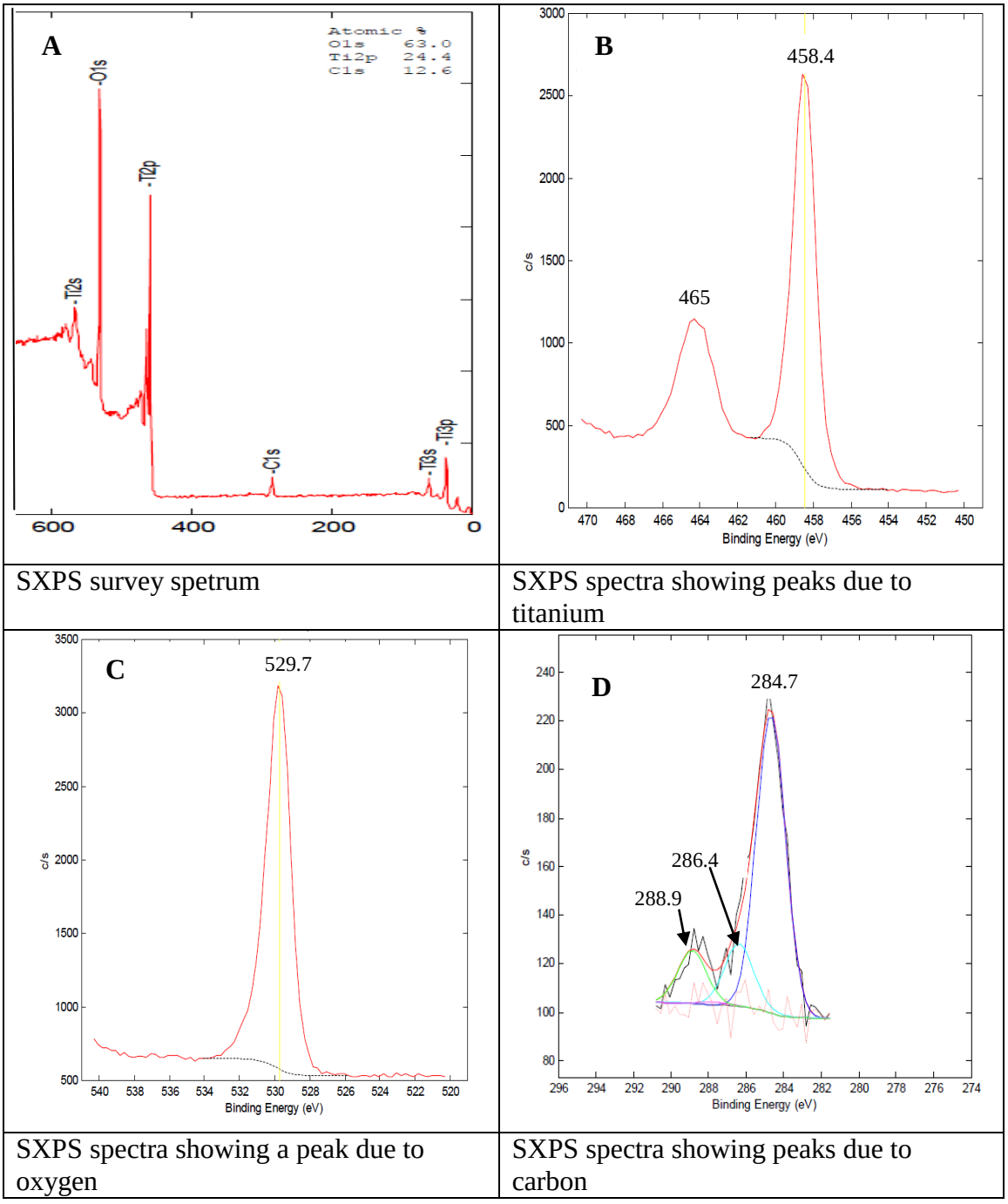

SXPS survey spetrum

SXPS spectra showing peaks due to titanium

SXPS spectra showing a peak due to oxygen

SXPS spectra showing peaks due to carbon

Figure 6.7: SXPS spectra of the doped TiO_2

The SXPS results showed the presence of Ti^{3+} in the carbon doped TiO_2 thus indicating the presence of oxygen vacancies which improves the photocatalytic activity of the photocatalyst. The presence of carbon in the TiO_2 lattice is further confirmed by electron spin resonance spectroscopy (ESR). The ESR spectrum of the carbon doped TiO_2 only

showed one intense symmetrical signal at g = 2.0032 as shown in Figure 4. This signal is assigned to the carbon dopant which is in agreement with the literature value (2.003 ± 0.0005) reported by Konstantiinova et al, 2007. They reported that the ESR signal arises after carbon doping while the g-value is typical for carbon radicals and the samples with a high content of carbon in general have more paramagnetic centres. Hence in this study we can conclude that the signal is due to carbon dopant.

6.3.1.5 Characterization of doped TiO_2 by FT-IR

The functional groups of undoped and doped TiO_2 nanoparticles were characterized by FT-IR transmittance and the spectra are shown in Figure 6.8. The broad band in the range 400-800 cm^{-1} was due to the stretching vibration of the Ti-O bond and this was common to all the three samples. The broad peak around 3400 cm^{-1} was more pronounced in the spectrum of undoped TiO_2 and another one at 1621 cm^{-1} which was common to all the samples was due to the surface adsorbed water and OH group of TiO_2 (Ding et al, 2000). Altar et al, 2008 reported that the peak at 1621 cm^{-1} could be assigned to the bending vibrations of coordinated water. This broad peak was not found in the spectra of nitrogen doped sample and it was very small in the spectrum of carbon doped implying that pure TiO_2 adsorbs more water than doped TiO_2. This showed the presence of hydroxyl group in the structure of the sample. The adsorbed water and the hydroxyl group are important to photocatalytic reactions because they produce hydroxyl radicals when they react with photo-excited holes on the surface of the catalyst. The small absorption peaks around 2938 cm^{-1} were probably due to the stretching mode of unreacted ethoxy groups such as $Ti\text{-}OC_4H_9$ (Wing & Limas-Ballesteros, 2001).

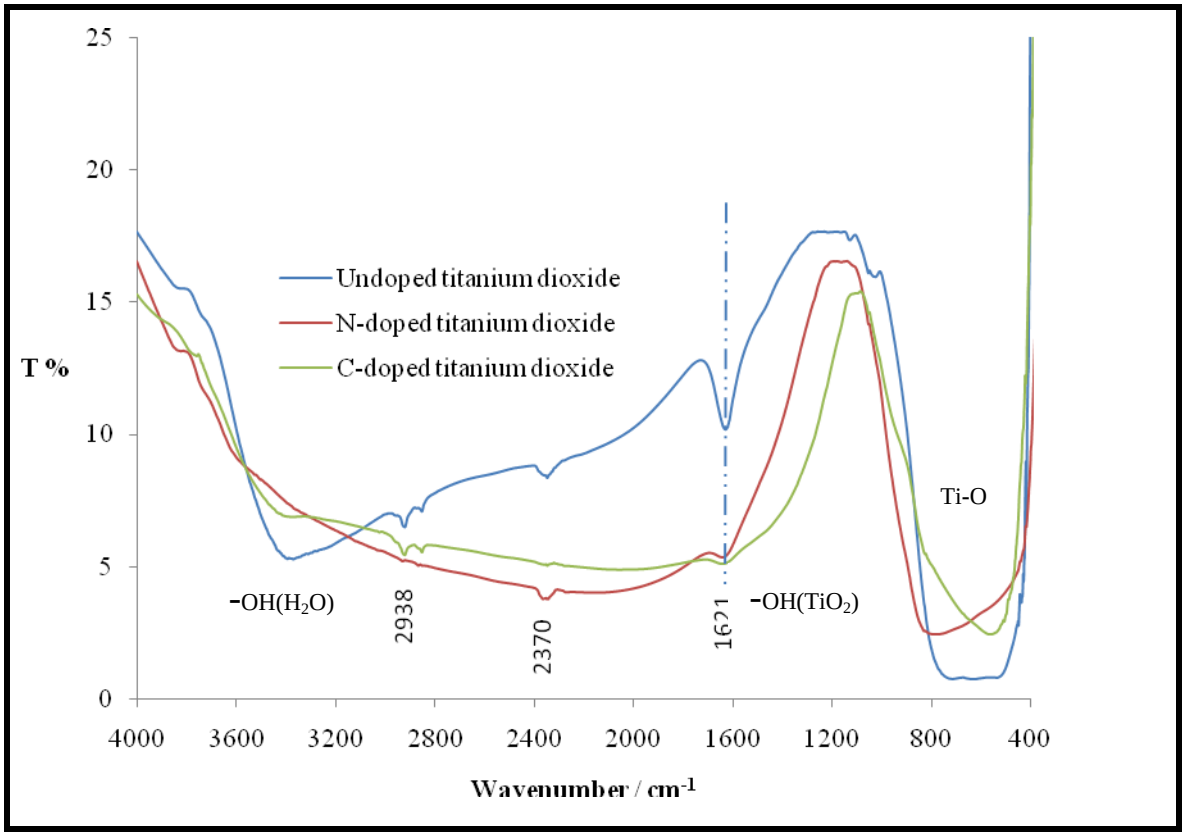

Figure 6.8: FT-IR spectra of undoped, nitrogen and carbon doped TiO_2.

6.3.2 Photocatalytic activity evaluations

In this section the photocatalytic measurements of the TiO_2 embedded polymer and carbon nanofibres were studied and reported. UV-Vis spectrophotometer was used for the determination of the change in concentration of the methyl orange solution chosen as the model pollutant.

6.3.2.1 Determination of the λ_{max} value of methyl orange

Before the evaluation of the photocatalytic activity of the TiO_2, the UV-Vis spectrum of methyl orange solution was obtained to see the range in which it absorbed ultraviolet light. Methyl orange a common acid-base indicator was chosen as a model of the azo

dyes mainly used in the chemical industry and found as a pollutant in water. It is yellow in alkaline solutions and red in acidic conditions. The structure of methyl orange is shown in Figure 6.9.

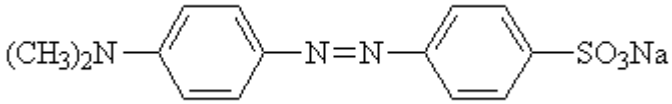

Figure 6.9: Structure of methyl orange

The spectrum of methyl orange is shown in Figure 6.10 and it shows two absorption peaks at 273 nm and a maximum absorption at 467 nm.

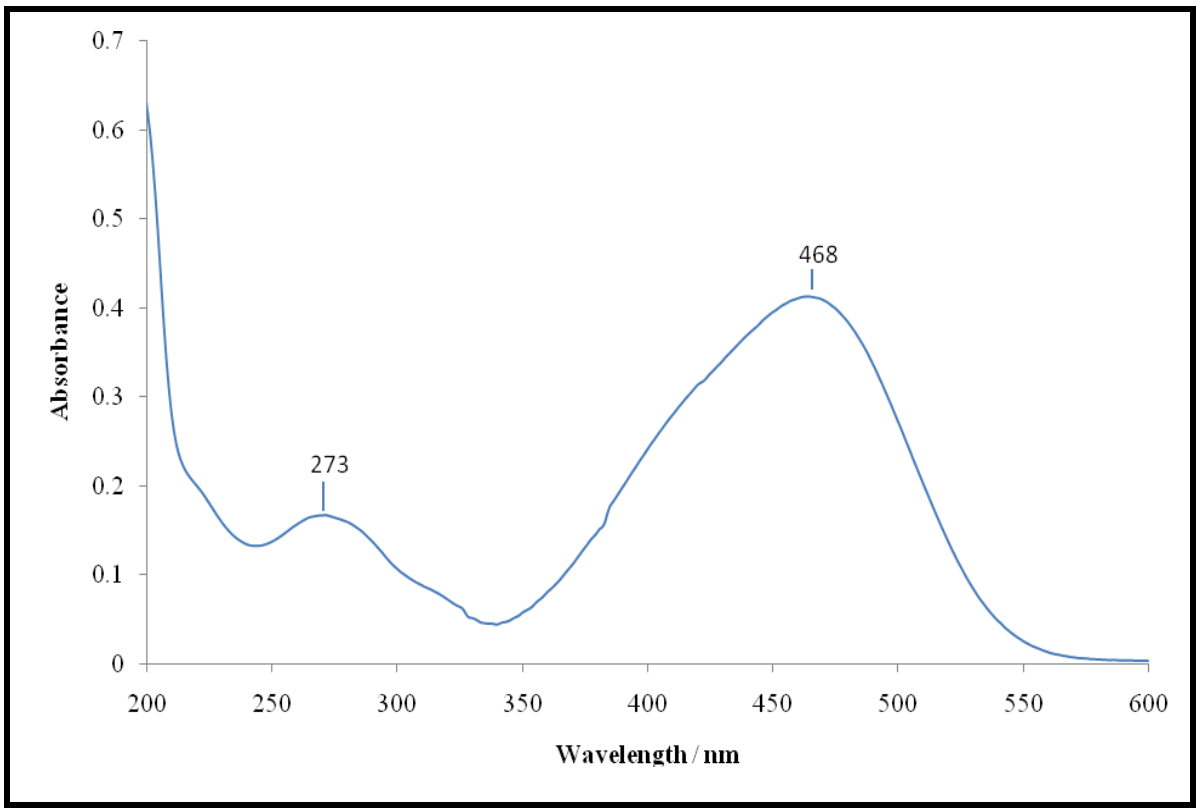

Figure 6.10: UV-Vis spectrum of 5 ppm methyl orange solution.

Since the concentration is best determined at the wavelength of maximum absorption, where the absorbance varies least with a change in concentration (Enke, 2001), a wavelength of 468 nm for determination of change in concentration was used

6.3.2.2 Determination of adsorption equilibrium time

Before photocatalytic activity measurements it was necessary to estimate the time required for the nanofibres to reach adsorption equilibrium (saturation). The reason was to ensure that in photocatalytic activity measurements, changes in concentration of the methyl orange were only due to photocatalysis. The experimental results showed that adsorption of methyl orange on the TiO_2 embedded carbon nanofibres reached equilibrium after an hour and the concentration of the methyl orange did change with prolonged time. After saturation and exposure to UV-light, the concentration of the methyl orange started changing due to photodegradation by TiO_2 photocatalyst.

6.3.2.3 Photodecomposition of methyl orange - effect of concentration

The results for the photocatalytic degradation of methyl orange by TiO_2 prepared at the same temperature (60 °C) using different precursor concentrations are presented in Figure 6.11. The highest degradation was observed for a sample prepared with the lowest concentration and the least degradation for the sample prepared with the highest concentration. The reason for this trend is that as the precursor concentration was increased, the particle size also increased resulting in a decrease in the surface area. In the photocatalytic degradation process, photoreaction takes place on the surface of the TiO_2 nanoparticles and hence the larger the surface area of the photocatalyst, the higher the degree of adsorption and photodegradation of methyl orange.

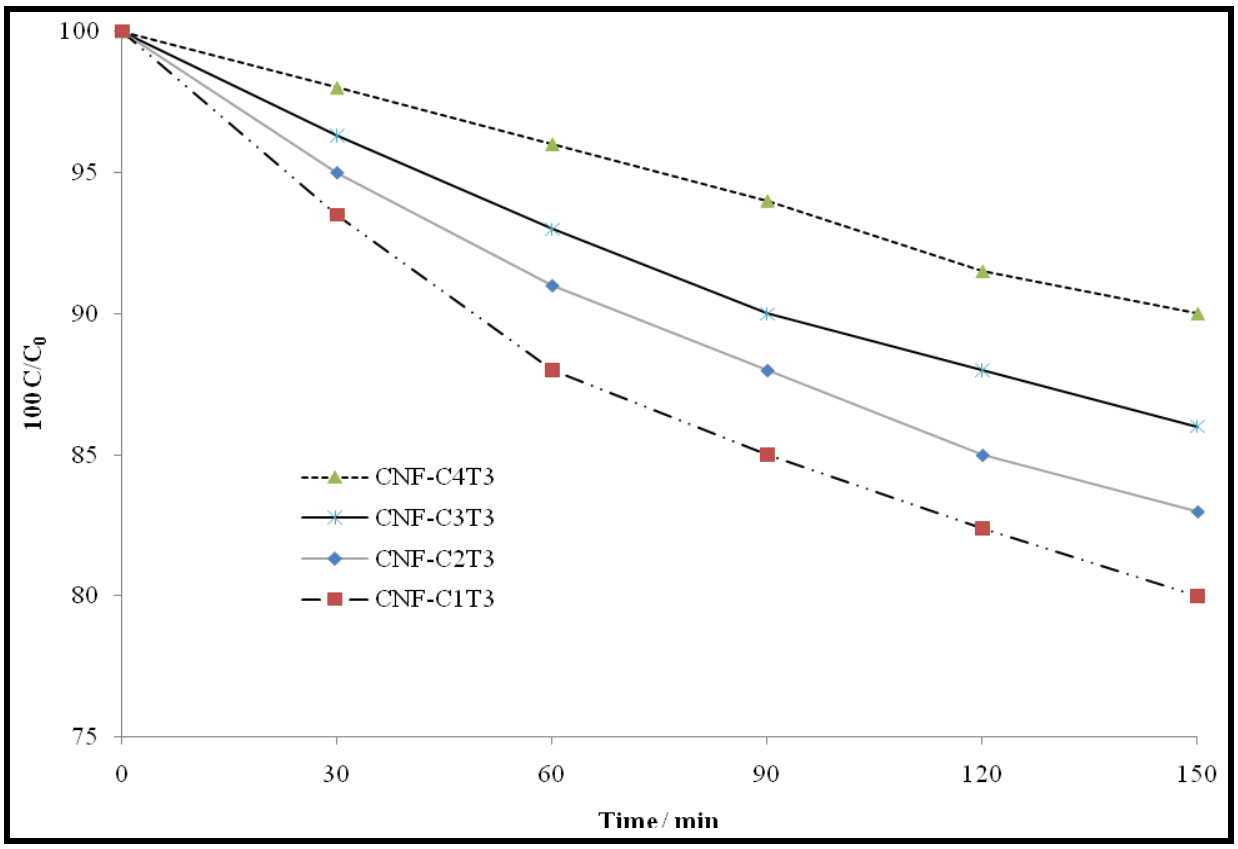

Figure 6.11: Photodecomposition of methyl orange by TiO_2 nanoparticles prepared using different precursor concentrations supported on carbon nanofibres.

The smaller the TiO_2 particles the shorter distance to be travelled by electrons from the valence band to the catalytic site resulting in an increase in the photocatalytic activity (Hafizah & Sopyan, 2009). From the XRD results it was observed that the sample prepared with the highest concentration had more of the rutile phase than the anatase phase. This also explains why it showed the lowest degradation rate since rutile phase is generally less photocatalytically active than the anatase phase.

6.3.2.4 Photodecomposition of methyl orange – effect of temperature

The plots showing methyl orange degradation by TiO_2 nanoparticles prepared using the same precursor concentration (0.7841 M) but different sol-gel temperatures are shown in Figure 6.12.

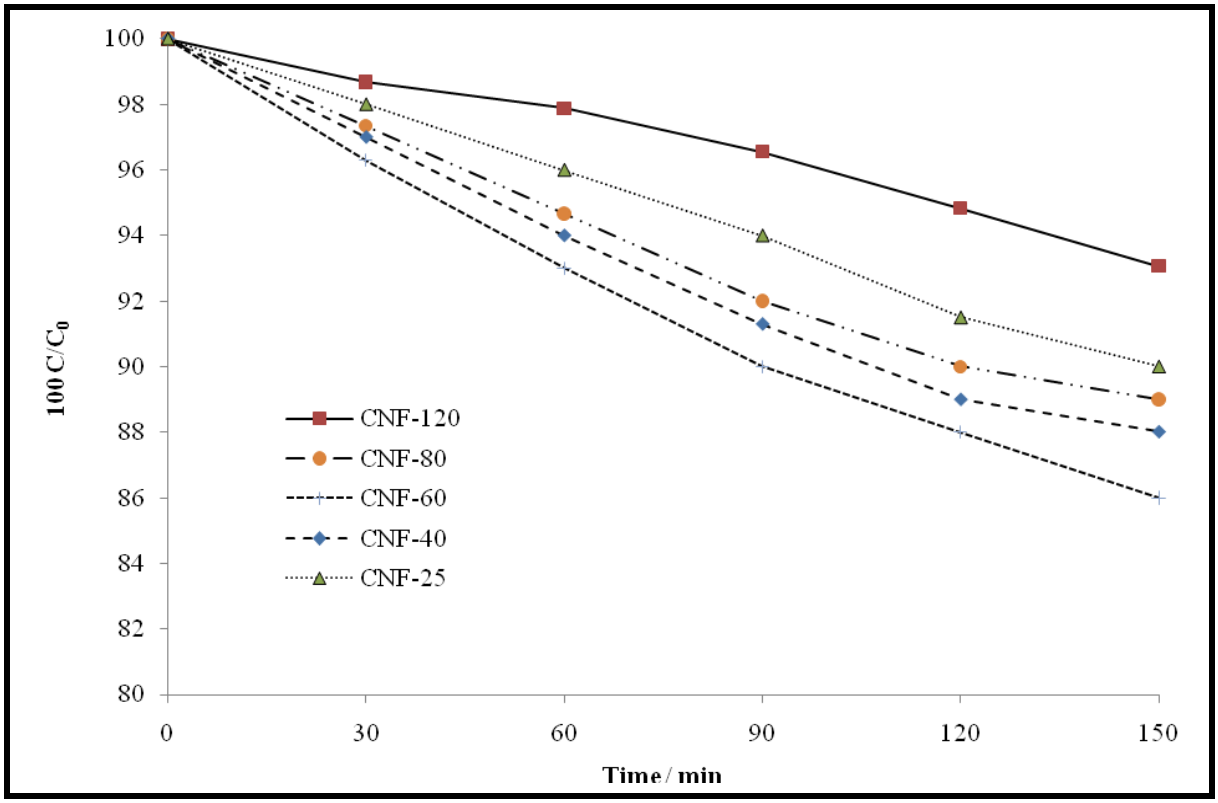

Figure 6.12: Photodecomposition of methyl orange by TiO_2 nanoparticles prepared at different sol-gel temperatures supported on carbon nanofibres.

It was found that the sample prepared at 60 °C showed the highest degradation rate because it had the smallest average particle size of 3 nm – 5 nm (Section 5.6) which provides a high surface area for adsorption and increase surface active sites for the photodegradation of methyl orange. The sample prepared at 120 °C showed the least degradation rate and this can be explained by its bigger particle size.

6.3.2.5 Photodecomposition of MeO by C-doped TiO_2 nanoparticles

Figure 6.13 shows the changes in the concentration of the methyl orange at different irradiation times due to photodegradation by carbon doped TiO_2 nanoparticles on carbon nanofibre supports.

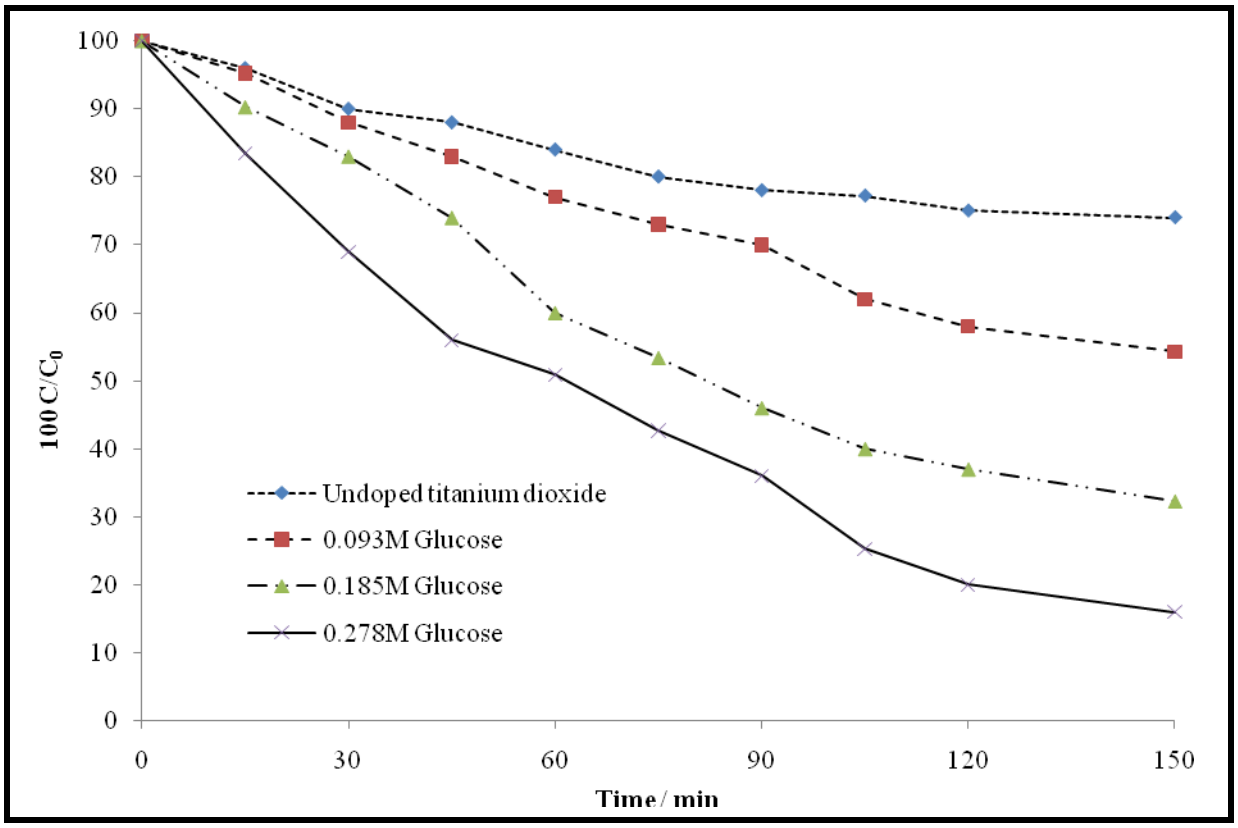

Figure 6.13 Photodecomposition of methyl orange by TiO_2 nanoparticles doped with different loadings of glucose supported on carbon nanofibres.

The photocatalytic activity of the samples increased with an increase in the dopant concentration. After 150 minutes, 84 % of the methyl orange was degraded by TiO_2 doped with a glucose concentration of 0.278 M. All the doped samples generally showed a high photocatalytic activity than the undoped TiO_2 which removed only 26 % of the initial methyl orange after 150 minutes. This shows that the degradation was much enhanced by incorporation of carbon into the lattice structure of TiO_2 which reduced the

band gap and also increased the surface area for adsorption. Based on the ESR and XPS results, the presence of Ti^{3+} species led to the formation of oxygen vacancies resulting in high photocatalytic activity.

6.3.2.6 Photodecomposition of MeO by N-doped TiO_2 nanoparticles

The photocatalytic activity of the nitrogen doped TiO_2 on carbon nanofibres with different dopant concentrations are shown in Figure 6.14.

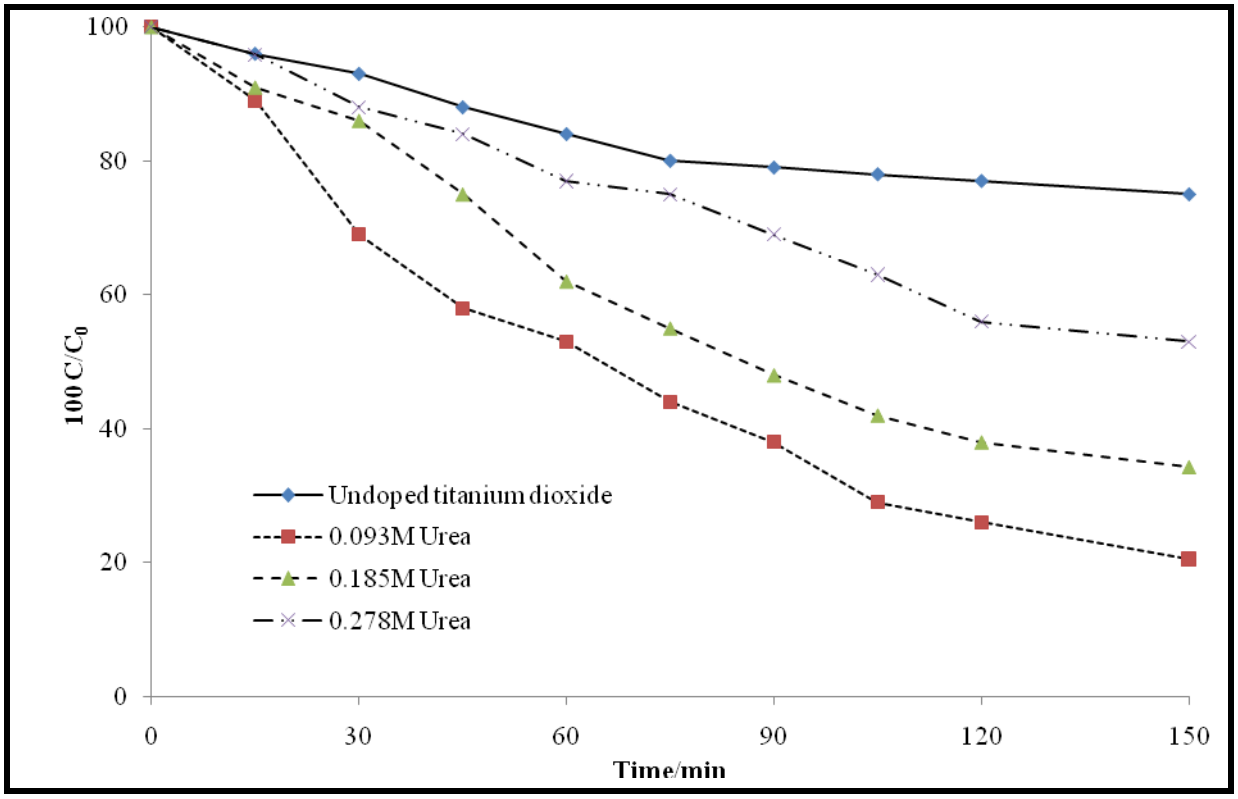

Figure 6.14: Photodecomposition of methyl orange by TiO_2 nanoparticles doped with different loadings of urea supported on carbon nanofibres.

All the doped samples showed a higher photocatalytic activity than the undoped TiO_2. After 150 minutes, 79.5 % of the methyl orange was degraded by TiO_2 doped with a urea concentration of 0.093 M, then 65.5 % and 47 % for TiO_2 doped with 0.185 M and 0.278

M respectively. The general increase of photocatalytic activity of the doped compared to undoped TiO_2 is due to the reduction in band gap and an increase in surface area evidenced by BET surface area measurements. The nitrogen is thought to substitute some oxygen atoms in the lattice of TiO_2 resulting in the narrowing of the band gap by mixing the N 2p and O 2p states.

6.4 Conclusions

The photodegradation experiments showed that doping with nitrogen or carbon increase the photocatalytic activity of TiO_2 through reduction of band gap and increase in surface area. These results also prove that heterogenous photocatalysis is a technique that can be successfully used for complete degradation of azo-dyes from wastewater in textile industries.

References

Altar, A. S.; Ghamsari, M. S.; Hajiesmaeilbaigi, F.; Mirdamadi, S. *Journal of Materials Science* **2008**, *43*, 1723-1729.

Chen, C.; Bai, H.; Chang, C. *Journal of Physical Chemistry C* **2007**,*111*, 15228–15235.

Choi, W.; Termin, A.; Hoffmann, M. R. *Journal of Physical Chemistry* **1994**, *98*, 669.

Ding, Z.; Lu, G. Q.; Greenfield, P. F. *Journal of Physical Chemistry* B **2000**, 104 4815

Di Valentin, C.; Pacchioni, G.; Selloni, A.; Livraghi, S.; Giamello, E. *Journal of Physical Chemistry* B **2005**, *109*, 11414–11419.

Enke, C. G. *The art and science of chemical analysis* **2001**.

Hafizah, N & Sopyan, I. *International Journal of Photochemistry* **2009**,*10*, 1155.

Huanga, D. G.; Liao, S. J.; Liu, J. M.; Danga, Z.; Petrik, L. *Journal Photochemistry and Photobiology A*: Chem **2006**, *184*, 282–288

Konstantinova, E. A.; Kokorin, A. I.; Sakthivel, H. K.; Lips, K. *Chimia International Journal fro Chemistry* **2007**, *61*, 810-814.

Livraghi, S.; Elghniji, K.; Czoska, A. M.; Paganini, M. C.; Giamell, O. E.; Ksib, I. M. *Journal of Photochemistry and Photobiology A*: *Chemistry* **2009**, *205*, 93–97

Livraghi S.; Paganini M. C.; Giamello E.; Selloni A.; Di Valentin C.; Pacchioni G. *Journal of the American Chemical Society* **2006**, *128*, 15666–15671.

Mo, S. D & Ching, W. Y. *Physical Review B* **1995**, *51*, 13023-13032.

Yang, X.; Cao, C.; Erickson, L.; Hohn, K.; Maghirang, R.; Klabunde, K. *Journal of Catalysis* **2008**, *260*, 128–133.

Rajh, T.; Poluektov, O. G.; Thurnauer, M. C. *Chemical Physics of Nanostructured Semiconductors* **2003.**

Rengaraji, S & Li, X. Z. *Journal of Molecular Catalysis A*: Chemical **2006**, *243*, 60–67.

Weng W.; Ma M.; Du P.; Zhao G.; Shen G.; Wang J.; Han G. *Surface & Coatings Technology* **2005**, *198*, 340– 344.

Wang, J. A & Limas-Ballesteros, R. *Journal of Physical Chemistry B* **2001**, *105*, 9692–9698.

CHAPTER 7

7. Conclusions and recommendations
7.1 Conclusions

TiO_2 nanoparticles with the desired properties can be synthesized by controlling the hydrolysis of the precursor. The properties such as particle size, crystallinity and photocatalytic activity depend on the preparation conditions such as sol-gel temperature and precursor concentration. The results of this study showed that the best sol-gel temperature was 60 °C using a precursor concentration of 0.3922 M. Increase in both temperature and precursor concentration resulted in an increase in particle size. From the XRD results it can be concluded that, temperature is a more important parameter than concentration in controlling the properties of TiO_2 such as crystallinity and particle size. The calcined TiO_2 nanoparticles prepared at high precursor concentration (1.3 M) contained high rutile phase due to easy transformation of anatase to rutile when the particles are big.

Solutions of PAN and TiO_2 in DMF represent a good way of producing TiO_2 embedded nanofibres via electrospinning. Thermal analysis showed that, to produce carbon nanofibre supports which are strong, low heating rates during stabilization are required. Low heating rates such as 5 °C cause less damage and fragmentation of the polymer chains resulting in strong catalyst supports. This stabilization process is a slow and time-consuming process that plays an important role in determining the final properties of the

fibres. The structural changes due to temperature deduced from the FT-IR and Raman spectra were seen to be consistent with DSC, DTA and TGA studies.

The study demonstrated that the photocatalytic activity of the TiO_2 nanoparticles depended on particle size and the ratio between anatase and rutile phase. In the phodegradation process, first there was adsorption of the methyl orange by the carbon nanofibres and TiO_2 which was directly proportional to the surface area. After adsorption there was the oxidation of the methyl orange by the radicals. Thus the rate of photodegradation of methyl orange is related to the following factors:

i. The particle size and surface area of the photocatalyst
ii. Stability of the methyl orange to oxidation
iii. The tendency of the methyl orange to adsorb on to the TiO_2 and carbon nanofibres

The carbon doped and nitrogen doped TiO_2 nanoparticles were successfully prepared by a simple sol-gel process. The carbon dopant came from glucose and nitrogen dopant from urea. The doped TiO_2 nanoparticles showed an improvement in optical absorption, for instance, a shift of 0.23 eV for the TiO_2 doped with 0.093 M glucose and 0.06 eV for the TiO_2 doped with 0.185 M urea. The doped nanoparticles also showed a higher photocatalytic activity than the undoped nanoparticles due to band gap narrowing. When the photocatalytic activity of the carbon and nitrogen doped samples were compared, it was observed that the carbon doped TiO_2 showed higher photocatalytic activity because incorporation of carbon resulted in an increase in the surface area of the nanoparticles for adsorption of the methyl orange.

7.2 Recommendations for Further Work

It is recommended that further studies should be done on the optimization of dopant loading for effective reduction in band gap since in this study only three different concentrations were used and there was no general trend that was found when the dopant concentration was increased. Optimization of TiO_2 photocatalyst loading in the carbon nanofibres for effective degradation of organic contaminants should also be studied. It would be interesting to investigate the effect of the repeated use of the supported photocatalyst on the photocatalytic activity and check if there is any detachment of TiO_2 from the carbon nanofibres.